國立交通大學

電子工程學系電子研究所

博士論文

量子點紅外線偵測器及銻化鎵材料之研究

Studies of Quantum Dot Infrared Photodetectors and GaSb Material

研究生：羅明城
指導教授：李建平　教授
共同指導：王祥宇　博士

中華民國 九十八 年 六 月

量子點紅外線偵測器及銻化鎵材料之研究

Studies of Quantum Dot Infrared Photodetectors and GaSb Material

研究生：羅明城　　Student：Ming-Cheng Lo
指導教授：李建平　　Advisor：Dr. Chien-Ping Lee
王祥宇　　Dr. Shiang-Yu Wang

國立交通大學
電子工程學系 電子研究所
博士論文

A Dissertation
Submitted to Department of Electronics Engineering and
Institute of Electronics
College of Electrical and Computer Engineering
National Chiao Tung University
in partial Fulfillment of the Requirements
for the Degree of
Doctor of Philosophy
In Electronics Engineering

June 2009

Hsinchu, Taiwan, Republic of China

中華民國九十八年六月

量子點紅外線偵測器及銻化鎵材料之研究

研究生：羅明城　　　　　　　　指導教授：李建平　博士
王祥宇　博士

國立交通大學
電子工程學系電子研究所

摘要

本論文分成兩個部分：第一部份為砷化銦量子點紅外線偵測器(第三～六章)，另一部份為銻化鎵材料之研究（第七、八章)。

在第一個部分我們利用分子束磊晶系統成長高品質之砷化銦量子點製作紅外線偵測器，研究包括：偵測器其響應值對於溫度及偏壓的相依性探討、垂直偶和的量子點紅外線偵測器的特性分析、以及偵測器中的光電流頻譜調整及躍遷能階之研究。

量子點紅外線偵測器的響應對於溫度及偏壓的相依性與量子井紅外線偵測器，具有相當的差異性。對於量子井而言，響應的大小對於溫度變化溫度並沒有太大的改變，對於偏壓則呈現線性的相依性。但是，對於量子點而言：響應對於溫度及偏壓都是呈現指數關係的變化。經由詳細的元件電流增益行為的量測，對於此響應行為我們有深入的分析。在100度K的溫度變化中，元件的電流增益約

有兩個數量級的改變，如此巨大的改變是由於量子點中額外注入的載子所產生的庫輪排斥力作用，此外我們亦計算了額外注入的載子數目。此額外注入的載子會改變量子點中的費米能階並且改變元件的量子效率。

對於垂直耦合的的量子點紅外線偵測器的特性，我們做了詳細的分析研究。對於垂直耦合的量子點中，會形成一個微能帶，此微能帶會使得載子在量子點中自由的移動帶，會使得量子點中的能階分佈更為均勻，進而縮小光電流頻譜的半高寬並提高元件之量子效率。此外，此垂直耦合的量子點亦可以提高自由載子的捕捉機率，因此，此結構亦可提高元件的頻率響應頻寬。

我們在標準的量子點紅外線偵測器中的量子點下方加入一層高能障之砷化鋁鎵，藉此調整元件中的載子躍遷行為。標準之偵測器其光電流響應頻譜會隨著加入之高能障層而分離成兩個訊號，其中一個光訊號並不會隨著此高能障層與量子點的距離改變而有所變化，但是另一個光訊號會慢慢的往短波長移動並且響應強度也會慢慢減弱。當此高能障層與量子點的距離只有五奈米的時候，只有一個光響應訊號會存在。因此，此光電流頻譜的半高寬與峰值波長的比例會從 25% 降低至 10%，且元件之量子效率亦可提高。此外，此加入之高能障層亦會降低元件之暗電流，進而提高元件之偵測度表現。

第二部分為銻化鎵材料的研究，分成兩個章節：一部份為銻化鎵在砷化鎵基材中的量子點成長，另一部份為銻化鎵的矽基板上的磊晶研究。

對於銻化鎵量子點的成長我們有系統的做了一系列的實驗，包括：磊晶材料的厚度、磊晶溫度及五族三族的通量比例等。我們藉由原子力顯微鏡分析成長之量子點的表面型態，包括量子點密度及大小。此外，我們亦研究了此第二類超晶格量子點的光激光譜行為，分別分析其光譜在不同的激發光密度及不同的溫度下的表現，有別於第一類超晶格量子點，此種類的量子點光激光譜有極不同的行為。另外，我們亦發現了一層、兩層及三層的銻化鎵原子層的光譜訊號，藉由理論的分析，我們可以研究推估銻化鎵及砷化鎵兩種異質材料的價帶不連續的能量大小。

我們對於銻化鎵材料在矽基板上成長的緩衝層材料做了研究探討。如果將銻化鎵直接成長於矽基板上，銻化鎵材料的表面會非常的粗糙，藉由銻化鋁緩衝層的加入，我們可以成功的提高銻化鎵的磊晶品質，此銻化鋁一開始會在矽基板表面形成量子點，並隨著更多銻化鋁的成長此量子點會連結起來，此過程會吸收因為晶格常數不匹配而產生的應力，進而使得銻化鎵的磊晶品質提升。此外，我們亦使用的銻化鋁/銻化鎵間格的超晶格結構去阻擋晶格缺陷的延展，此種緩衝層結構會更進一步的提升銻化鎵的磊晶品質。

Studies of Quantum Dot Infrared Photodetectors and GaSb Material

Student：Ming-Cheng Lo **Advisor：Dr. Chien-Ping Lee**

Dr. Shiang-Yu Wang

Department of Electronics Engineering & Institute of Electronics Enineering

National Chiao Tung University

Abstract

The thesis was separated into two parts: one is the quantum dot infrared photodetectors (QDIPs) based on the InAs/GaAs QDs (chapter 3, 4, 5 and 6), and the other is the GaSb material study (chapter 7 and 8).

In the first parts, we studied the temperature dependent responsivity behavior of QDIPs, vertically coupled QDIPs, and photocurrent spectra tuning of QDIPs.

Temperature dependent behavior of the responsivity of InAs/GaAs quantum dot infrared photodetectors was investigated with detailed measurement of the current gain. The current gain varied about two orders of magnitude with 100K temperature change. The dramatic change of the current gain is explained by the repulsive coulomb potential of the extra carriers in the QDs. With the measured current gain,

the extra carrier number in QDs was calculated. The extra electrons in the QDs elevated the Fermi level and changed the quantum efficiency of the QDIPs. The temperature dependence of the responsivity was qualitatively explained with the extra electrons.

Vertically coupled InAs/GaAs quantum dot infrared photodetectors (QDIPs) were studied. With vertically coupled quantum dots, the formation of the mini-bands among quantum dot (QD) layers enhances the uniformity of QD states and results in a narrow response spectrum and higher peak quantum efficiency. The mini-bands increase the capture probability and also facilitate the carrier flow among QD layers and leads to more uniform carrier distribution. Because these, the frequency response of vertically coupled quantum dot infrared photodetectors were much faster than that of the conventional ones.

The quantum dot infrared photodetectors (QDIPs) with an additional thin $Al_{0.2}Ga_{0.8}As$ layer near the quantum dot (QD) layers were studied. With the thin $Al_{0.2}Ga_{0.8}As$ layer, the carrier transitions of the QDIPs can be refined. The board absorption peak of the InAs/GaAs QDIPs splits into two response peaks with the additional $Al_{0.2}Ga_{0.8}As$ layer. These two signals have different behaviors as the spacing between the $Al_{0.2}Ga_{0.8}As$ layer and QDs is changing. One of the peaks remains fixed at the same wavelength, and the other peak shifts to higher energy and the intensity becomes weaker as the $Al_{0.2}Ga_{0.8}As$ layer is closer to the QD layers. A much narrow photocurrent spectrum was observed when the $Al_{0.2}Ga_{0.8}As$ layer is 5 nm to the QDs. The fractional spectra width is reduced from 25% to 10% and the quantum efficiency is enhanced. Combining with the reduced dark current due to the higher barrier, the detectivity increases for about 5 times.

In the second part, the GaSb material was studied, including the GaSb/GaAs quantum dots growth and GaSb growth on silicon substrate.

The growth conditions of GaSb/GaAs quantum dots were studied systematically, including the GaSb film thickness, substrate temperature and the V/III beam equivalent flux ratio. The morphology of quantum dots is studied by the atomic force microscope. And, the excitation power density and temperature dependent photoluminescence is also studied. Due to the type-II band alignment, the result is different from the type-I band alignment system. Also, the distinct light emission peaks from monolayers of GaSb quantum wells in GaAs were observed. Discrete atomic layers of GaSb for the wetting layer prior to quantum dot formation give rise to transition peaks corresponding to quantum wells with one, two and three monolayers. From the transition energies we were able to deduce the band offset parameter between GaSb and GaAs. By fitting the experimental data with the theoretical calculated result using an 8×8 $\mathbf{k\bullet p}$ Burt’s Hamiltonian along with the Bir-Picus deformation potentials, the valence band discontinuity for this type II heterojunstion was determined to be 0.45 eV.

The heterojunction growth of GaSb on Silicon (001) substrate with different buffer layer structure was studied. When the GaSb deposited directly on the silicon surface, the epitaxial GaSb shows a non-mirror surface. It is necessary to use the AlSb as the buffer layer in the heterostructure growth. The AlSb forms QDs on silicon surface at first few monolayers. When more AlSb deposited, the QDs would coalesce. The process is strain relief mechanism and results in better GaSb crystal quality. Furthermore, the GaSb/AlSb superlattice interface would merge and stop the dislocation propagation. Therefore, the superlattice buffer layer further increases the GaSb crystal quality.

致　謝

七年研究生涯中，最感謝指導教授李建平博士及王祥宇博士，李教授在教學及研究上的指導是我完成本論文的最重要因素，而王博士在量子點紅外線偵測器的研究上給予的指導與討論亦是我完成本論文的另一個重要的因素。

此外非常感謝我的家人，父親的二十多年來的養育照顧以及在求學過程中支持，使我能在求學過程中一切順利。姊姊們在這段時間中，幫忙分擔照顧父親的責任，也給予了莫大的幫助。

也要感謝所有曾經在 MBE 磊晶設備上付出過心力的學長：張國雄博士、蔡光隆博士、蔡嘉明博士、王祥宇博士，林聖迪博士及李秉奇博士，沒有你們過去在 MBE 上的努力及傳承，我將無法順利完這些的研究。而實驗室的學長：林志昌博士、王興燁博士、廖志豪博士、李定麒博士、黃世傑博士及林決仁學長，你們在磊晶設備使用維護上的指導及分析量測技術上的教導，亦是我研究上的一大助力。另外所有共同奮鬥的伙伴們：黃博聲、張至揚及呂佳穎同學，淩鴻緒、林大鈞學弟，感謝你們在我研究生活中的低潮中給予鼓勵與支持。

最後要感謝珮心，在博士求學生活中陪伴與支持。

CONTENTS

Abstract (Chinese)……………………………………………………….…..….i

Abstract (English)……………………………………………………….……..iv

Acknowledgement…………………………………………………………..vii

Contests…………………………………………………………………..viii

Table captions………………………………………………………….. xi

Figure captions……………………………………………………….... xii

Chapter 1: Introduction

1.1 Infrared technology…………………………………..………...1

1.2 GaSb/GaAs quantum dots and GaSb growth on silicon…..…7

1.3 Organization of the thesis………..………………………..…9

Chapter 2: Experiment Techniques

2.1 Molecular beam epitaxy………..……………………….…12

2.2 Material characteristic analysis………………..………...…19

2.3 QDIPs device processes and measurement………...……21

Part I. Quantum Dot Infrared Photodetectors

Chapter 3: Fundamentals of Quantum Dot Infrared Photodetectors

3.1 Absorption of intersubband transitions…….……….……..27

3.2 Quantum efficiency…………………………….……..………28

3.3 Current gain……..….………………………….…….…………29

3.4 Responsivity……………………….……………….……………29

3.5 Dark current……………………………………………….…………30
3.6 Noise……………………………………………………….……30
3.7 Detectivity……………………………………………………….32

Chapter 4: Temperature Dependent Responsivity of Quantum Dot Infrared Photodetectors

4.1 Introduction……………………………………………...…34
4.2 Basic characteristics of sample…….…………………….35
4.3 Result and discussion…………………………………….39
4.4 Summary………………………………………………...48

Chapter 5: Vertically Coupled Quantum Dot Infrared Photodetectors

5.1 Introduction……………………………………………...…49
5.2 Vertically coupled QDs characteristics…….……………....50
5.3 Vertically coupled QDIPs characteristics…….…………...55
5.4 Result and discussion……………………………….…......57
5.5 Summary……………………………………………...…62

Chapter 6: Photocurrent Spectrum Tuning of Quantum Dot Infrared Photodetectors

6.1 Introduction……………………………………………...…63
6.2 Sample structure……………………………………...64
6.3 Result and discussion…………………………....…...…66
6.4 Summary……………………………………………...…77

Part II. III-Antimonide Semiconductor material

Chapter 7: GaSb/GaAs Quantum Dots Growth

7.1 Introduction……………………………………….…….78
7.2 Growth condition……………………….………….……79
7.3 Surface morphology study…………………………...….81
7.4 Photoluminescence study….……………………….……85
7.5 Discrete monolayer light emission form wetting layer….91
7.6 Summary……………………….……………………..….95

Chapter 8: GaSb Growth on Silicon (001) Substrate

8.1 Introduction……………………………………….…..…96
8.2 Growth conditions…………………………….…………96
8.3 Material quality characterization…………….…...….98
8.4 Discussion……………………………………….……101
8.5 Summary……………………………………......…103
Chapter 9: Conclusion……………………………………………104

Reference……………..…………………………………………107

Vita…………………………………………………………………113

Publication List…………………………………………………114

TABLE CAPTIONS

CHAPTER 1:

Table 1.1: Advantages and limitations of different type infrared detectors. 4

CHAPTER 4:

Table 4.1: The parameters used in calculation of average excess carrier in QDs. 44

CHAPTER 7

Table 7.1: The list of the GaSb quantum structure growth conditions and surface QD density. 81

FIGURE CAPTIONS

CHAPTER 1

Figure 1.1: The blackbody radiation spectra at 350K, 300K, and 250K. The peak intensity varies from 8.5 μm to 11.5 μm. 3

Figure 1.2: The atmosphere transmittance spectrum. 3

Figure 1.3: The schematic drawing of the type-I, type-II and type-III heterojunction. 7

Figure 1.4: The schematic drawing of the band alignment of GaSb and InAs in GaAs matrix. 8

Figure 1.5: Energy bandgap versus lattice constant of the III-V semiconductor. 9

CHAPTER 2

Figure 2.1: The sketch of Varian/Veeco Gen-II solid source MBE system. 13

Figure 2.2: The RHEED pattern of (a) GaAs film and (b) GaSb QD growth on GaAs substrate. 15

Figure 2.3: The RHEED intensity oscillation of GaAs film growth for Ga growth rate calibration. 17

Figure 2.4: The growth rate versus the beam equivalent pressure of Ga cell. 18

Figure 2.5: The relationship of the doping concentration and cell temperature of silicon dopant cell. 19

Figure 2.6: The setup of PL measurement system. 20

Figure 2.7: The sketch of typical QDIPs device structure. 22

Figure 2.8: The setup of the dark current measurement system. 23

Figure 2.9: (a) The setup of the FTIR measurement system.
(b) The 45° waveguide measurement method. 24

Figure 2.10: The responsivity measurement setup. 25

Figure 2.11: The noise measurement setup. 26

CHAPTER 4

Figure 4.1: The schematic drawing of the device structure used in this study. Inset shows the band diagram of the QDs in the active region. 36

Figure 4.2: The TEM image of the ten InAs/GaAs QDs layers with 50nm barrier. Each barrier includes 47nm GaAs and 3nm $Al_{0.2}Ga_{0.8}As$. 36

Figure 4.3: The low temperature PL result of the sample. The transition peaks are at 1.11 and 1.17 eV. The ground state FWHM is around 50meV. 37

Figure 4.4: The scatter line shows the dark current activation energy at different voltages, and the straight line shows the kinetic energy of electrons across one barrier under uniform electric field. 38

Figure 4.5: The responsivity versus bias at different temperatures. 39

Figure 4.6: The noise spectrum at 130K and different bias voltages. 40

Figure 4.7: The current gain of the sample at different bias and temperatures. 41

Figure 4.8: The capture probability at different bias and temperatures. 42

Figure 4.9: The dark current (solid curve) and current gain (scatter curve) curve for the two samples with different doping concentration at 77K. 43

Figure 4.10: The calculated average extra carrier number $<N>$ in one QD at different temperature and voltages. 45

Figure 4.11: The quantum efficiency of the sample at different bias and temperature. 46

Figure 4.12: The quantum efficiency (solid curve) and $<N>$ (scatter line) at different temperatures and negative voltages. The vertical lines are used to indicate the voltage of quantum efficiency peaks. The peak quantum efficiency occurs around $<N>$=0.4. 47

CHAPTER 5

Figure 5.1: The low temperature (20K) PL result of single layer and multi-layer (vertically aligned ten layers with 10nm spacer). 51

Figure 5.2: The PL spectra of (a) single and (b) multi-layer samples at different temperature. 52

Figure 5.3: The temperature dependence of the peak energies of the PL spectra. The scatter curves are the experiment data, and the continuous curves are calculated results according to the Varshni law using the parameters (α, β) of InAs. 53

Figure 5.4: The FWHM of single and multi-layer samples at different temperature. 54

Figure 5.5: The cross-section TEM image of the device B. 56

Figure 5.6: The 40K photocurrent response spectra of sample A and B. 58

Figure 5.7: The 77K noise current gain of sample A and B as a function of the average electric field. 59

Figure 5.8: The normalized frequency response of photocurrent of sample A and B at 40K and 0.5V. 60

Figure 5.9: The quantum efficiency of sample A and B at 77K. 61

CHAPTER6

Figure 6.1: The schematic drawing of the device structure used in this study. Inset shows the band diagram of the QDs in the active region. 65

Figure 6.2: The surface AFM image of sample A (1μm×1μm).

Figure 6.3: The normalized photocurrent spectra of these four samples at 40K and 1V. 65

Figure 6.4: The 77K micro-PL and 1.4K PLE spectra of sample A. The inset shows the six electron states and possible intersubband transitions. 68

Figure 6.5: The PLE spectra of the four samples at 1.4K. 69

Figure 6.6: (a) The simulation structure of sample A. (b) The simulated electron states of angular quantum number *l=0, 1*. 71

Figure 6.7: The six electron states wavefunction. 72

Figure 6.8: The intersubband carrier transition oscillator strength (a) for $\Delta l=0$ (TM polarized), (b) for $\Delta l=1$ (TE polarized). 73

Figure 6.9: The photocurrent spectra of sample B at 40K and 1V for different polarization angle of the incident infrared light from the 45° polished facet on the detector. 74

Figure 6.10: The dark current density and responsivity of sample A and D at 77K. 76

Figure 6.11: The quantum efficiency and detectivity of sample A and D at 77K. 76

CHAPTER 7

Figure 7.1: The sample structure of GaSb/GaAs QDs in our study. 80

Figure 7.2: The source shutter operation sequence during GaSb QDs growth. And, the substrate temperature change procedure. 80

Figure 7.3: The surface AFM image of sample A, B, C, and D. The image size of sample A was 5μm×5μm, and the others were 1μm×1μm. Sample A, B, C and D were with 1, 2, 3 and 4 monolayer GaSb film. 82

Figure 7.4: The surface AFM image of sample E, F, D, and G. The image size of sample E was was 5μm×5μm, and the others were 1μm×1μm. Sample E, F, D and G was grew at 540℃, 520℃, 500℃ and 480℃. 83

Figure 7.5: The surface AFM image of sample H, D, I, and J with the image size 1μm×1μm. The V/III flux ratio is equal to 3, 5, 10 and 20. 84

Figure 7.6: (a) SK mode GaSb/GaAs QDs. (b) IMF mode GaSb/GaAs QDs. There misfit array at the GaSb QDs and GaAS substrate interface. 85

Figure 7.7: The schematic band structure of the GaSb/GaAs heterostructure in different excitation level. 86

Figure 7.8: The 20K PL response spectrum of the sample D at different excitation power. 87

Figure 7.9: Measured transition energy of sample A vs the cubic root of the excitation power. 88

Figure 7.10: PL emission spectrum of sample D at different temperature at 10mW excitation power. 89

Figure 7.11: The emission peaks energy level of WL and QDs at different temperature. 90

Figure 7.12: Product of Fermi-Dirac and Gaussian distribution functions at different temperatures. 90

Figure 7.13: Photoluminescence spectra of (a) sample A and (b) sample B at 20K. 92

Figure 7.14: Measured transition energy versus the cubic root of the excitation power. The interceptions of the extrapolated lines with the y axis give the transition energies at thermal equilibrium. 93

Figure 7.15: Transition energies of quantum wells with 1, 2 and 3 ML of GaSb. The measured result is compared with the theoretical result. 95

CHAPTER 8

Figure 8.1: The sample structure of GaSb on Silicon substrate in our study. 97

Figure 8.2: The surface AFM image of these samples. The image size is 10μm×10μm with the 30nm scale bar. 98

Figure 8.3: The 20K PL response from the 8nm $In_{0.2}Ga_{0.8}Sb$/GaSb QW. The FWHM of sample C is 11.2meV and peak is at 0.177eV. 99

Figure 8.4: High resolution XRD (004) rocking curve of GaSb on Silicon. The

FWHM of the sample C is 490 arcsec. 100

Figure 8.5: Cross-section HR-TEM image of the GaSb/AlSb superlattice on Silicon substrate in sample C. In area 1, 2 and 3 the dislocations merge or stop at the superlattice interface. 102

Chapter 1

Introduction

The III-arsenic semiconductors and their related quantum structure have been widely used in optoelectronic and high-speed device application. With the mature heterojunction epitaxy, the quantum well laser diode, the quantum well infrared photodetectors (QWIPs), heterojunction bipolar transistor (HBT), and high electron mobility transistor (HEMT) have been realized [1, 2]. Besides, the self-assembled defect-free 3-D confined InAs/GaAs quantum dot system with S-K (Stranski-Krastanov) mode growth method has also been successfully developed in the past decade. The physics of the quantum dot has been widely studied, and the quantum dot also has been used in many different optoelectronic devices, such as single photon emitter, quantum dot lasers, and infrared detectors [3]. Recently, III-antimonide compounds have been regarded as potential materials for applications in ultra high-speed devices and long-wavelength photonic devices due to their high electron mobility and small band gap energies [4]. Furthermore, the heterostructures composed of antimony and other III-V compounds, such as arsenic, have also been of physical interest because of the unconventional type-II and type-III band alignment [5-7].

1.1 Infrared technology

Any object with nonzero temperature will emit radiation. The radiation spectrum peak of lower temperature object is at longer wavelength. For the detection of people in the night or the space application, the infrared detection technology is important. In the past two decades, the quantum well made by the III-V material has been widely used in the infrared detection technology. Furthermore, the quantum dot infrared photodetectors (QDIPs) is regarded as the potential structure to overcome the drawbacks of QWIPs.

1.1.1 Blackbody radiation

All of objects with nonzero temperature generate thermal radiation which could be approximated as a blackbody with an emissivity factor smaller than one. The blackbody is an ideal radiation source, and the radiation spectrum is the function of temperature. The radiation power density spectrum of the blackbody is expressed as:

$$Q(\lambda,T)=\frac{2\pi hc^2}{\lambda^5}\cdot\frac{1}{e^{hc/\lambda kT}-1} \tag{1.1}$$

where h is the Plank's constant, k is the Boltzmann constant, c is the speed of light, λ is the wavelength, and T is the blackbody temperature. Fig. 1.1 shows the blackbody radiation spectra at 350K, 300K, and 250K. The peak intensity wavelength varies from 8.5μm to 11.5μm. The moisture (H_2O) and carbon dioxide (CO_2) in atmosphere will absorb the infrared. Therefore, the infrared transmittance spectrum of the atmosphere is not flat. Fig. 1.2 shows the transmittance spectrum of atmosphere. There are two transparent windows of infrared: 3~5μm (MWIR) and 8~13μm (LWIR). Therefore, the detection wavelength of infrared detectors which are used on earth must fall in the transparent window. For the space application, all of the detectors with different detection wavelength can be used due to the vacuum environment.

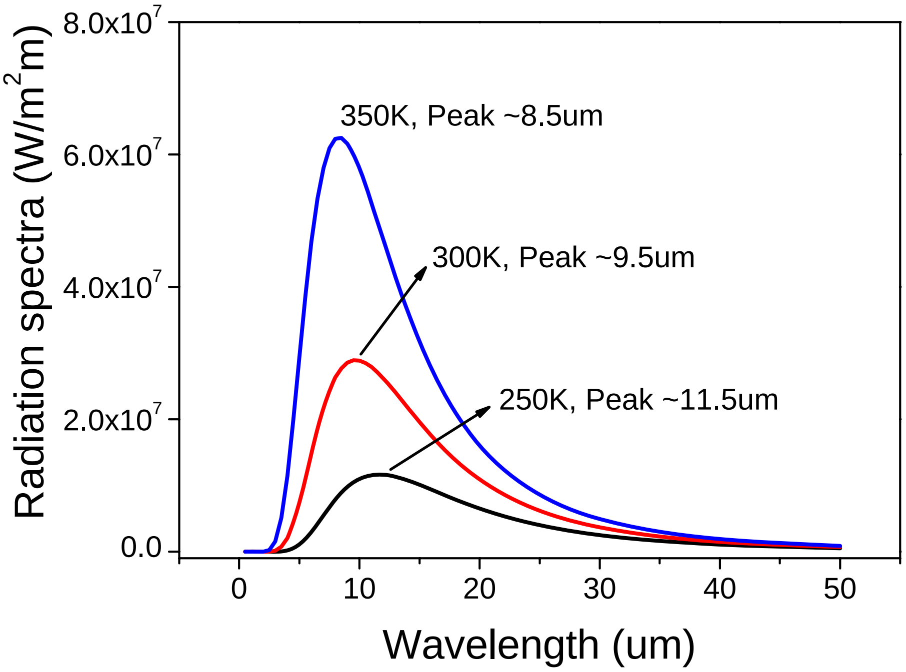

Figure 1.1: The blackbody radiation spectra at 350K, 300K, and 250K. The peak intensity varies from 8.5μm to 11.5μm.

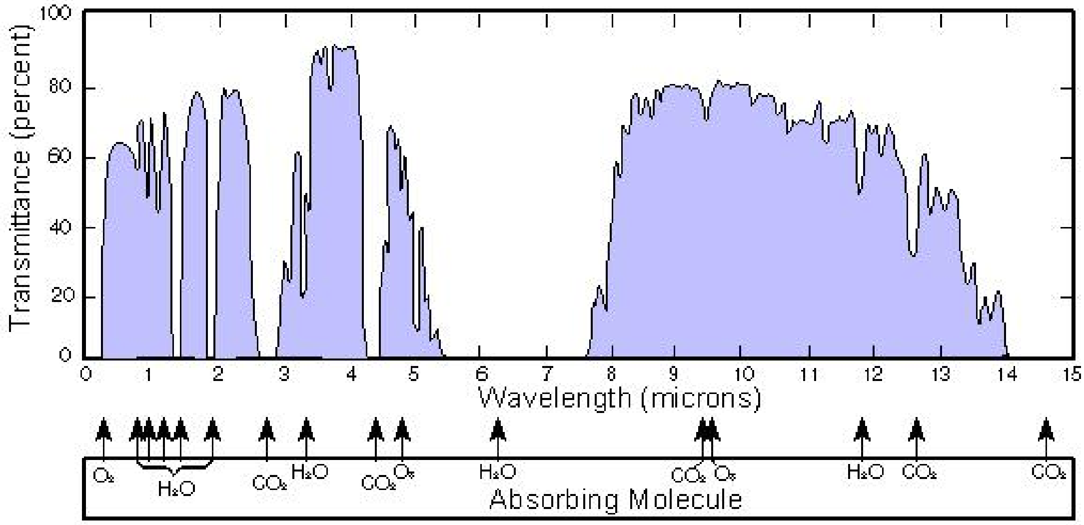

Figure 1.2: The atmosphere transmittance spectrum of infrared.

1.1.2 Infrared detection technology

There are two major detection types of the infrared radiation: thermal and photon detector. The detection mechanism of thermal detector is the physics characteristics change after the absorption of infrared radiation, such as resistance, thermoelectric, and charge. Bolometers and microbolometers are based on the resistance change. Thermocouples and thermopiles use the thermoelectric effect. In general, the thermal detector could be operated at higher temperature, but the response time is much longer due to the limitation of the thermal conductivity.

There are three types of the photon detectors, including QWIPs (or QDIPs), II-VI photodiodes, and type-II InAs/GaSb superlattice photodiodes. The operation of the photon detectors is based on the carrier transition from lower energy state (valence band) to higher energy state (conduction band) and becomes free carrier. The free carrier (electron) concentration increase causes the photo current increase. The major advantage of the photon detector is the shorter response time than thermal detector because the carrier transition process is faster than the physics property change. However, the photon detectors must be operated at low temperature in order to reduce the thermal noise. The advantages and limitations of these three type detectors are listed in table 1.1 [8].

Detector type	Advantages	Limitations
QWIPs	Mature III-V technology Large, uniform FPA	High dark current Low quantum efficiency Non-normal absorption
II-VI (MCT)	High detectivity High quantum efficiency Low dark current	High device defect Expensive substrate Epitaxy difficulty
InAs/GaSb SLS	High detectivity High quantum efficiency	High dark current Epitaxy difficulty

Table 1.1: Advantages and limitations of different type infrared detectors.

The major advantages of QWIPs are the mature III-V epitaxial technology and large area uniformity, which is important for the focal plane array (FPA) application. However, the high dark current, low quantum efficiency, and the non-normal incident radiation absorption limit the device performance.

1.1.3 Overview of QWIPs and QDIPs

The intersubband infrared absorption of the GaAs/AlGaAs QW was first observed by West and Eglash in 1985 [9]. The absorption peak at 8μm and 10μm was observed in the 65Å and 82 Å GaAs/AlGaAs QW. Two years later (1987), the first QWIPs device was demonstrated by Levine *et al.* [10]. The absorption of the 65 Å GaAs/AlGaAs QW was 10.8μm with a responsivity of 0.52 A/W. In 1991, the first 128×128 GaAs/AlGaAs QWIP FPA was fabricated [11]. In 2003, the large 640×514 four detection bands IR FPA with 99.9% of the pixels working was fabricated by JPL [12]. However, the operation temperature of QWIPs is difficult to further increase and the device is insensitive for the normal incident radiation. These drawbacks limit the application of QWIPs.

After the high quality self-assembled quantum dot (QD) epitaxial technology was carried out, the QD is assumed as potential active layer structure for the intersubband infrared detector application. Due to the three dimensional confinement of the carrier, the QDIPs are sensitive to normal incident infrared radiation. And, because of the discrete energy level of the QD, the carrier intersubband relaxation time is much longer than that of QW. The longer relaxation time would enhance the device current gain and reduce the detector noise. Thus, the QDIPs are of the great potential to surpass the disadvantages of the QWIPs [13].

The infrared absorption of the QDs had been observed by different method in different groups. Drexler *et al.* studied the intersubband far-infrared absorption by a capacitance spectroscopy technique coupled with a far-infrared spectrometer [14]. Phillips *et al.* reported the far-infrared absorption of Si-doped InAs QDs by Fourier Transform Infrared (FTIR) spectrometer [15]. Berryman *et al.* studied the mid-infrared intersubband absorption in InAs QDs by photo conductivity measurement method [16]. And, Chua *et al.* investigated the polarization dependence of the intersubband absorption in InAs QDs by a FTIR spectrometer [17].

In 1998, several reports of the InAs/GaAs QDs as active structure intersubband photoconductive detectors were published. Phillips *et al.* measured the 17µm photo response signal by a FTIR and a low-noise amplifier measurement system [18]. Maimon *et al.* demonstrated the responsivity signals in the different polarization infrared radiation, and the carrier transition states were also studied [19]. Pan *et al.* showed the response signals were from E_0 to E_1 (13µm) and E_0 to E_2 (11µm), and this device showed a peak detectivity of 1×10^{10} cm-$Hz^{0.5}$/W at 40K [20]. Xu *et al.* studied the electro-optic characteristics of the QDIPs, and showed the ratio of TE (s-polarization) and TM (p-polarization) mode [21].

Except for the typical vertical QDIPs, the lateral QDIPs, which carriers transport direction is perpendicular to growth direction, had been also studied [22]. The lateral QDIPs was predicted of higher responsivity than vertical QDIPs due to the higher current gain. However, the lateral QDIPs was more difficult to fabricate the FPA, because the two electric contact pads were fabricated at the same side.

In 2001, the performance of the QDIPs was improved by inserted the high band gap material ($Al_xGa_{1-x}As$) in the active region to reduce the device dark current and increase the device performance. Wang *et al.* demonstrated the low dark current and high detectivity (2.5×10^9 cm-$Hz^{0.5}$/W at 77K, ~6µm) QDIPs by capping a thin $Al_{0.2}Ga_{0.8}As$ layer after the QDs [23]. Chen *et al.* compared two different structures: the InAs QDs surrounded by GaAs or AlAs/GaAs super lattice. The ratio of I_{pc}/I_{dark} of latter structure showed more than two orders higher than former one [24]. Stiff *et al.* used a single $Al_{0.3}Ga_{0.7}As$ barrier as current blocking layer to reduce the dark current [25]. The device showed a detectivity of 3×10^9 cm-$Hz^{0.5}$/W at 100K, and it could be operated up to 150K. With the different active structure design, encouraging results have been demonstrated with operation temperatures over 200K [26-28] and even up to room temperature [29, 30]. The 640×512 pixels long wavelength (8.1μm) QDIP FPA has fabricated in 2007 by Gunapala *et al* [31]. The noise equivalent temperature difference is of 40mK at 60K operation temperature.

1.2 GaSb/GaAs quantum structure and GaSb growth on Silicon substrate

1.2.1 Semiconductor heterojunction

A heterojunction is the junction of two different semiconductor materials with different bandgap energy. In the ideal case, the interface is strain-free and the bandgap energy is not changed. Due to the bandgap energy, the work function, and the electron affinity difference in different material, the heterojunctions have three kinds of band alignment, including type-I, type-II and type-III [32, 33]. Fig. 1.3 shows the ideal case energy band alignment of these three kinds of heterojunction. By controlling the composition of the group-III and V in ternary or quaternary semiconductor, we can adjust the band alignment in the heterostructure device.

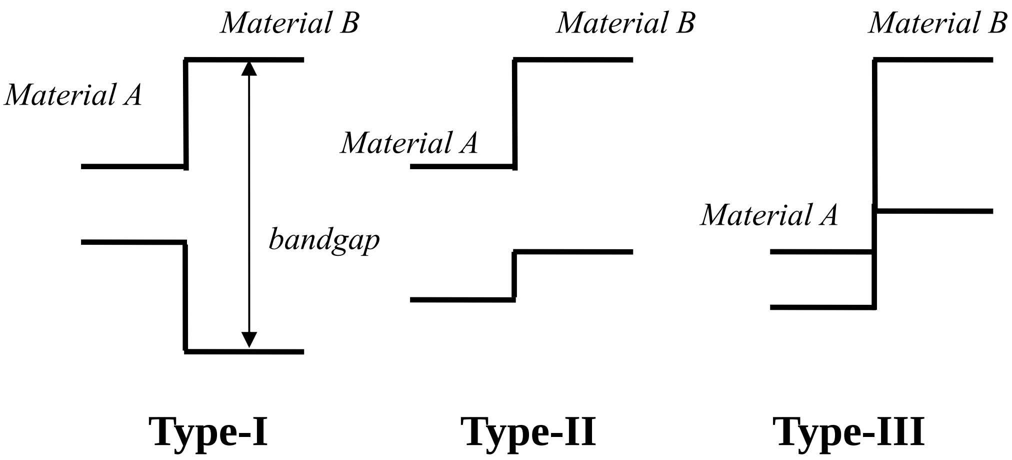

Figure 1.3: The schematic drawing of the type-I, type-II and type-III heterojunction.

The quantum wells and self-assembled quantum dots made by GaSb or InAs embedded in GaAs matrix show the different band alignment. The former is the type-II band alignment, and the later is the type-I. The major difference of the type-II and type-I band alignment is the spatially separate electrons and holes. Fig. 1.4 shows the GaSb and InAs quantum structure embedded in GaAs matrix band alignment system. The spatially separate electrons and holes will result in longer carrier life time.

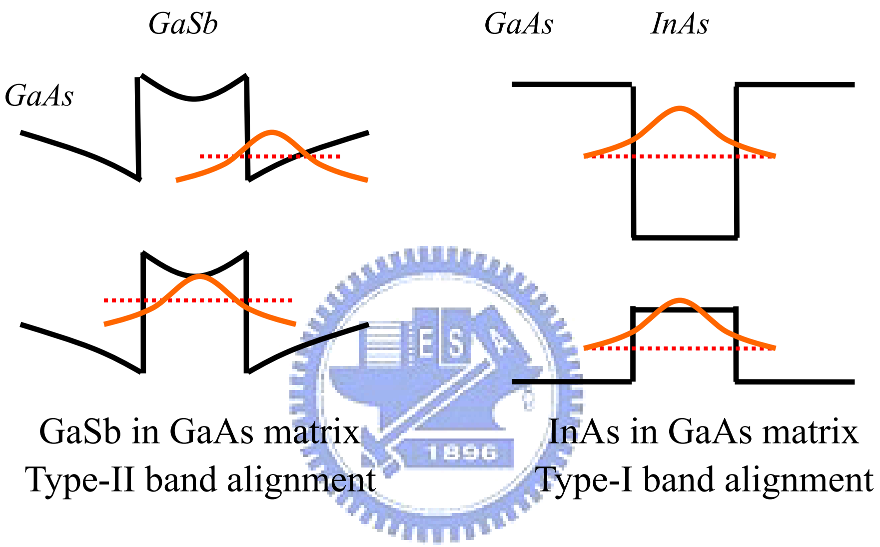

Figure 1.4: The schematic drawing of the band alignment of GaSb and InAs in GaAs matrix.

1.2.2 GaSb base optical and electronic devices

The Sb-base device has the advantages of narrow band gap and high electron mobility over conventional GaAs or InP base devices [34, 35]. Fig. 1.5 shows the band gap energy versus lattice constant. The Sb-base (red rectangular) is the next generation of the long wavelength laser diode and high speed device application. The GaSb based laser diode can emit mid-infrared (2~5μm) region with different structure. The type-I InGaAsSb/AlGaAsSb quantum well emits at the 2~2.6μm region. The type-II InGaAsSb/GaSb, type-III InAs/InGaSb, and InAl/InGaSb/AlSb, which are all based on GaSb substrate, can emit beyond 2.6μm. Moreover, the Sb based HEMTs and HBTs can attain higher operation frequency and lower noise. The HEMTs with InAs or InSb-QW channel on GaSb substrate shows the much higher operation frequency than the GaAs/AlGaAs HEMT devices.

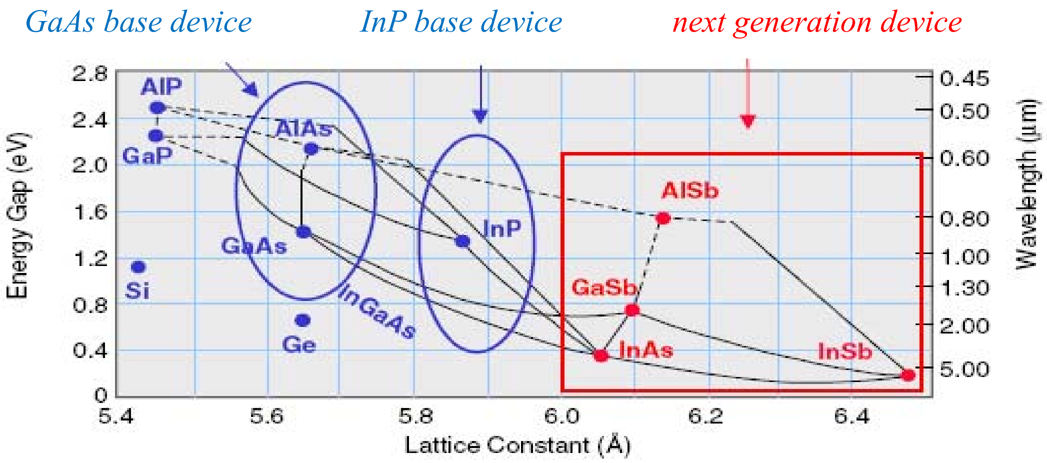

Figure 1.5: Energy bandgap versus lattice constant of the III-V semiconductor.

The Sb-base devices are grown on GaSb substrate, but the substrate is expensive. Thus, the cheaper GaAs substrate is used for the Sb-base device with a thick AlSb buffer layer. Furthermore, the silicon substrate is much cheaper and more hardness than GaAs substrate. In recent years, the growth of GaSb on Silicon substrate was reported by K. Akahane *et al.* [36] and G. Balakrishman *et al.* [37].

1.3 Organization of the Thesis

The thesis is separated into two parts: one is the QDIPs device based on the InAs/GaAs QDs (chapter 3, 4, 5, and 6), and the other is the GaSb material study (chapter 7 and 8). Due the high current gain of the QDIPs, the device can be operated at higher temperature and even up to room temperature. However, only a few studies are executed to study the high gain behavior. Besides, the lower quantum efficiency is still a drawback in the device application. In our study, we try to increase the quantum efficiency and enhance the roll-off frequency at the same time by using the vertically coupled QDs in the active layer. Furthermore, the carrier intersubband transitions will influence the quantum efficiency, photocurrent spectra, and transition oscillator strength. These topics are also studied in the thesis. In addition to the QDIPs, the GaSb material is also studied. The Sb-based semiconductor is regarded as the potential material to execute the higher speed device and longer wavelength laser. Two studies are executed in this thesis, including GaSb/GaAs QDs and the GaSb growth on silicon substrate.

In chapter 2, the experimental techniques are described, including molecular beam epitaxy (MBE) system, analysis techniques (AFM, PL, and XRD), QDIPs device processing, and QDIPs measurement system.

In chapter 3, the fundamentals of QDIPs are described. The intersubband absorption, quantum efficiency, current gain, responsivity, dark current, noise, and detectivity are discussed.

In chapter 4, the temperature dependent responsivity of QDIPs is discussed. The responsivity of QDIPs shows a very different behavior compared to that of QWIPs. In QWIPs, the responsivity keeps almost constant at different device temperatures and changes linearly with the bias voltage. On the contrary, in QDIPs, the responsivity increases dramatically with both voltage and temperature. Only few studies were executed with the experimental data. In this chapter, a detailed analysis of the responsivity was done based on the current gain measurement to explain the responsivity temperature dependent behavior in QDIPs.

In chapter 5, the vertically coupled QDIPs were studied. The performance of QDIPs is limited by the low quantum efficiency which is critical to the performance. In addition to quantum efficiency, poor frequency response of the responsivity in QDIPs was also reported with the roll-off frequency lower than 1K Hz especially at lower temperatures. The roll-off frequency of QDIPs is a few orders of magnitude lower that of QWIPs. The long RC time constant originated from the charging process of the electrons into the quantum dots deteriorates the frequency response. This phenomenon limits the use of QDIPs in some military and space applications where the high speed detection is needed. In this chapter, the vertically coupled QDs were used as the active layer in the QDIPs to solve the issues mentioned above.

In chapter 6, the QDIPs with an additional thin $Al_{0.2}Ga_{0.8}As$ layer near the QDs were studied. With the thin $Al_{0.2}Ga_{0.8}As$ layer, the carrier transitions of the QDIPs could be engineered. One of the transitions of the simple InAs/GaAs QDIPs would be suppressed. Thus, a much narrow photocurrent spectrum was observed when the $Al_{0.2}Ga_{0.8}As$ layer is closer to the QDs. The fractional spectra width was reduced to only 10% and enhanced the quantum efficiency. The thin $Al_{0.2}Ga_{0.8}As$ layer also reduces the device dark current, and enhances the device performance.

In chapter 7, the self assembled GaSb QDs embedded in GaAs matrix were studied. The GaSb/GaAs QDs show a type-II band alignment in which the electron and hole is spatially separated. The morphology of the surface QDs and photoluminescence of the embedded QDs at different excitation power and temperature were studied. Furthermore, the valence band offset (VBO) between GaSb and GaAs has been studied by the observation of discrete monolayer light emission.

In chapter 8, the GaSb material growth on Silicon substrate with different buffer layer structure was studied. The GaSb crystal quality and $In_{0.2}Ga_{0.8}Sb$ QW photo emission intensity was analyzed by x-ray diffraction and photoluminescence, respectively. The sample with superlattice buffer layer structure shows the best quality.

Chapter 2

Experimental Techniques

In this chapter, the experimental techniques used in my experiment are presented. It consists of three parts: molecular beam epitaxy (MBE) system for sample growth, the material characterization analysis techniques, and quantum dot infrared photodetectors (QDIPs) processing and measurement.

2.1 Molecular Beam Epitaxy

2.1.1 Introduction to our MBE system

The epitaxial system in our laboratory consists of two growth units. One is Varian Gen-II system, and the other is Veeco Gen-II system. These two growth units are linked by an extension chamber. Fig. 2.1 shows a sketch of the integral MBE system. Each system consists of three ultra high vacuum (UHV) chambers, including growth chamber, buffer chamber and load-lock chamber. The buffer chamber is connected to the other two chambers and isolated by gate valve.

The pumps used in our MBE system is oil-free pumps for reduce the contamination. In order to maintain UHV, croy-pump, ion-pump, and titanium sublimation pump (TSP) are used in growth chamber, ion-pump and TSP pump are used in buffer chamber, and croy-pump is used in load-lock chamber. Besides, in order to pump down the system from atmospheric pressure, a scroll and turbo-molecular pump is connected to these three chambers and isolated with three all metal angle valves.

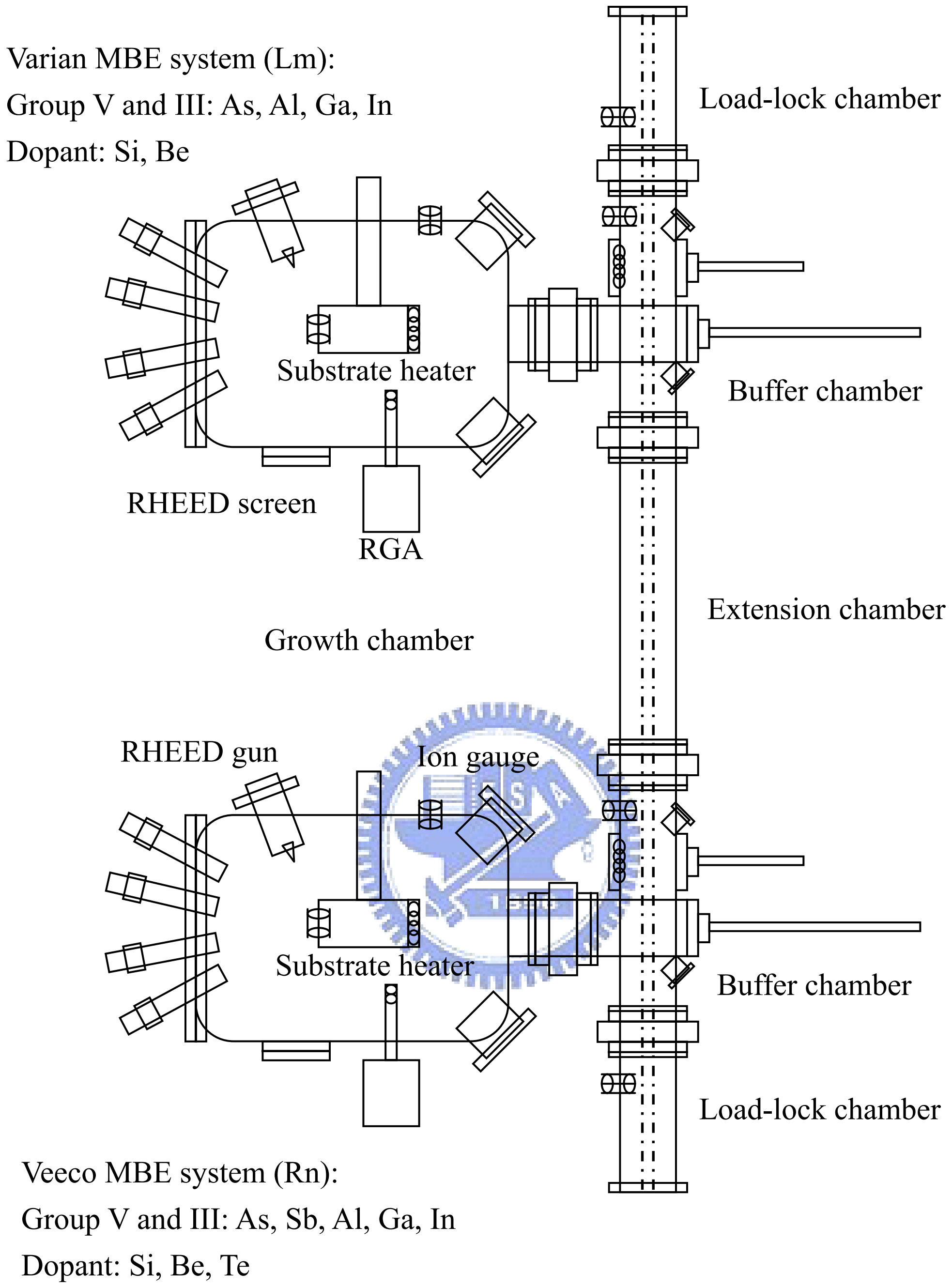

Figure 2.1: The sketch of Varian/Veeco Gen-II solid source MBE system.

One of the integral MBE systems is called Lm-MBE (Varian Gen-II), and the other is called Rn-MBE (Veeco Gen-II). The Lm-MBE system consists of eight sources. There are arsenic (As) cracker cell for group-V source and aluminum (Al) cell, gallium (Ga) cell, and indium (In) cell for group-III source. Besides, the silicon

(Si) cell and beryllium (Be) cell are used for different doping. In additional to the sources in Lm-MBE system, the group V material (antimony: Sb) valve cracker cell and a tellurium (Te) cell for n-type doping are added in Rn-MBE system.

Two temperature control zones of the group V valve cracker cell of As and Sb, bulk and cracking zone, are controlled by individual filament. The bulk zone of As is usually operated between 350℃ and 400℃. This cell can be operated at different mode to supply As_2 or As_4 by controlling the cracking zone temperature varying from 840℃ to 500℃. The beam equivalent pressure (BEP) is controlled by the needle valve. The bulk zone of Sb is operated between 500℃ and 600℃, and the cracking zone is operated at 1050℃ to supply the Sb. Two designs are used for the group III source cell, including Kundsen cell (K-cell) and SUMO cell. The SUMO cell has two filaments to control bulk and tip zone. We keep the tip temperature and vary the bulk temperature to control the beam flux. The K-cell only has one filament to control the beam flux. The group III Ga and In source are hot lip design and Al is cold lip design due to the different material characteristic.

There are two analysis instruments in the growth chamber. One is residue gas analyzer (RGA), and the other is the reflection high energy electron diffraction (RHEED) monitor. The RGA is used to analyze the residue gas in the chamber. The RGA monitor can also serve as leakage detector by keeping the detection range of the atomic mass unit (AMU) to helium (He, 4). The helium gas is usually used to detect the chamber leakage, due to the small size of atom and little amount in atmosphere. The RGA monitor is a very sensitive leakage detector, but it can only be operated when the chamber at ultra high vacuum (pressure lower than 1×10^{-8} torr). The RHEED allows us to in-situ monitor the surface reconstruction structure. By using a high energy electron beam with an angel, the reconstruction structure of the sample surface (typically a few monolayers) can be analyzed with the diffraction patterns. It makes the substrate surface native oxide desorption easy. It indicates the oxide free surface when the surface reconstruction pattern appeared. Besides, it is useful for quantum dot (QD) growth by observing the RHEED pattern transition. When the growth mode changes from layer to dot, the RHEED pattern will change from streaky to spotty pattern. Fig. 2.2 (a) (b) shows the layer and dot RHEED pattern. Also, by observing the RHEED pattern intensity oscillation period, we can calibrate the material growth rate. The growth rate calibration will be discussed later.

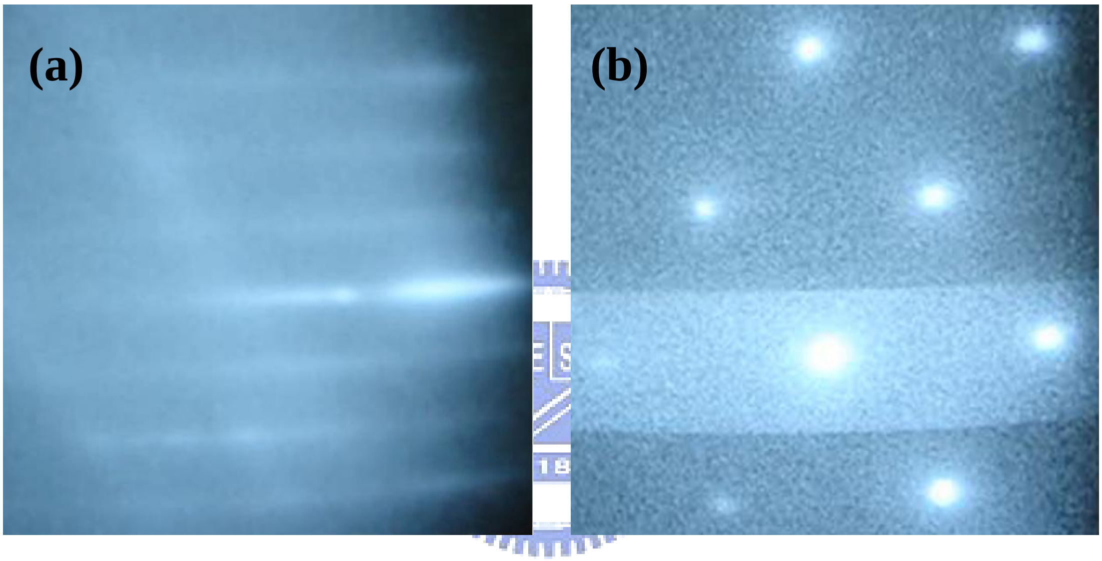

Figure 2.2: The RHEED pattern of (a) GaAs film growth, and (b) GaSb QD growth on GaAs substrate.

2.1.2 Pre-growth procedure

In order to maintain the chamber cleanness and obtain high quality epitaxial film, a standard treatment procedure for wafer before growth is important and necessary. The epi-ready substrate is mounted on indium free Mo spring substrate holder, and then put into load-lock chamber. In load-lock chamber, the wafer will be baked at 200℃. The moisture on wafers and sample holders will be baked out during the bake process. These wafers will be transferred to buffer chamber when the load-lock chamber pressure lower than 1×10^{-8} torr after bake out and pump down process. The each wafer will be baked up to 400℃ more than 4 hours in buffer chamber in order to remove the organic species. Usually, the cleanness of wafers is judged by the chamber pressure (chamber pressure must be lower than 3×10^{-9} torr). After the 400℃ bake process, the wafer can be transferred to growth chamber to grow. A thin native oxide exists on the substrate surface when the substrate exposure at atmosphere. The native oxide will not be removed during the bake process in load-lock and buffer chamber. Before growth, the native oxide of substrate is desorbed by heating the wafer up to the suitable temperature under arsenic phase. The desorption temperature depends on the substrate type. The desorption temperature is 610℃ for GaAs and 510℃ for InAs substrate.

Our MBE system is served as III-V semiconductor material growth. But, we also use the silicon substrate for sample growth. The native oxide of silicon is hard to remove by heating in our system. The native oxide of silicon must be removed before loading. We use diluted HF solution to clean the silicon substrate, and load it into load-lock chamber as soon as possible to prevent the native oxide formation. The followed pre-growth procedure is 200℃ bake in load-lock chamber, and 500℃ in buffer chamber. Before growth, the silicon wafer is heated up to 800℃ (substrate thermal couple temperature, it is our system limit).

During the sample growth, the growth chamber is cooled down by continuous liquid nitrogen flow. The cooled cryo panel in growth chamber is served as a powerful absorption pump to maintain the system vacuum.

2.1.3 Growth rate and doping concentration check

In general, we use the RHEED intensity oscillation on non-rotate substrate to calibrate the group-III material (Al, Ga, In) growth rate. A GaAs wafer with (001) orientation is used to check the Al and Ga cells growth rate, because the AlAs (5.66 Å) and GaAs (5.65Å) have almost the same lattice constant. Besides, the InAs wafer with

(001) orientation is used to check In cell growth rate. Fig. 2.3 is the RHEED intensity oscillation of Ga cell. One oscillation period means one monolayer of GaAs.

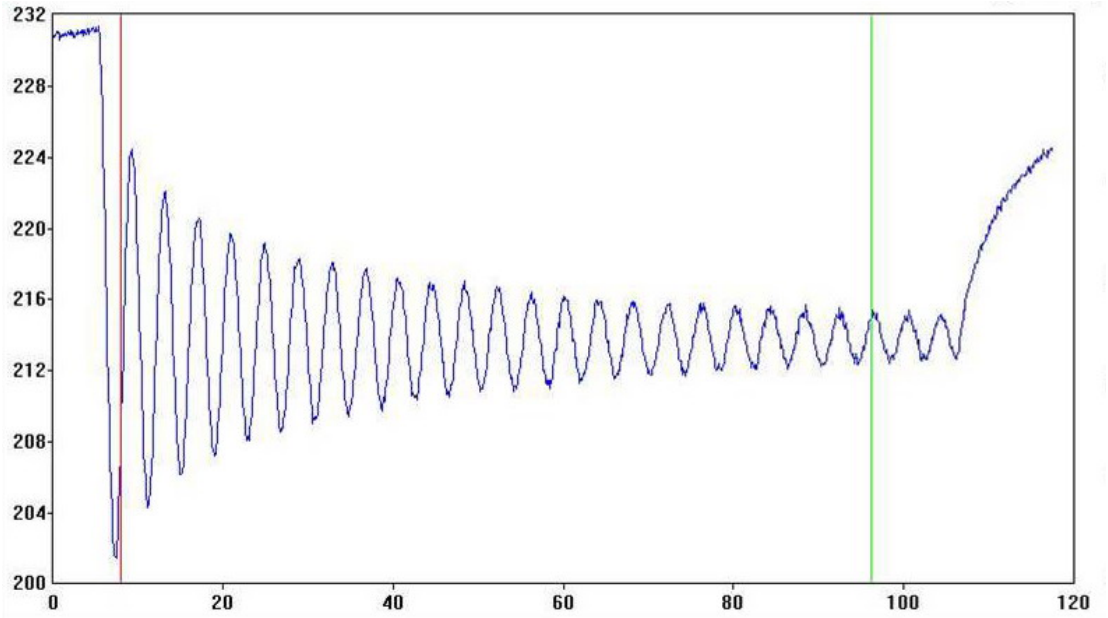

Figure 2.3: The RHEED intensity oscillation of GaAs film growth for Ga growth rate calibration.

For carefully designed source cell, a fixed cell temperature gives a stable source beam flux. We use a beam flux monitor ion gauge to measure the source beam equivalent flux pressure (BEP). In Varian (Veeco) Gen-II MBE, the beam flux monitor gauge and substrate holder can exchange their location exactly by rotating the substrate manipulator (CAR). First, we measure BEP at different temperature of each cell. Then, we measure the RHEED intensity oscillation at different cell temperature. The growth rate is determined by the oscillation period. Finally, we can get the relationship between the BEP and growth rate. Fig. 2.4 shows the growth rate versus the beam equivalent pressure of Ga cell. We can see that the growth rate and the BEP have very good linear dependence. Before each sample growth, the desired growth rate is obtained by adjusted the cell temperature to reach the corresponding BEP.

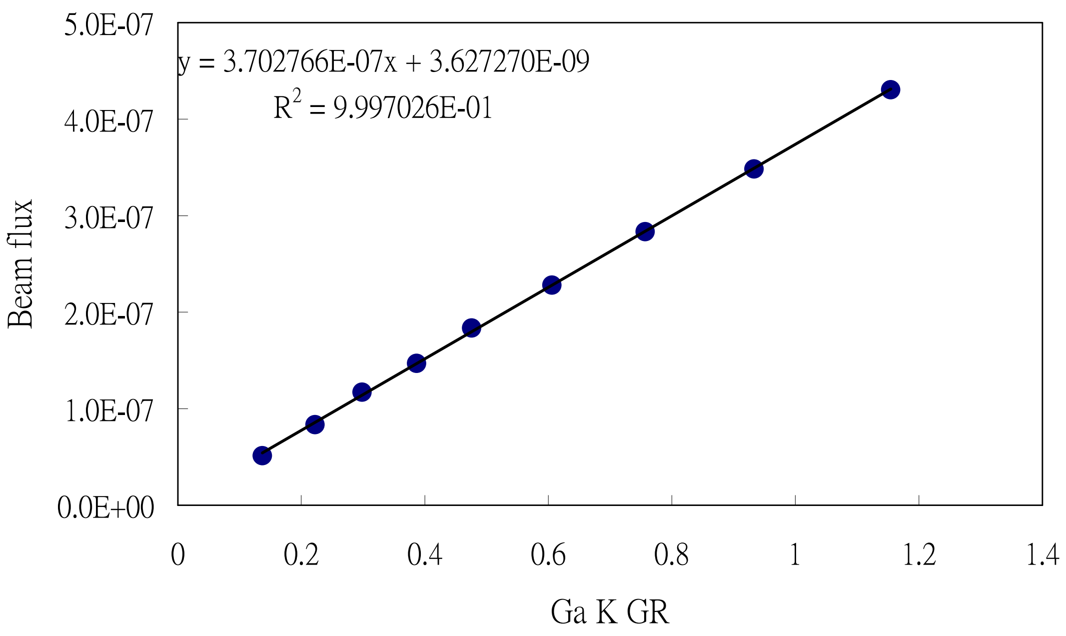

Figure 2.4: The growth rate versus the beam equivalent pressure of Ga cell.

When sample growth, the substrate will rotate in order to obtain uniform material composition and flat heterointerface in the whole wafer. However, the wafer would not rotate during the growth rate calibration.

Under 1μm/hr growth rate, the n-type (Si, Te) and p-type (Be) doping concentration for GaAs are calibrated with the etched C-V or Hall measurement for several temperature of the dopant cells. We assume the evaporated amount of the dopant material is the stable at different cell temperature, because the BEP of dopant material is not detectable of our beam flux monitor gauge. Fig. 2.5 shows the relationship between cell temperature and doping concentration of n-type silicon doping. During sample growth, the doping concentration for a definite growth rate can be calculation easily.

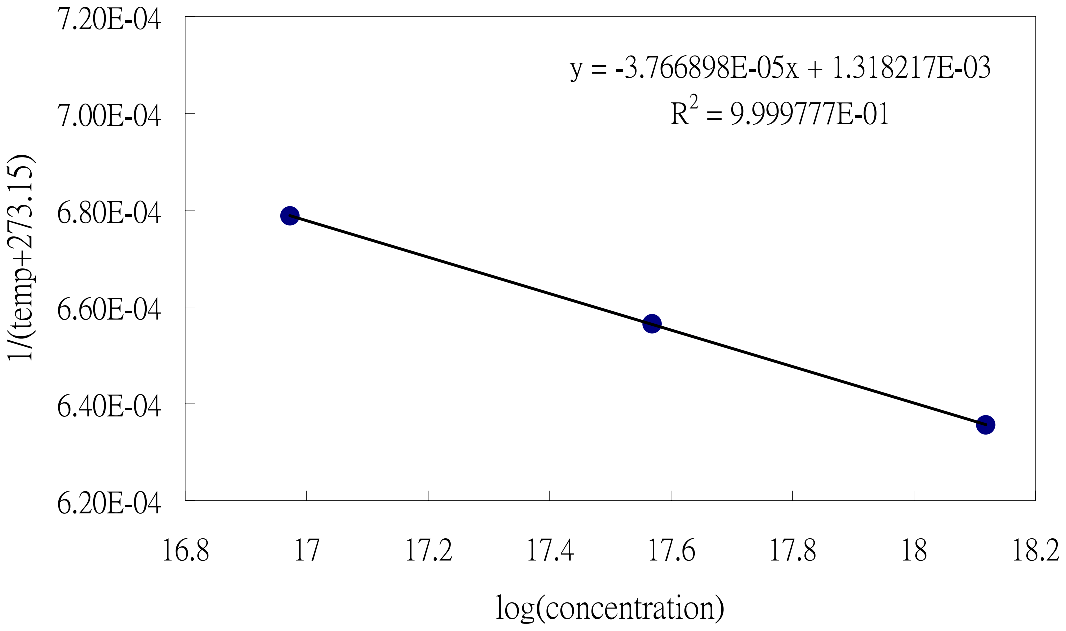

Figure 2.5: The relationship of the doping concentration and cell temperature of silicon dopant cell.

2.1.4 Growth condition

The group-V/group-III BEP ratio must be kept at suitable range for high quality epitaxial material. The typical V-III ratio is 10~20 for III-arsenic and 2~5 for III-antimonide. In general, the suitable growth temperature for 2-D layer of AlAs, GaAs, InAs, GaSb, and InSb are about 600℃, 580℃, 500℃, 500℃ and 450℃, respectively. However, for the 3-D structure (InAs or GaSb quantum dots), the QDs characteristics (size and density) is highly dependent on the growth conditions, including III/V ratio, temperature, and growth rate.

2.2 Material Characteristics Analysis

2.2.1 Atomic Force Microscope

The Veeco D3100 tapping mode atomic force microscope (AFM) system is used in our study. A QD layer is grown on the sample surface with the same growth condition with the active layer QDs for AFM study. By the AFM study, the density of

QDs can be obtained. However, due to the capping layer different (no capping layer on the surface QDs), the size of QDs is not the same. By cross-section transmission electron microscope (TEM) study, the size of the surface QDs is larger than the embedded layer QDs.

2.2.2 Photoluminescence

Photoluminescence (PL) is a useful non-destructive optical technique for analyzing the semiconductor material characteristics. The impurity level, defects, band gap and crystal quality will be obtained in the PL study. We use an Argon laser to generate electron-hole pairs in the material. The emission occurs when the electron-hole pair recombines. Fig. 2.6 shows the schematic drawing of the PL measurement system. In our conventional PL system, the laser spot size is about 50μm in diameter. When the excitation power density increase, the laser will heat the sample. In order to obtain the high power density information, we use micro-PL system, which laser spot size is about 2μm in diameter, to increase the excitation power density and avoid the heating effect.

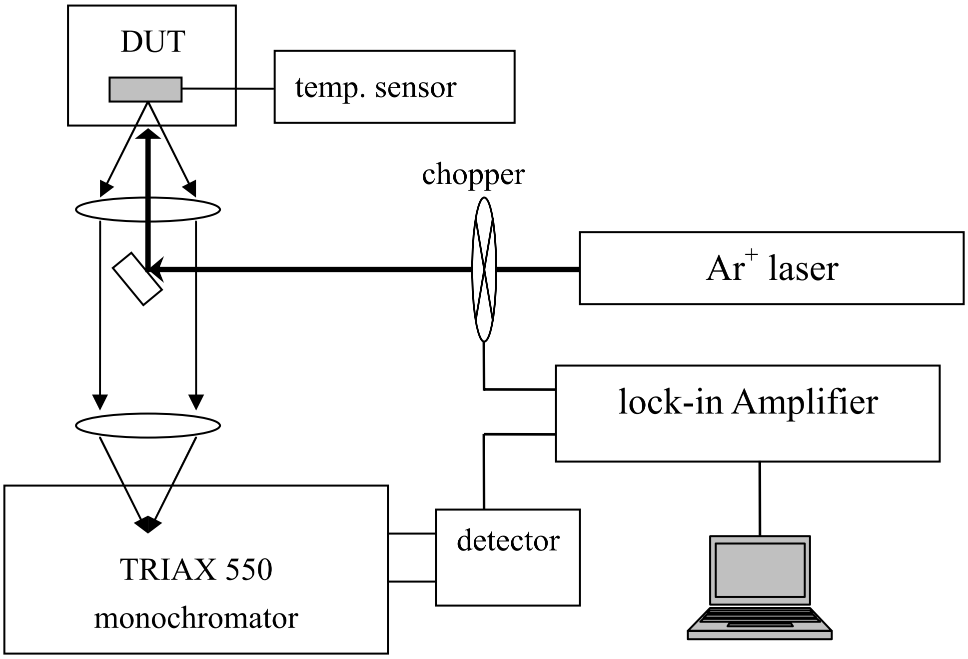

Figure 2.6: The setup of conventional PL measurement system.

2.2.3 X-Ray Diffraction Analysis System

The Bede D1 high resolution X-Ray diffraction meter (HRXRD) system is used to measure the crystal structure information, such as lattice constant and layer composition. We use the high resolution ω-2θ scan mode to measure the GaSb epi-layer on silicon substrate quality. In general, we measure the GaSb (004) curve full width at half maximum (FWHM) to analyze the epitaxial film quality.

2.3 QDIPs Device Process and Measurement

Unlike the QWIPs, no grating is fabricated on the device surface. We measure the normal incident absorption characteristics. The QDIPs device fabrication is done by standard lithography, wet etching and metallization process. The device mesa size is 370μm×260μm with a 200μm×200μm square light window. Fig. 2.7 shows the standard QDIP device structure and the inset shows the top view of the device after processing. The wet etching solution is H_2SO_4: H_2O_2: H_2O=1: 8: 80, and the etching rate is about 80 Å/sec for GaAs epitaxial layer. The n-type ohmic contact metal is Ni/Ge/Au (300Å/700Å/3000Å) evaporated by single E-gun evaporation system at the top and bottom of the mesas. The bottom contact is referred as ground contact in all measurement. A good ohmic contact can be obtained by a rapid thermal annealing at 380℃ for 30 sec. After processing, the device is mounted on a holder with good thermal conductivity and connected to electric feedthrough by gold wire bonding. The QDIPs package is cooled with close cycle helium refrigerator for different temperature measurement.

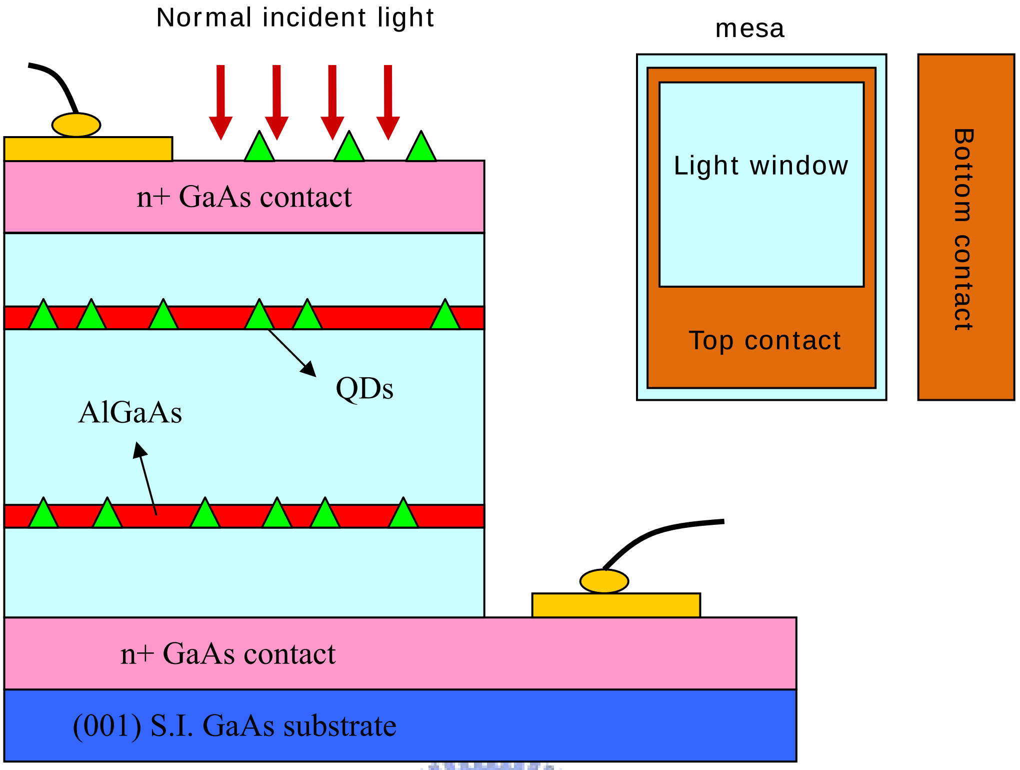

Figure 2.7: The sketch of typical QDIPs device structure and the top view of the device after processing.

Three important characteristics of QDIPs device are measured to judge the device performance, including dark current and 300K background photocurrent, device absorption spectrum and responsivity, and device noise level and detectivity.

In our laboratory, the Keithley 236 is used to measure the dark current and background photocurrent. The cryostat is used to measure the background photocurrent at different temperature. Besides, we put the sample at the air phase of liquid helium dewar flask and a temperature sensor is mounted near the sample. By controlling the distance between the sample and liquid helium surface, we can measure the dark current at different temperature. Fig. 2.8 shows the dark current measurement system setup.

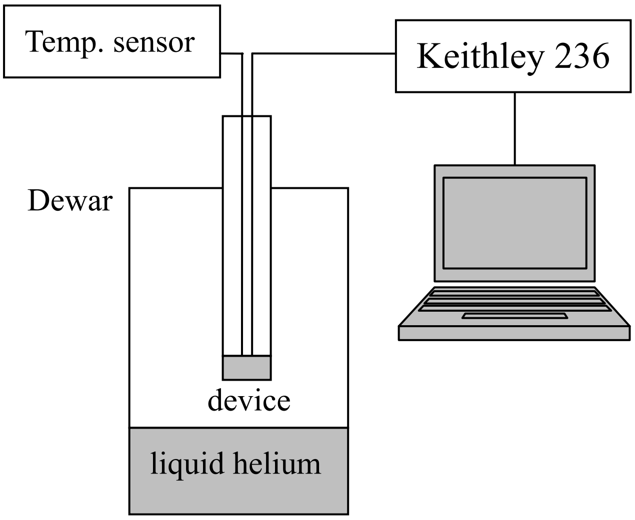

Figure 2.8: The setup of the dark current measurement system.

The second important characteristic is the responsivity spectrum. In our laboratory, the Fourier transform infrared spectroscopy (FTIR) is used to measure the photocurrent spectrum. Fig. 2.9 (a) shows the FTIR measurement system. The FTIR method is faster to get the spectrum than the monochromator method. The FTIR used in our lab is Nicholet 550 with computer control. The response photo signal is amplified by a low noise current amplifier (SR570) and feed back to the FTIR. Fig. 2.9 (b) shows the 45° waveguide measurement method. The incident light is polarized by a polarizer. The 0° polarized light included 50% TM and 50% TE mode light, and the 90° polarized is totally TE mode light. This method can measure the device photocurrent sensitivity under different polarization of radiation.

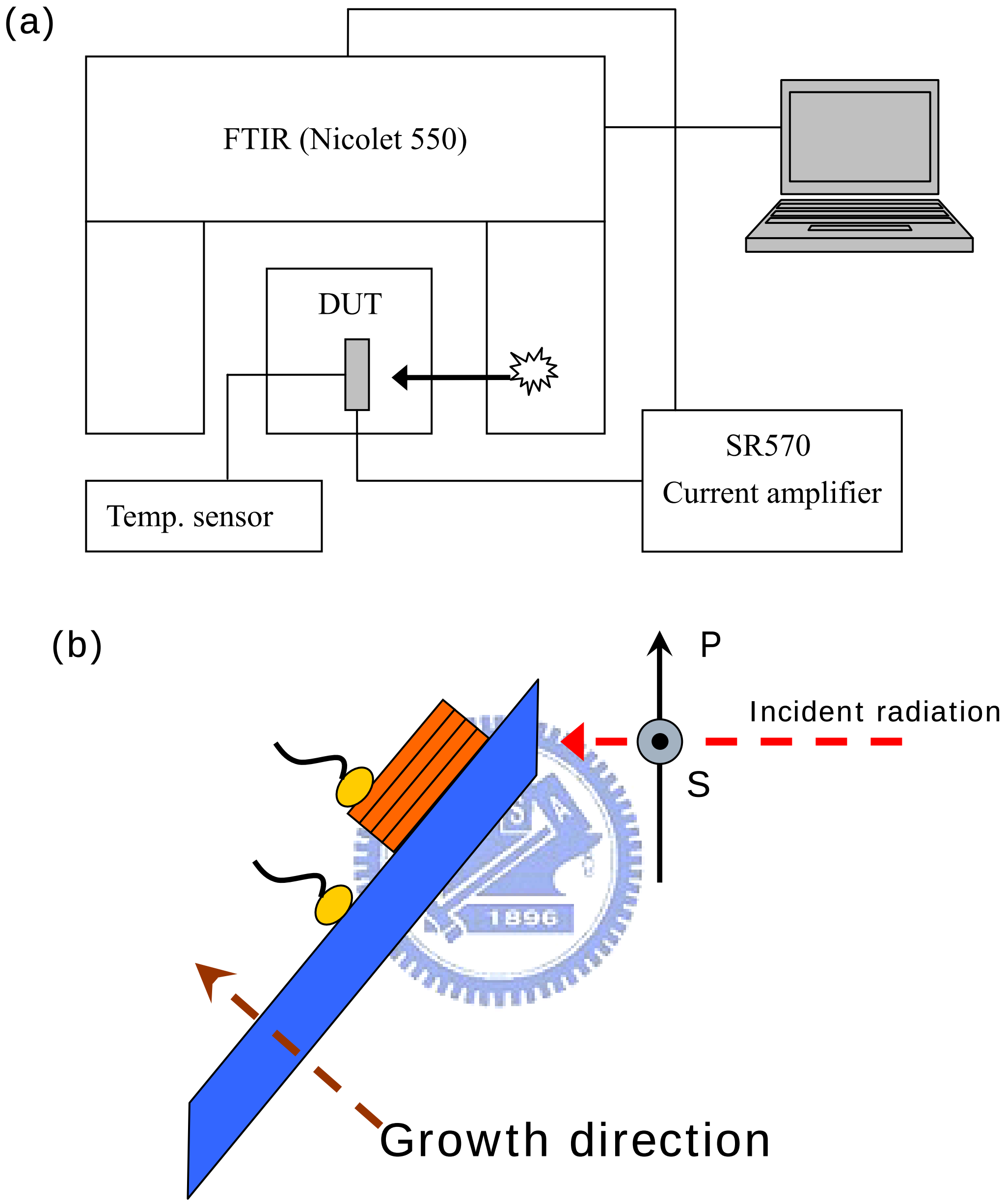

Figure 2.9: (a) The setup of the FTIR measurement system. (b) The 45° waveguide measurement method.

Because the light source of FTIR is not calibrated, we use a blackbody and lock-in amplifier to measure the photocurrent and calculate the absolute responsivity. The setup is showed in Fig. 2.10. In order to avoid the interband photocurrent, the germanium filter is used to filter out the high energy photon. Typically, the chopper frequency is set as 1000Hz in our measurement.

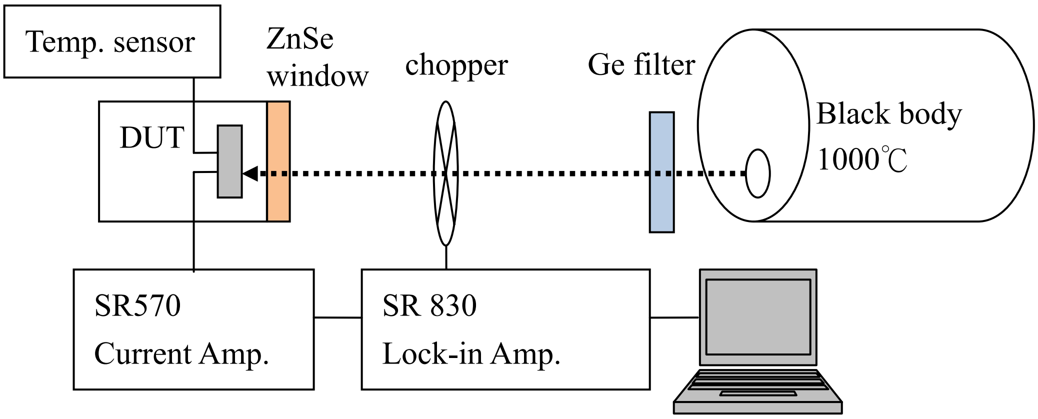

Figure 2.10: The responsivity measurement setup.

The peak responsivity (R_{peak}) can be calculated by the following equation:

$$R_{peak} = \frac{I_p}{A_D \cdot MF \cdot T_{Ge} \cdot T_{ZnSe} \cdot E \cdot \int R \cdot Q d\lambda} \tag{2.1}$$

where the I_p is the photocurrent, A_D is the device area. MF is the modulation factor of the chopper, and it is 0.38 in our system. T is the transmission coefficient of Ge filter and ZnSe window, and it is 0.64 and 0.7. R is the normalized response spectrum which is obtained by FTIR. Q is the blackbody radiation spectrum. E is the configuration factor given by:

$$E = \left(\frac{d}{2}\right)^2 \Big/ \left[D^2 + \left(\frac{d}{2}\right)^2\right] \tag{2.2}$$

where d is the aperture size of the blackbody radiation source and D is the distance between the light source and the device. The relation between applied bias and peak responsivity can be obtained.

The third important characteristic is the detectivity. The detectivity is the normalized signal to noise ratio. We use the SR770 fast Fourier transform (FFT) spectrum analyzer to measure the noise level. In order to reduce the noise which comes from the environment, we put the sample in the air phase of the liquid helium dewar flask and use the BNC cable for signal connection. Fig. 2.11 shows the measurement setup.

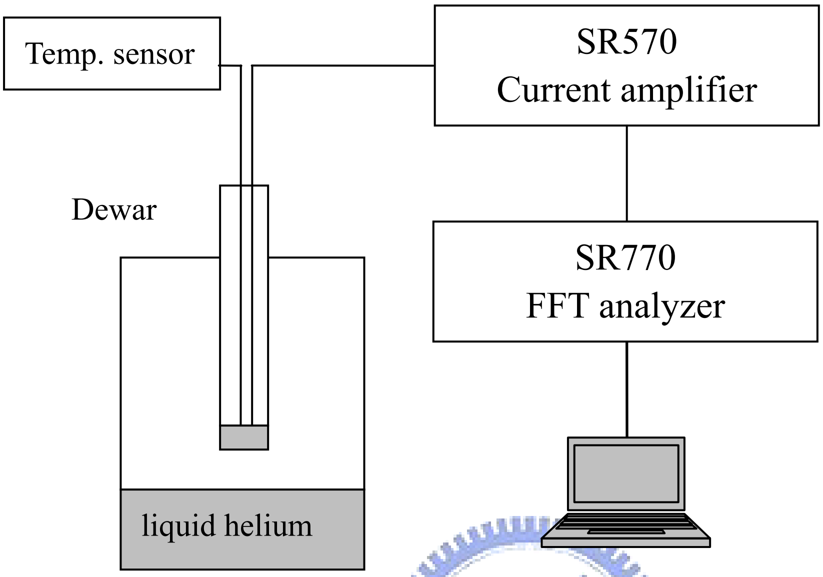

Figure 2.11: The noise measurement setup.

We measure the root mean square noise voltage of QDIP device. The noise current (I_n) can be calculated by the following equation.

$$V_n^2 = V_{n0}^2 + A^2 I_n^2 \tag{2.3}$$

where V_n is the measured noise voltage, V_{n0} is the noise under open circuit, and A is the gain of the SR570 current amplifier. After the noise current measurement, we can calculate the detectivity of the device. The detectivity (D^*) can be calculate by the following equation.

$$D^* = \frac{R\sqrt{A_D B}}{i_n} \tag{2.4}$$

where the R is the responsivity, A_D is the device area, the B is the bandwidth, and the i_n is the noise current.

Chapter 3

Fundamental of Quantum Dot Infrared Photodetectors

The quantum dot infrared photodetectors (QDIPs) structure consists of multi layer In(Ga)As/GaAs QDs as the active structure, which is sandwiched by two silicon n^+ doped contact layer. A high band gap $Al_xGa_{1-x}As$ current blocking layer is added in the active layer to reduce the dark current and enhance the performance. The detection mechanism is based on the carrier (electron) transition from lower energy level to higher energy level by absorbing a photon. The carrier at higher energy level is swept out by the external electric field and form the photocurrent. In this chapter, we will discuss the fundamental physics of the QDIPs, including the intersubband absorption (α), quantum efficiency (η), current gain (g), responsivity (R), dark current (I_d), noise current (i_n), and detectivity (D^*).

3.1 Absorption of Intersubband Transition

The absorption coefficient (α) is defined as incident photo energy ($\hbar\omega$) times the number of transitions per unit volume per unit time divided by the incident power per unit area. The absorption coefficient of a given transition from initial state (i) to final state (f) can be expressed as:

$$\alpha(\omega) = \frac{\pi\hbar N_d n e^2}{m^* \varepsilon c}\left[\frac{\Gamma}{\left(\hbar\omega - \hbar\omega_{if}\right)^2 + \Gamma^2}\right]\cdot\left(n_i - n_f\right)\cdot f_{if} \qquad (3.1)$$

where $\hbar$ is the Plank constant, N_d is the number of dot per unit volume, n is the refractive index, ε is the permeability, n_i and n_f are the occupation probability in initial and final state, Γ is the life time broadening, and f_{if} is the oscillator strength. The oscillator strength is a dimensionless quantity to express the transition probability from initial state (i) to final state (f). The oscillator strength could be expressed as:

$$f_{if} = \frac{2m^*}{\hbar^2} \cdot \left(E_f - E_i\right) \cdot \left|\langle i|r|f\rangle\right|^2 \tag{3.2}$$

3.2 Quantum Efficiency

The quantum efficiency (η) is the photo carrier generation probability. The photo carrier generation process consists of the carrier transition from lower energy level to higher energy level and the excited carrier escape from quantum dot bound state to continuous state. Thus, the quantum efficiency could be expressed as:

$$\eta = \eta_\alpha \cdot p_e \tag{3.3}$$

where the η_α is the absorption quantum efficiency, and p_e is the escape probability. The absorption quantum efficiency (η_α) can be given as:

$$\eta_\alpha = (1 - r)\left(1 - e^{-2\alpha L}\right)\chi \tag{3.4}$$

where r is the reflection coefficient, α is the absorption coefficient, L is the height of the QD, and χ is the polarization correction factor.

The escape probability is the function of applied external electric field. The escape probability can be expressed as:

$$p_e = \left(1 + \frac{\tau_e}{\tau_c}\right)^{-1} \tag{3.5}$$

where the τ_e is the time which is required to escape from the origin quantum dot, and τ_c is the excited carrier recapture time. The τ_e is a function of the electric field and τ_c is independent from the electric field.

3.3 Current Gain

The current gain (g) is defined as:

$$g \equiv \tau_{life} / \tau_t \tag{3.6}$$

where τ_{life} is the life time of the photo carrier, and τ_t is the transit time of the photo carrier across the active region. The current gain can also be expressed as:

$$g = \frac{1 - \frac{1}{2} p_c}{NFp_c} \tag{3.7}$$

where the p_c is the capture probability when the carrier pass through the QDs, N is the QDs layer number of the device, F is the filling factor of QDs in one layer. The capture probability is determined by device structure, material parameter, and energy distribution of electrons.

3.4 Responsivity

The photocurrent (I_p) of the QDIPs device can be expressed as:

$$I_p = A_D q \Phi \eta g \tag{3.8}$$

where A_D is the device area, q is the charge of electron, Φ is the radiation flux, η is the quantum efficiency, and g is the current gain. The reponsivity is defined as the photo current under unit radiation power. Thus the responsivity can be given as:

$$R = \frac{I_p}{A_D \Phi \hbar\omega} = \frac{q}{\hbar\omega} \eta g = \frac{\lambda(\mu m)}{1.24} \eta g \tag{3.9}$$

3.5 Dark Current

The dark current of the QDIPs could be divided into three parts:

1. Thermionic emission: the leakage current caused by the carriers which are thermally excited into continuous state and form the current by the external electric field.
2. Thermally assisted tunneling: the leakage current caused by the carriers which are thermally excited into higher energy level and tunnel through the triangular barrier.
3. Temperature independent tunneling: the leakage current caused by the carriers in ground state tunnel into the neighbor QDs state level or into the continuous level.

The dark current density can be expressed as:

$$j_D = qv_d n \tag{3.10}$$

where n is the free carrier density, and v_d is the carrier drift velocity.

3.6 Noise

There are two major noise source of a photodetector under operation. One is the dark noise and the other is the 300K background radiation noise. The dark noise includes thermal noise (Johnson noise), flick noise (*1/f* noise), and generation-recombination noise (G-R noise). The thermal noise current (i_{th}) is the electronic noise generated by the thermal agitation of the electrons, and can be expressed as:

$$i_{th} = \sqrt{\frac{4kTB}{R_{res}}} \tag{3.11}$$

where R_{res} is the differential resistance of the device, and the B is the measurement bandwidth.

The flick noise is a type of electronic noise of low-frequency phenomenon. The flicker noise current ($i_{1/f}$) can be expressed as:

$$i_{1/f} = \sqrt{\frac{KI^2B}{f}} \tag{3.12}$$

where K is a proportionality factor, and I is the bias current.

The G-R noise is a type of electrical signal noise caused by the fluctuation of the generation and recombination of electrons in semiconductor-based photon detectors. The G-R noise current ($i_{G\text{-}R}$) can be expressed as:

$$i_{G-R} = 2I\sqrt{\frac{\tau B}{N_0\left(1+\omega^2\tau^2\right)}} \tag{3.13}$$

where τ is the lifetime of free carriers, and N_0 is the total number of the free carriers of the device. In QDIPs, the free carrier (N_0) is given as:

$$N_0 = \frac{I \cdot \tau_t}{q} \tag{3.14}$$

where the τ_t is the transit time when the carrier across the device. Thus, the G-R noise can be express as:

$$i_{G-R} = \sqrt{4qIg \cdot \frac{B}{1+\omega^2\tau^2}} \quad , \quad g \equiv \frac{\tau}{\tau_d} \tag{3.15}$$

where g is the noise current gain. In most case, the $\omega\tau << 1$, thus the G-R noise can be rewritten into:

$$i_{G-R} = \sqrt{4qIgB} \tag{3.16}$$

As a good approximation, the photoconductive gain and the noise gain are equal in a conventional photoconductor and can be expressed as [38]:

$$g = \frac{i_{G-R}^2}{4qI} \tag{3.17}$$

The thermal noise is significant in very low bias region, and the flicker noise is low frequency phenomenon. Therefore, the noise current of QDIPs is primary G-R noise.

Because the G-R noise is the dominated noise of the QDIPs, the background radiation noise can be written as:

$$i_{nb} = \sqrt{4qI_b gB} \quad , \qquad I_b = R \cdot P_b = \left(\frac{q}{\hbar\omega}\eta g\right) \cdot P_b \tag{3.18}$$

where P_b is the incident background optical power and can be expressed as:

$$P_b = A_D \sin^2\left(\frac{\Omega}{2}\right)\int_{\lambda_1}^{\lambda_2} Q(\lambda)d\lambda \tag{3.19}$$

where Ω is the field of view, Q is the blackbody radiation power distribution. The integration range is the spectral range of the detector. Therefore, the overall noise is the combination of the dark noise and background noise:

$$i_n = \sqrt{i_{nd}^2 + i_{nb}^2} = \sqrt{4qgB \cdot \left[I_d + qg \cdot \left(\frac{\eta P_b}{\hbar\omega}\right)\right]} \tag{3.20}$$

3.7 Detectivity

For a photodetector, the detectivity (D^*, D-star) is used to characterize the device performance. The detectivity equals to the reciprocal of noise equivalent power (*NEP*), normalized to unit area and unit bandwidth.

$$D^* = \frac{(A_D B)^{1/2}}{NEP} \tag{3.21}$$

The *NEP* is the incident radiant power which gives rise to signal current equal to the noise current. The detectivity of QDIPs can be given as:

$$D^* = \frac{R\sqrt{A_D B}}{i_n} \tag{3.22}$$

where R is the responsivity, and the i_n is the noise current of the QDIPs.

In real application, the device must be operated under background photon noise limitation that is background limited performance condition (BLIP) which the dark current is low enough so the noise is dominated by the background noise.

$$D^*_{BLIP} = \frac{R\sqrt{A_D B}}{i_{nb}} = \frac{\frac{q}{\hbar\omega}\cdot\eta\cdot g\cdot\sqrt{A_D B}}{\sqrt{4q^2 g^2 B\cdot\left(\frac{\eta P_b}{\hbar\omega}\right)}} = \frac{1}{2}\left(\frac{\eta A_D}{\hbar\omega P_b}\right)^{1/2} \tag{3.23}$$

The detectivity under the BLIP condition is the only function of the quantum efficiency (η), and is dependent of the dark current (I_d) and gain (g).

Chapter 4

Temperature Dependent Responsivity of Quantum Dot Infrared Photodetectors

Temperature dependent behavior of the responsivity of InAs/GaAs quantum dot infrared photodetectors was investigated with detailed measurement of the current gain. The current gain varied about two orders of magnitude with 100K temperature change. The dramatic change of the current gain is explained by the repulsive coulomb potential of the extra carriers in the QDs. With the measured current gain, the extra carrier number in QDs was calculated. More than one electron per QD could be captured as the dark current increases at 150K. The extra electrons in the QDs elevated the Fermi level and changed the quantum efficiency of the QDIPs. The temperature dependence of the responsivity was qualitatively explained with the extra electrons.

4.1 Introduction

The responsivity of QDIPs shows a very different behavior compared to that of QWIPs. In QWIPs, the responsivity keeps almost constant at different device temperatures and changes linearly with the bias voltage for bound-to-continuum (B-C) type device. On the contrary, in QDIPs, the responsivity increases dramatically with both voltage and temperature. The stability of the responsivity of QWIPs with either temperature or voltage is crucial to provide a wide operation range in practical applications. However, only few researches have been done on this issue. Detailed analysis on the quantum efficiency considering the temperature dependent of the escape rate, the ground state population and excited carrier life time has been published [39]. The calculated quantum efficiency showed a small change within a factor of 2 from 0 K to 150 K under a fixed voltage. It is much smaller than the measured responsivity change which varies by a factor of 10 within 100K. Thus, other factors must be considered to explain the temperature dependence of the responsivity of QDIPs. Although it is observed that the current gain varies with the temperature, no detailed study was executed with the experimental data. In this study, a detailed analysis of the responsivity was done based on the current gain measurement to explain the temperature dependence of the responsivity in QDIPs.

4.2 Basic characteristics of the sample

The sample (Rn0218) was grown by Veeco Gen-II MBE system on (001) GaAs semi-insulating substrate. Ten periods of InAs/GaAs QDs with 50nm barriers were used in the active region. Each barrier consisted of 47nm GaAs layer and 3nm $Al_{0.2}Ga_{0.8}As$ current blocking layer. Fig. 4.1 shows the device structure and the band diagram of the active region. Fig. 4.2 shows the TEM image of the active layer QDs, and the image shows the 3nm $Al_{0.2}Ga_{0.8}As$ current blocking layer was partially cover the QDs. The detail function of the current blocking layer was explained in Ref. 23. The active region was sandwiched by 500nm n-type contact layers. Delta-doped Si layer was inserted 2nm before each QD layer to provide electrons in each QD. By the examination of surface AFM, the QD density is about 2.4×10^{10} cm^{-2} and the size is about 8nm in height and 25nm in radius. The device processing and measurement system have been described in chapter 2.

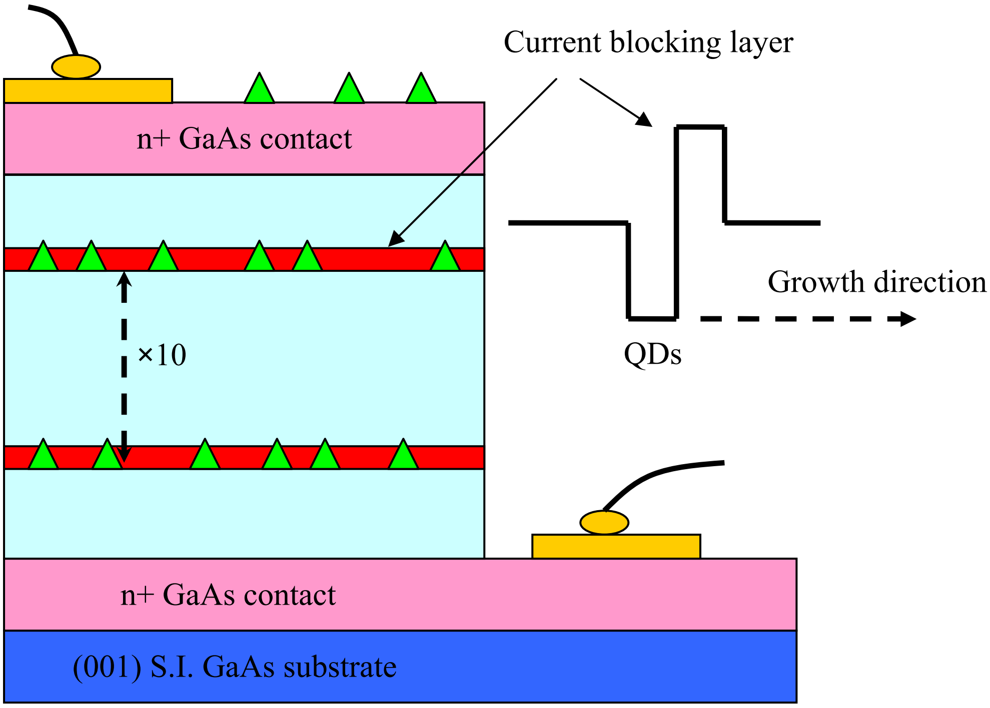

Figure 4.1: The schematic drawing of the device structure used in this study. Inset shows the band diagram of the QDs in the active region.

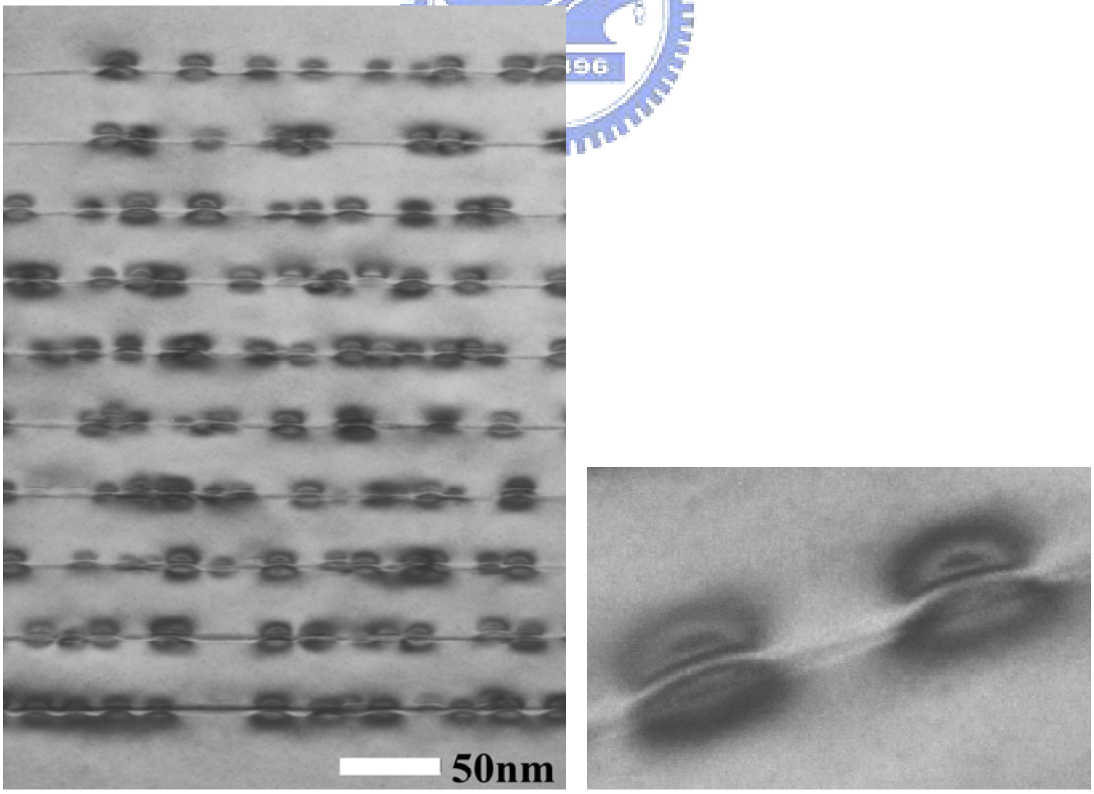

Figure 4.2: The TEM image of the ten InAs/GaAs QDs layers with 50nm spacer. Each spacer includes 47nm GaAs and 3nm $Al_{0.2}Ga_{0.8}As$.

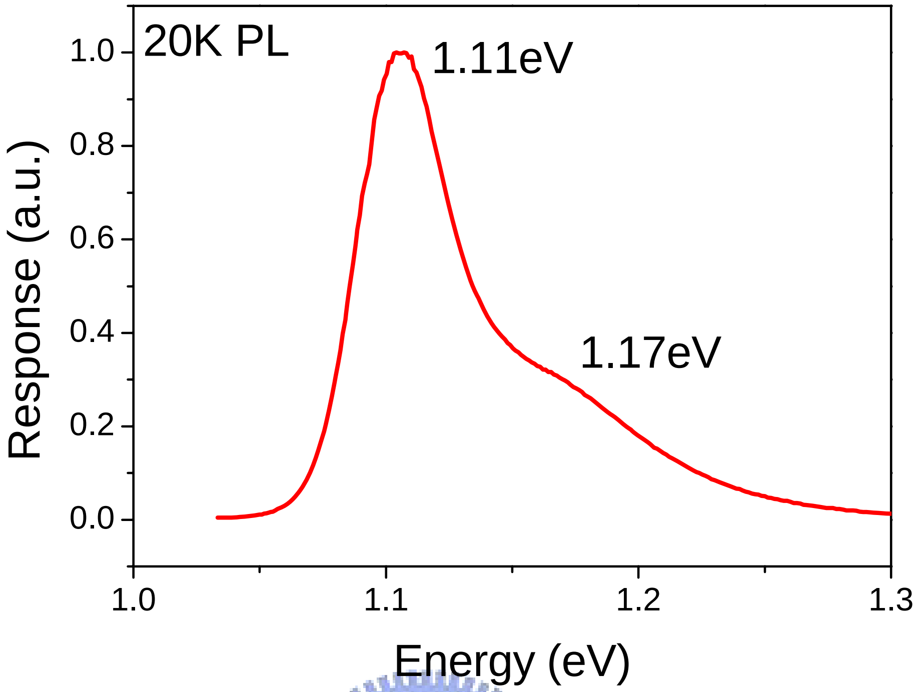

Figure 4.3: The low temperature PL result of the sample. The transition peaks are at 1.11 and 1.17eV. The ground state FWHM is around 50meV.

Fig. 4.3 shows the low temperature (20K) PL result of the sample. The ground state energy was at 1.11eV with a FWHM around 50meV. Comparing the infrared responsivity peak (6μm, ~205meV) with the transition peaks, the transition could be deduced to be from the ground state to the bound excited state associated with the 1.39eV transition level assuming a 70% energy discontinuity in the conduction band.

Fig. 4.4 shows the dark current activation energy at different voltages. The dark current density is less than 1×10^{-5} A/cm^2 at 77 K and 0.3 V. The activation energy of the dark current is about 140meV at low bias and decreases linearly with the increase of bias. The decrease of the activation energy has been investigated to be from the tunneling process between the QD layers [40]. The low activation energy implies the impact ionization could happen at the high voltage region. Assuming a uniform electric field distribution across the device, the kinetic energy of the emitted carriers is higher than the activation energy when bias is larger than 0.9V or -0.75V. The multiplication process generates extra noise to the usual G–R noise and deteriorates the performance. In order to get the correct gain value, we limited the bias range between 0.9 V and -0.75 V in the following discussions. The photo-response of the devices were measured at different temperatures by a FTIR spectrometer, and calibrated by a 1000℃ blackbody source under normal incident illumination. The detectivity of this device is 1×10^{10} cmHz$^{1/2}$/W and responsivity is 0.2 A/W at 0.5V at 77K. Fig. 4.5 shows the responsivity of the sample at different temperatures and biases. As mentioned, the responsivity increases exponentially with bias. As the temperature rose, the responsivity also increased dramatically from 40 K to 100 K and saturated after 100 K. Such dependence is quite different from what has been observed in QWIPs.

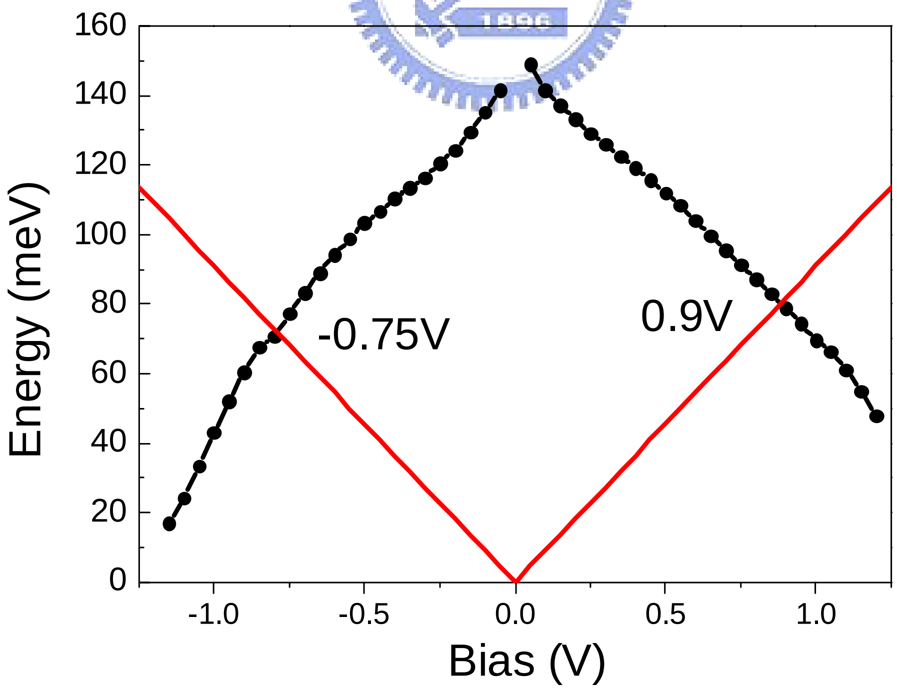

Figure 4.4: The scatter line shows the dark current activation energy at different voltages. The straight line shows the kinetic energy of electrons across one barrier under uniform electric field.

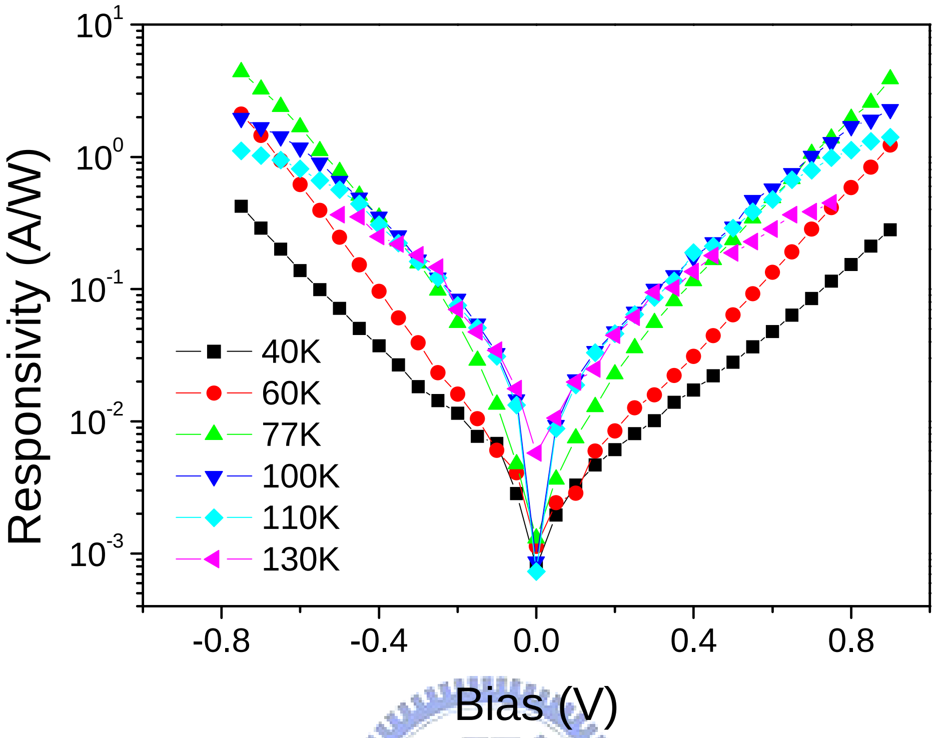

Figure 4.5: The responsivity versus bias at different temperatures.

4.3 Results and discussion

In order to investigate the temperature dependent of the responsivity, we measured the current gain and separated the quantum efficiency from the responsivity. The noise current of the device was measured at different temperatures and biases. The noise spectrum at 130 K is shown in Fig. 4.6. Similar to QWIPs, the noise spectrum showed a white noise feature and is dominated by the carrier generation and recombination process, i.e., G–R noise in QDIPs [38]. The relation between the G–R noise current and the current gain g is:

$$g = \frac{I_n^2}{4qI_d} \tag{4.1}$$

where I_d is the dark current, q is electron charge, and I_n is the noise current.

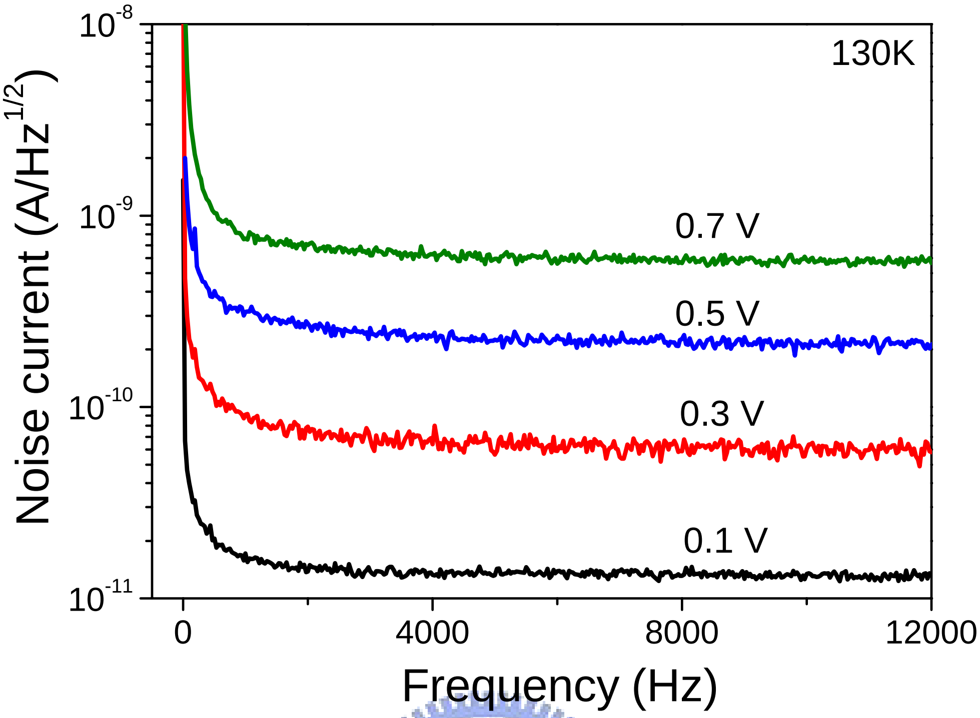

Figure 4.6: The noise spectrum at 130K and different bias voltages.

The current gain was calculated and plotted in Fig. 4.7. Due to the limit of the measurement system, noise current smaller than 1×10^{-13} A/Hz$^{1/2}$ cannot be correctly measured. Thus, the current gain at lower biases with lower temperatures is not available. Obviously, the current gain has a similar trend as the responsivity does. The current gain increases more than 50 times from 70 K to 140 K.

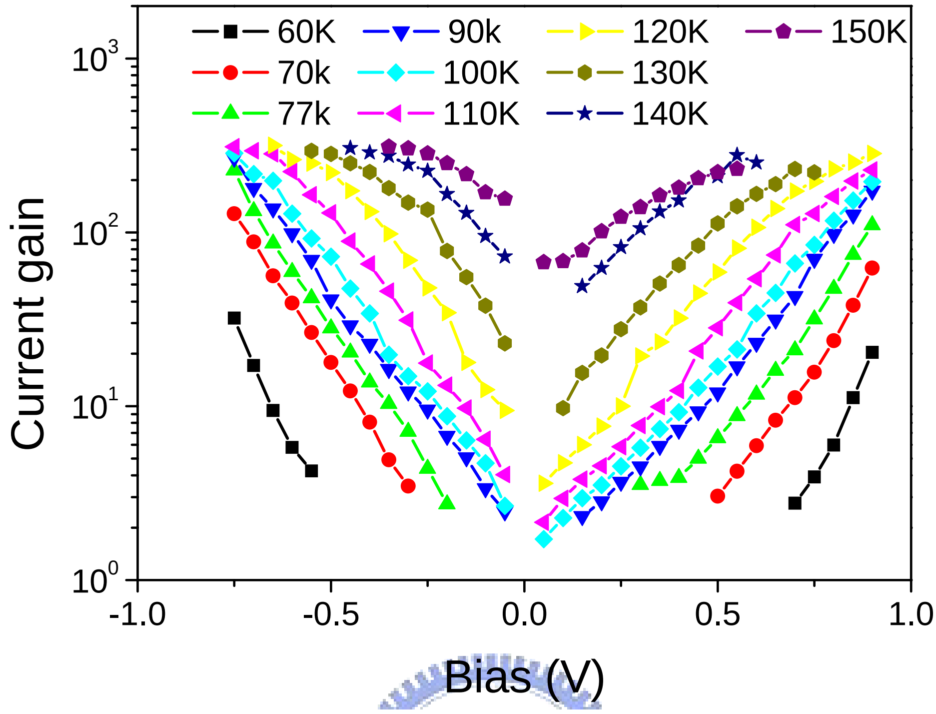

Figure 4.7: The current gain of the sample at different bias and temperatures.

The carrier capture probability through the QD layer changed dramatically within the temperature range. One major difference is that the gain increases without saturation even at 150 K. This shows the change of responsivity is dominated by the current gain thus the capture probability. The capture probability P_c can be calculated with the current gain g and equation 3.7.

Fig. 4.8 shows the capture probability at different temperatures and biases. With the increase in bias, the capture probability decreases rapidly, which results in a rapid increase in the current gain.

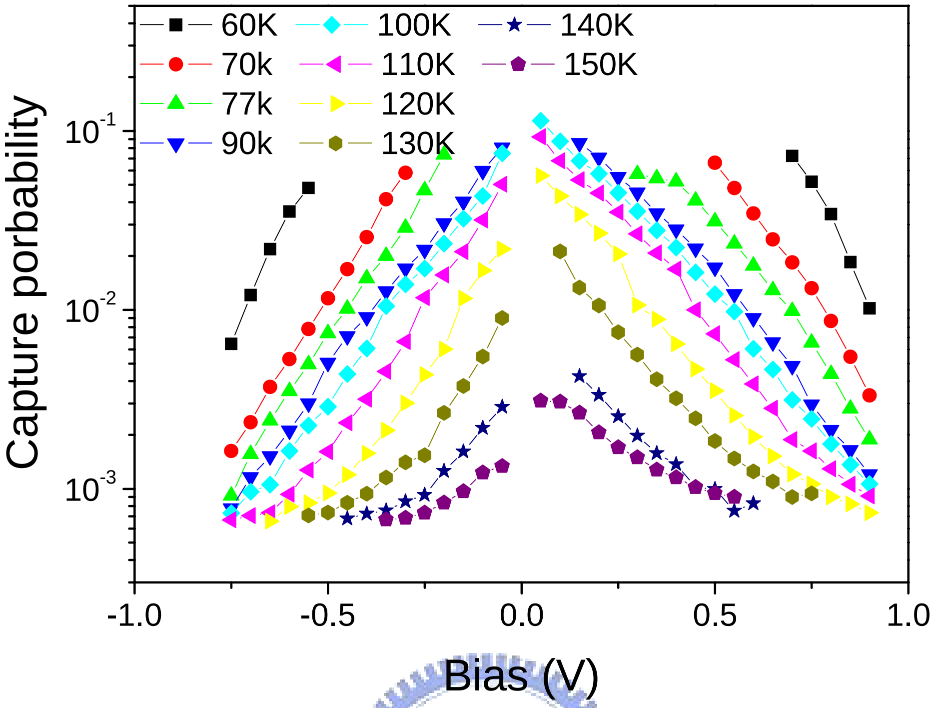

Figure 4.8: The capture probability at different bias and temperatures.

The capture process is influenced by the repulsive coulomb potential of the extra carriers inside the QDs. Unlike in the QWs, where carriers flow freely in the *x–y* direction, the isolated charge in the quantum dot could generate potential barrier to electrons passing through the QD layers. That is why such dependence was never observed in typical QWIPs. In principle, the repulsive potential is related to the capacitance of the QD and the charge number inside the QD. The capture probability P_c of the carriers passing through the QDs could be approximated with the following equation [41]:

$$P_c = P_0 \frac{N_{QD} - \langle N \rangle}{N_{QD}} \exp\left(-\frac{e^2 \langle N \rangle}{C k_B T}\right) \qquad \text{with} \qquad C = 2\varepsilon * a_{QD} \big/ \pi\sqrt{\pi} \qquad (4.2)$$

where P_0 is the capture probability under neutral condition, N_{QD} is the maximum electron number that a QD can accommodate, $<N>$ is the average extra carrier number in the QDs. *C* is the capacitance of the QD and a_{QD} is area of the QD. The number of electrons inside the QD is determined by the balance of the trapped current into the QDs with the emitted current from the QDs. When the current increases with temperature and bias, the carrier number inside the QD increases. As a result, the capture probability decreases and the current gain show a dramatic increase with temperature and bias. To further verify the idea, two QDIPs with identical device structure but different QD doping density were compared.

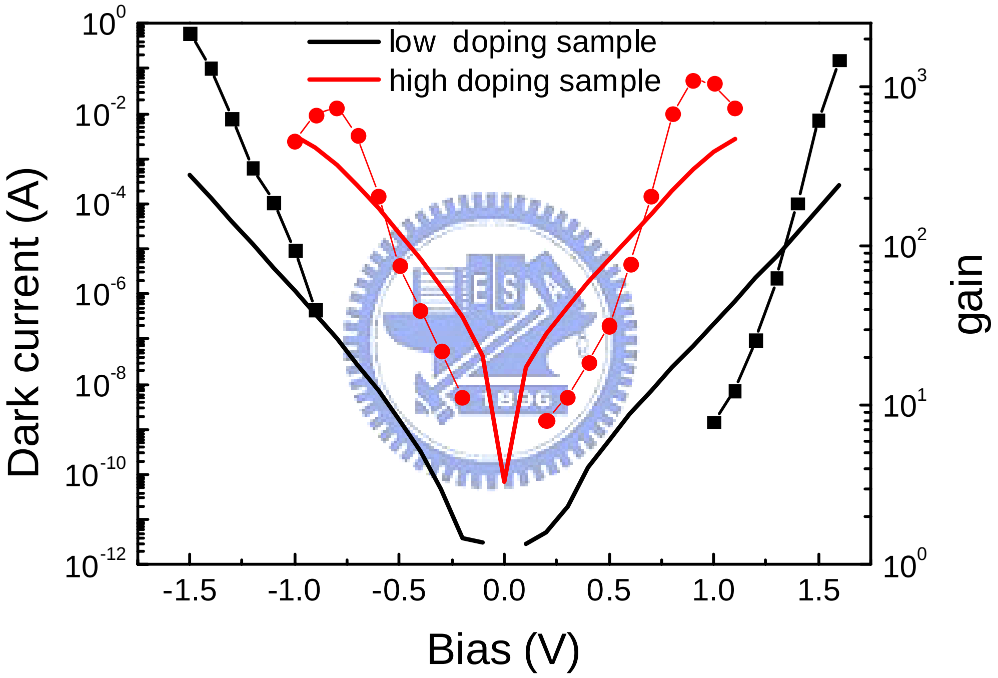

Figure 4.9: The dark current (solid curve) and current gain (scatter curve) curve for the two samples with different doping concentration at 77K.

Fig. 4.9 shows the dark current and the current gain of the two samples at 77 K. The low doping sample showed a much lower dark current as expected. Also, the current gain of the low doping sample is much lower than that of the high doping sample. This phenomenon cannot be explained without the carrier filling process since the identical device structure should give similar transport property and the current gain value should be similar for the two samples. With such a concept, the average excess carrier number can be estimated with the carrier capture probability and the device parameters. Due to the large size of our QDs, N_{QD} is much large than $<N>$ and $(N_{QD} - <N>)/N_{QD}$ is approximated to 1. The neutral capture probability P_0 is equal to the ratio of transit time (τ_{td}) and the capture time of the QD (τ_c). The transit time can be calculated with the drift velocity:

$$\tau_{td} = \frac{h}{v_d} = \frac{h}{\mu F \Big/ \left[1 + \left(\mu F / v_{sat}\right)^2\right]^{0.5}} \tag{4.3}$$

where μ is the carrier mobility, v_{sat} is the saturation velocity and h is the height of the QDs. In our calculation, the mobility value of 2000 cm^2/V-s and the saturation velocity of 1×10^6 cm/s were used. The capture time has been reported to be in the order of pico-second by different experiments [42, 43]. Here 5ps is used in our calculation. All of the parameters in our calculation were listed in table 4.1. Fig. 4.10 shows the estimated average extra carrier number.

parameters	value	unit
dot density	2.4×10^{10}	#/cm^2
dot diameter	50	nm
filling factor	49%	
dot height (h)	8	nm
carrier mobility (μ)	2000	cm/V-s
saturation velocity (v_{sat})	1×10^6	cm/s
layer number	10	
capture time (τ_c)	5	pico-second

Table 4.1: The parameters used in calculation of average excess carrier in QDs.

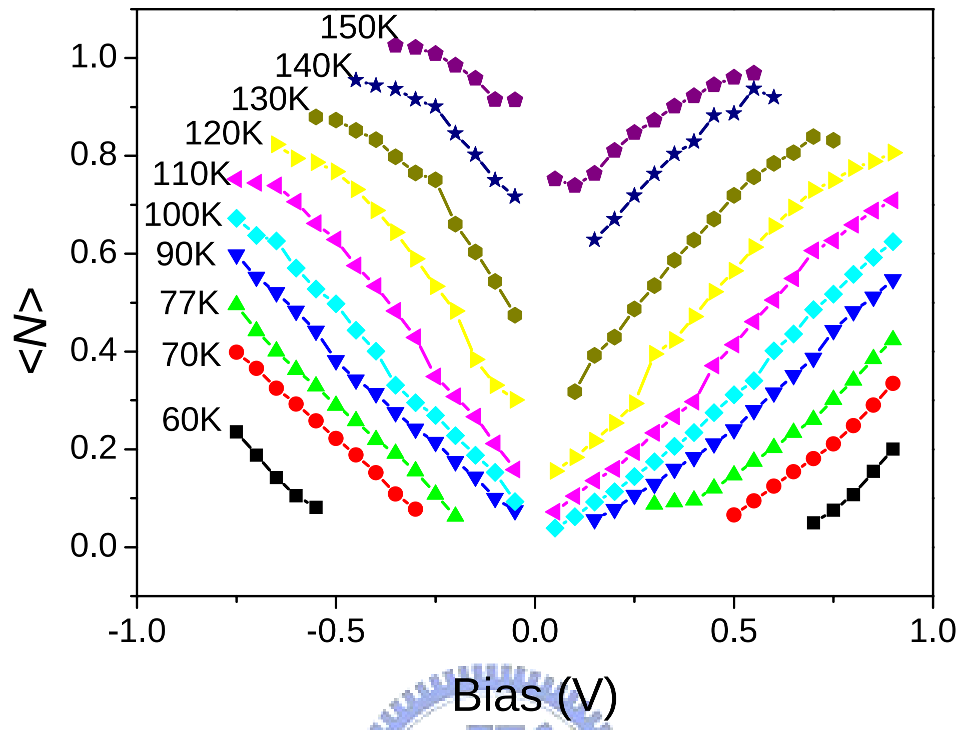

Figure 4.10: The calculated average extra carrier number <*N*> in one QD at different temperature and voltages.

When the temperature and bias is low, almost no extra carriers exist inside the QDs. When the device current increases with either temperature or voltage, <*N*> could be more than 1 electron at 150 K. Due to the higher dark current at negative biases, the extra carrier number is higher under negative biases. Although the dark current increases exponentially with temperature, the average charge in one QD increases only linearly with temperature and bias. According to the theoretical calculation for the lens shape quantum dot, the energy difference between the ground state and the first excited state energy is around 50meV for our InAs QDs [44]. Considering the size distribution of the QDs, the density of states of the ground state and the first excited state of the QD layer could overlap and form a band. When the average carrier number increases linearly, the Fermi level of the QD layer also increases in a linear way. The emitted current is thus increases exponentially to balance the captured carriers. In order to check the reality of the calculated <N>, we tried to compare the result with the device quantum efficiency. It is well understood that the carrier number inside the QD is essential to the quantum efficiency and the performance of QDIPs. The optimized condition occurs when the ground states are fully occupied and the excited states are all empty, i.e., 2 electrons per QD. Using the measured current gain, the quantum efficiency is calculated with the responsivity and gain shown in Fig. 4.11.

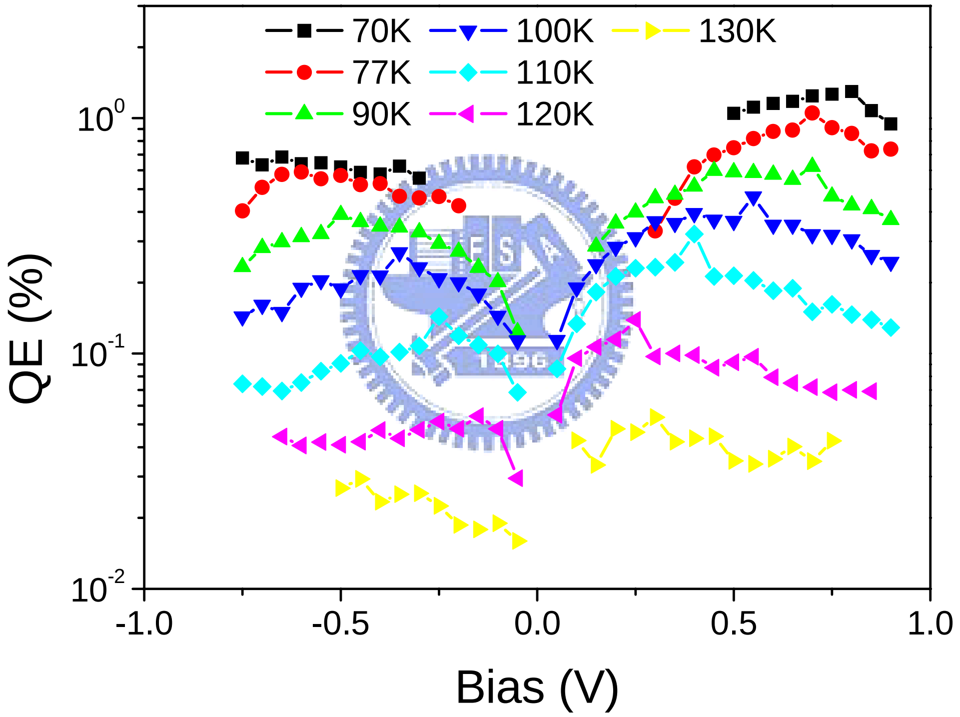

Figure 4.11: The quantum efficiency of the sample at different bias and temperature.

Due to the increase of the escape probability of the B–B type transition, the quantum efficiency increases exponentially at low bias region in all temperature. However, the peak quantum efficiency decreases by a factor of 10 with the increase of temperature from 70 K to 130 K. Such difference cannot be attributed to the thermal distribution of the carriers inside the QDs which could only change for 10% in our temperature range [36]. Since the doping density of our sample is less than 2e$^-$/QD, as the extra carrier number increases, the quantum efficiency increases and then start to drop slowly. As the temperature goes higher, <*N*> increases and the maximum of the quantum efficiency occurs at lower voltage. If we compare <*N*> with the quantum efficiency carefully as shown in Fig. 4.12, the peak quantum efficiency happened when the excess carrier number is around 0.4 independent of the temperature.

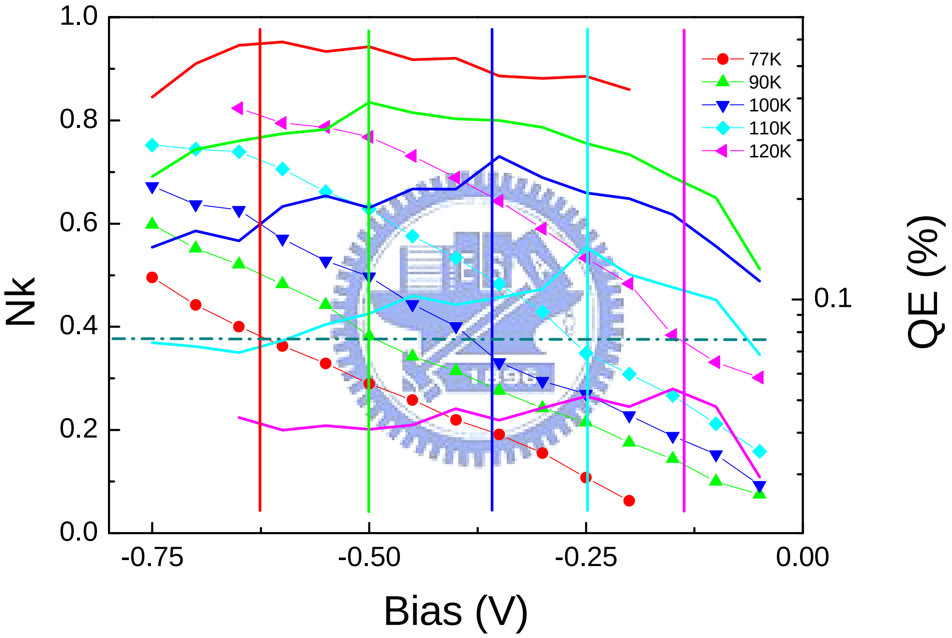

Figure 4.12: The quantum efficiency (solid curve) and <*N*> (scatter line) at different temperatures and negative voltages. The vertical lines are used to indicate the voltage of quantum efficiency peaks. The peak quantum efficiency occurs around <*N*>=0.4.

Of course, other factors such as the excited carrier life time might also induce the lower quantum efficiency at high temperature. From the discussion above, we know the change of carrier number inside the QDs plays an important role on the temperature dependence of the responsivity in QDIPs. The higher the dark current is, the more charge inside the QDs will be. This feature enhances the responsivity and the performance of the QDIPs at higher temperature. The photocurrent can be kept at a higher level with elevated temperature though the quantum efficiency decreases. Taking the extra charge into account, it is beneficial to use smaller QDs to have a more stable responsivity. The small QDs associated with smaller capacitance could generate higher potential barrier to suppress the carrier injection into the QDs. QDIPs with smaller QDs could provide higher current gain and stable quantum efficiency.

4.4 Summary

The temperature dependence of responsivity of InAs/GaAs QDIPs has been investigated. From the measurement, we found the dramatic change of the current gain with temperature dominates the behavior of the responsivity. The increasing dark current with the temperature injects more carriers inside the QDs. The repulsive potential of the extra carriers suppress the capture process and enhance the current gain. The average extras carrier number calculated from the capture probability qualitatively explained the behavior of the quantum efficiency. From this concept, QDIPs with smaller QD and higher density is predicted to have better temperature stability and also maintain a higher current gain.

Chapter 5

Vertically Coupled Quantum Dot Infrared Photodetectors

Vertically coupled InAs/GaAs quantum dot infrared photodetectors (QDIPs) were studied. With vertically coupled quantum dots, the formation of the mini-bands among quantum dot (QD) layers enhances the uniformity of QD states and results in a narrow response band and higher peak quantum efficiency. The mini-bands increase the capture probability and also facilitate the carrier flow among QD layers and leads to more uniform carrier distribution. Because these, the frequency response of vertically coupled quantum dot infrared photodetectors were much faster than that of the conventional ones.

5.1 Introduction

The performance of QDIPs is limited by the low quantum efficiency which is critical to the performance under normal operations. The density and uniformity of the quantum dots are essential for the improvement of the quantum efficiency. Unfortunately, the density and uniformity of QDs are greatly limited by the self assembled growth process of QDs. In addition to quantum efficiency, poor frequency response of the responsivity in QDIPs was also reported with the roll-off frequency lower than 1K Hz especially at lower temperatures [45]. Compared with QWIPs, the roll-off frequency is a few orders of magnitude lower for QDIPs. The long RC time constant originated from the charging process of the electrons into the quantum dots deteriorates the frequency response [46, 47]. This limits the use of QDIPs in some military and space applications where the high speed detection is needed.

With thin spacer layers between QD layers, it has been demonstrated that the vertically coupled quantum dots can be grown and generated mini-bands among the QD layers. In the vertically coupled QD columns, the energy levels form mini-bands and allow carriers to diffuse to different QD layers easily [48, 49]. In the past, the infrared absorption of vertically coupled QDs has been reported but without any real device characteristics [50]. In this study, the vertically coupled QDs were used as the active layer in the QDIPs to solve the issues mentioned above. Higher quantum efficiency, narrower response spectra, and higher roll-off frequencies than the conventional QDIPs were demonstrated.

5.2 Vertically coupled QDs characteristics

The vertically coupled multilayer self-assembly InAs/GaAs QDs shows the different photoluminescence results than the single layer QD sample such as the PL signal red-shift and narrower linewidth. Two samples with the similar QD growth condition were used in this study (Lm4454 & Lm4469). One is single layer sample and the other is ten layer vertically aligned sample with 10nm dot to dot spacer. The local strain relaxation facilitates the QDs formed directly on the top of the lower layer QDs [48]. The partial strain relaxation is expected to be removed as the GaAs capping layer thickness increasing. When only few GaAs is capped on the QDs, the strain field from the buried QDs would extend to the surface. The 10nm GaAs capping layer was thin enough to make sure the QDs were well aligned in growth direction.

Fig. 5.1 shows the low temperature (20K) PL result of these two samples. The peak energy of single and multilayer sample is 1.26eV and 1.22eV, and the linewidth is 72meV and 48meV. The peak energy shows 40meV red shift and the linewidth shows 24meV reduction. The carriers would diffuse to the lowest energy state of QDs in the same column by tunneling through the 10nm GaAs barrier. As a result, the PL spectrum peak shifts to lower energy. The size variation of QDs causes the ground state energy variation, and contributes to the PL spectrum linewidth. Because the carrier will diffuse to the lowest energy level, the linewidth of the multi-layer sample is contributed from the lowest energy level of the QD column. Therefore, the linewidth of vertically coupled QDs sample is narrower than single layer sample.

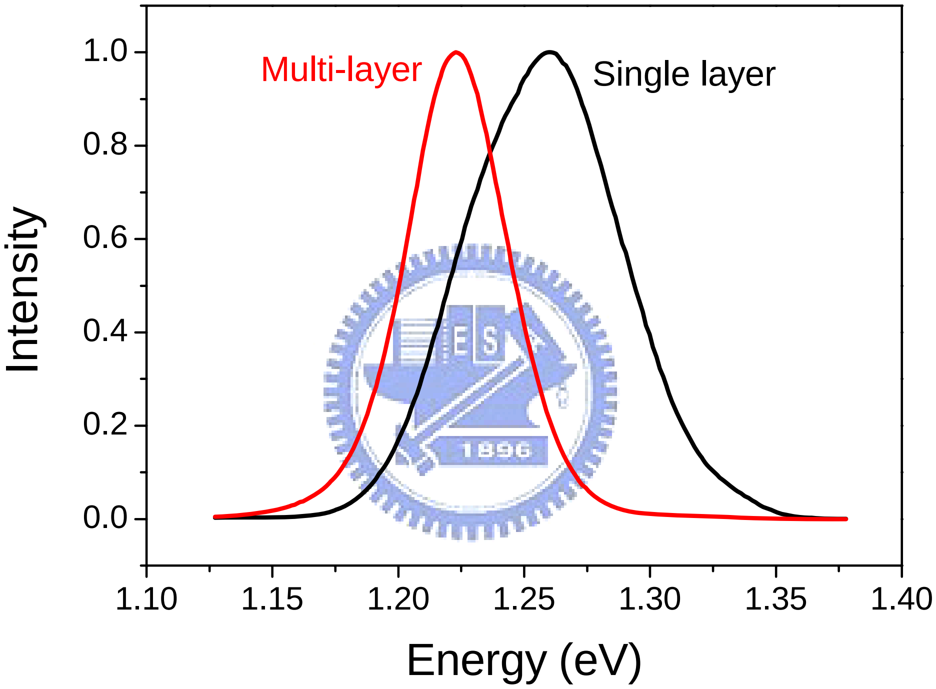

Figure 5.1: The low temperature (20K) PL result of single layer and multi-layer quantum dot samples.

In addition to the peak red shift and the narrower linewidth, the temperature dependent behavior of the vertically coupled QDs is also different from that of single layer QDs. Fig. 5.2 (a) (b) shows the PL spectra at different temperature of these two samples.

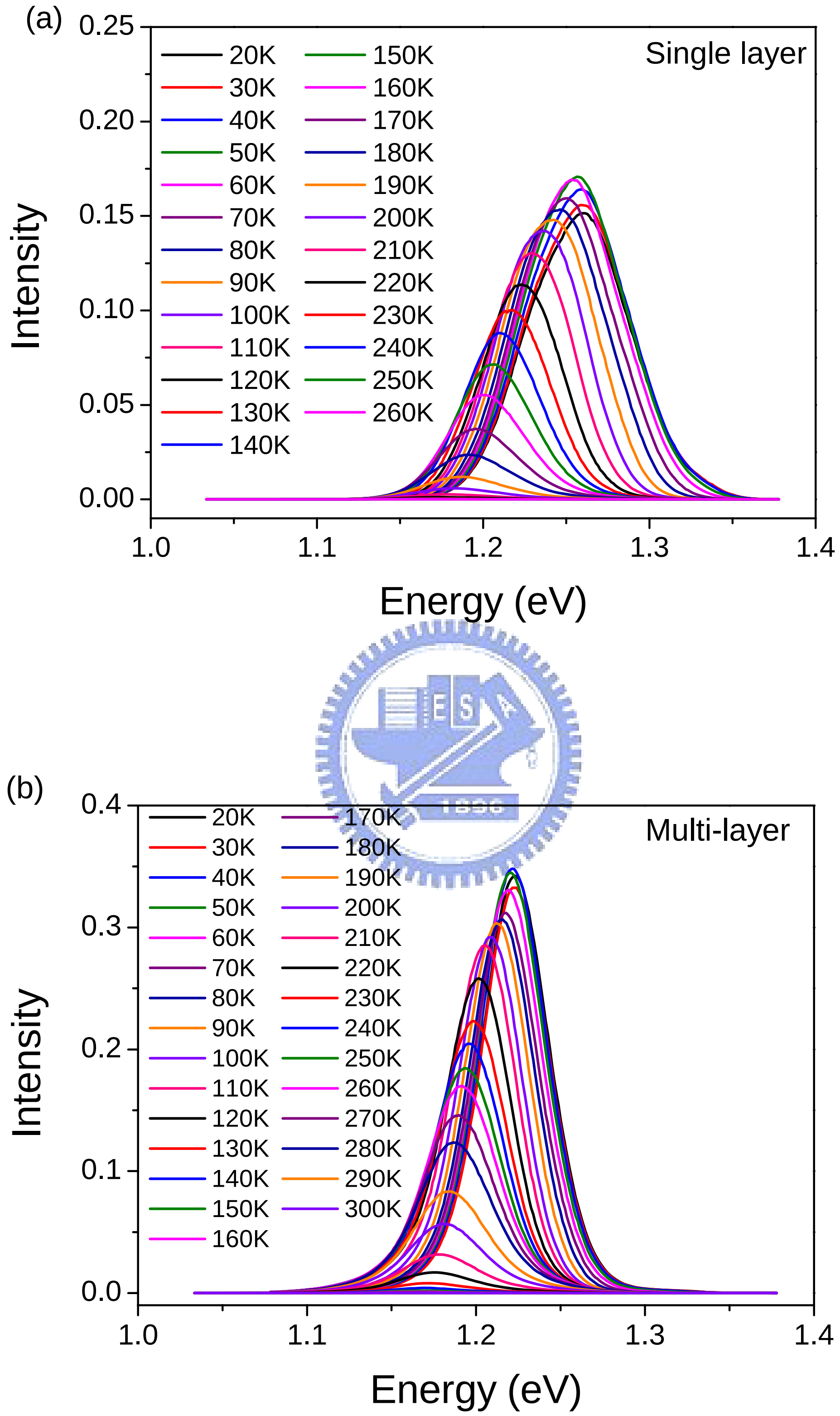

Figure 5.2: The PL spectra of (a) single and (b) multi-layer samples at different temperature.

The scatter curves of Fig. 5.3 shows the dependence of the peak energies of the PL spectra of these two samples. In principle, the peak energy shift rate is followed the Varshni law, which describes the material band gap energy as a function of temperature. The Varshni is expressed as:

$$E_g = E_0 - \frac{\alpha \cdot T^2}{T + \beta} \tag{5.1}$$

where the E_g is the band gap energy, E_0 is the band gap energy at 0K, T is temperature, and α, β is the material constant (α=2.76×10^{-4}, β=83 for InAs). However, the peak energies of the QD samples exhibit a sigmoid dependence on temperature [51]. From 50K to 140K, the red shift rate of the PL peak energy with temperature is much faster than that of InAs band gap. The continuous curves of Fig. 5.3 show the calculated result according to the Varshni law with different E_0. The E_0 is 1.263eV and 1.22eV for single layer sample at lower and higher temperature, and the E_0 is 1.226eV and 1.22eV for multilayer sample.

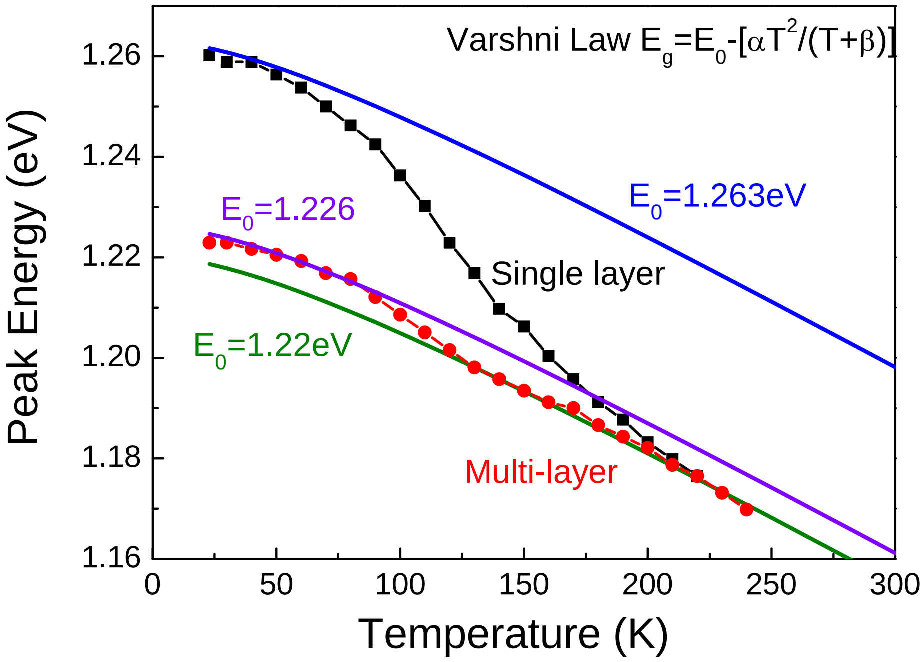

Figure 5.3: The temperature dependence of the peak energies of the PL spectra. The scatter curves are the experiment data, and the continuous curves are calculated results.

Fig. 5.4 shows the dependence of the linewidth on temperature of these two samples. The linewidth of the single layer sample shows a strong reduction when the temperature is higher than 50K, and reaches a minimum value at 140K [52]. The linewidth reduction is about 18.4meV from 50K to 140K. However, the linewidth reduction is only about 2meV for the multilayer sample, and the minimum value is at 100K.

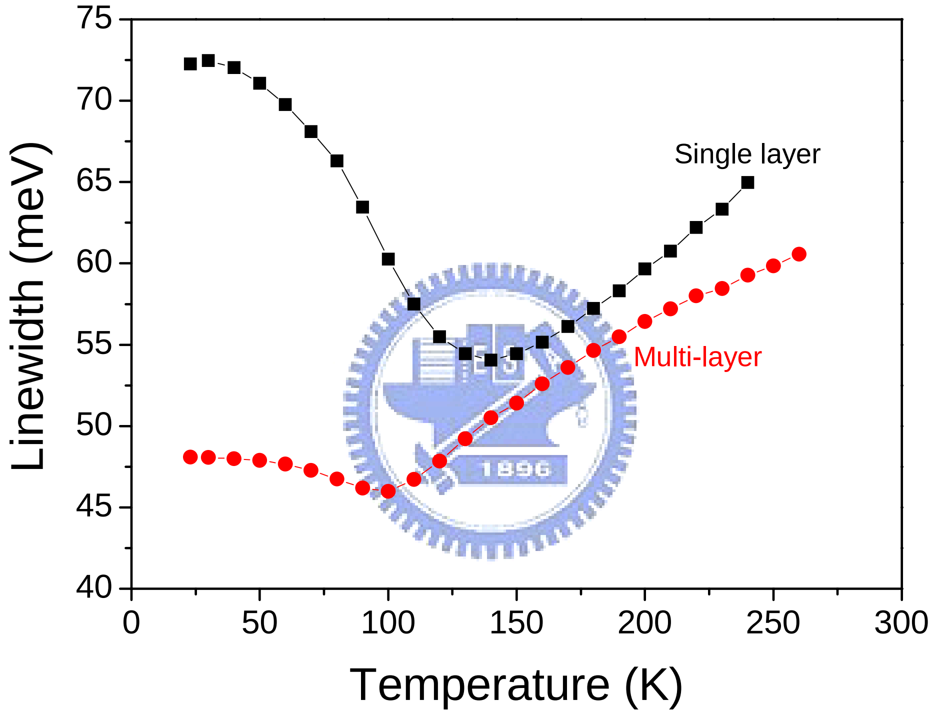

Figure 5.4: The FWHM of single and multi-layer samples at different temperature.

These two behaviors, faster peak energy red shift rate than bulk material and linewidth reduction, is caused by the thermal activated carriers transfer process. The carrier can escape from a QD and re-trap by the other QDs as the temperature increase. The QDs with lower ground state energy level and larger size have smaller escape probability and higher trapping probability. As a result, the smaller QDs wouldn't contribute to the PL spectrum at higher temperature. Therefore, the temperature dependence PL peak energy shows a faster red shift phenomenon and the linewidth reduction as the temperature raises. The larger size variation of the QDs results in larger peak energy shift and larger linewidth reduction. The linewidth of the vertically coupled QD samples is much smaller than single layer samples, because the ground state energy level variation between different QDs column is much smaller. Therefore, the temperature dependence PL peak energy red shift and linewidth reduction is not obvious in vertically coupled QD sample. The carriers in QDs can diffuse to the neighbor QDs via the miniband formed in the vertically coupled QDs column. Therefore, the vertically coupled QDs column could be assumed as a larger QD with larger carrier capture crossection and higher carrier capture probability.

5.3 Vertically coupled QDIPs characteristics

Two samples (Lm4662, Lm4715) were prepared by Varian Gen-II MBE system on (001) GaAs semi-insulating substrates. Different active regions, which was sandwiched between two 500nm silicon doped contact layers, were used in the two samples. The structure of sample A is the same with the device discussed in chapter 4. The schematics and band diagram of this structure is shown in Fig. 4.1. Sample B was a vertically coupled QDIP (VC-QDIP) with 7 periods of InAs QDs and thin 10 nm GaAs spacers. Due to the growth of the vertical aligned process, the thin AlGaAs blocking layer structure in sample A was not practical in sample B. A 50nm $Al_{0.27}Ga_{0.73}As$ current blocking layer was inserted on top of the bottom contact layer instead. In order to control the stress in the active region and avoid the generation of dislocations, fewer layers of QDs were used in sample B. The growth condition for barriers and InAs QDs were kept the same for the two samples.

The sample B was first examined with the high resolution crossection transmission electron microscopy (TEM) to check the vertical alignment of the QDs. Fig. 5.5 shows the TEM picture of sample B with well aligned QDs along the growth direction.

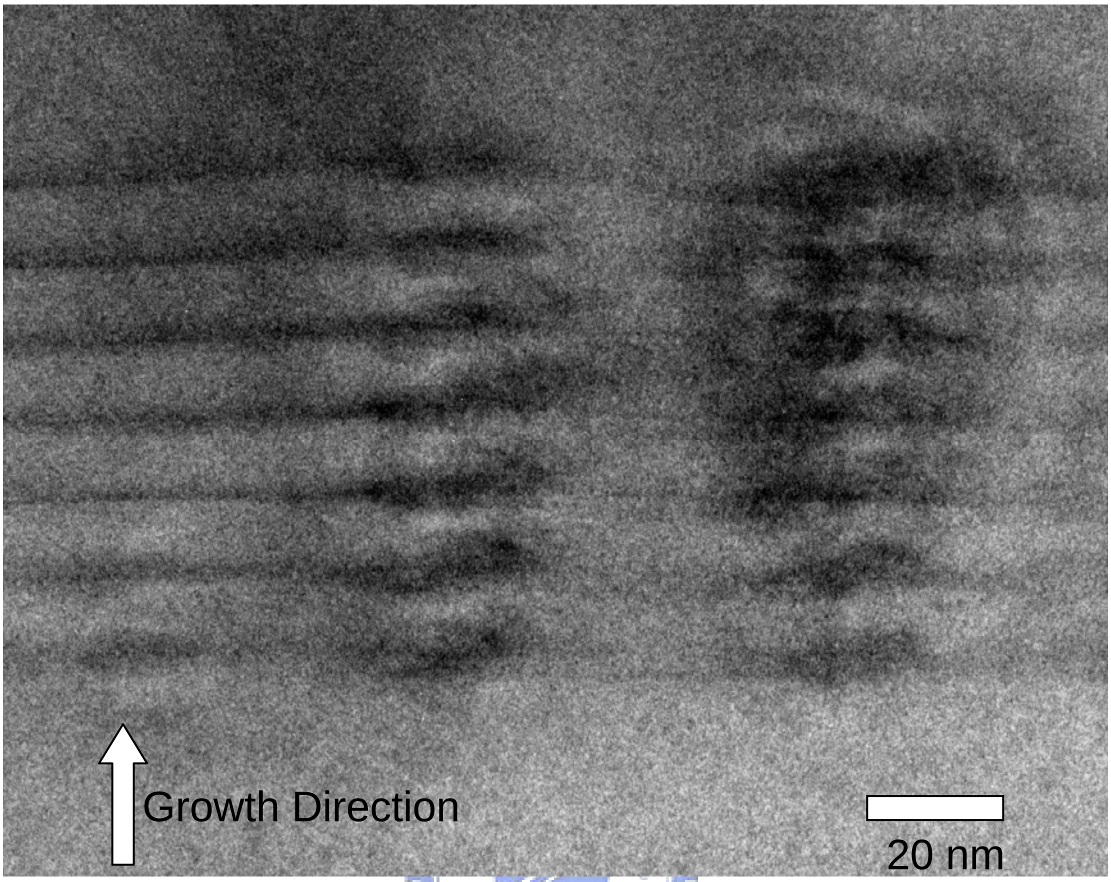

Figure 5.5: The crossection TEM image of the device B.

The QDs increases in radius but decreases in height as the layer number increases. The local strain relaxation facilitates the QDs formation directly on the top of the QDs in the previous layer [48]. Such strain relaxation is expected to be reduced with the increase of GaAs capping layer thickness. In sample B, the 10nm GaAs capping layers was thin enough to ensure the QDs to be aligned in the growth direction. On the other hand, 50nm capping layer in sample A is too thick for the strain field to propagate to the next QD layer and the QDs are therefore not aligned as shown in fig. 2.8. However, it should be mentioned that from the TEM result, not all of the QD columns in sample B contains 7 layers. Due to the non-uniform strain distribution, some of the QDs are not well aligned along the growth direction [49].

The thin GaAs barrier allows the electronic wave functions of QDs in the same column overlap and generate mini-bands [48]. The QDs with different sizes share the same quantum states which result in narrower absorption spectrum which in turn enhance the quantum efficiency. The formation of the mini-bands was confirmed by the photoluminescence (PL). 20K PL spectrum peak was at 1.13eV and 1.01eV for samples A and B, respectively. The clear red shift of the PL peak in sample B indicates the coupling of the states between the QDs which decreases the lowest ground state energy. In the PL spectrum of sample B, a small peak near 1.13eV was also observed. The signal from the uncoupled QDs shown in the TEM result was detected in the PL spectrum. After the wafer level tests, individual devices were then produced by standard lithography, wet etching and metallization techniques. All measurements were performed with normal incident radiation from the mesa top, and the bottom contact was referred as the ground.

5.4 Result and Discussion

The mini-bands reduced the full width at half maximum (FWHM) of photocurrent spectrum of sample B. Fig. 5.6 shows the normalized photocurrent spectra of samples A and B at 40K. The photo current peak of sample A was about 5.6μm with the FWHM of 1.4μm ($\Delta\lambda/\lambda_p \sim 25\%$). On the other hand, two absorption peaks were observed in sample B. The smaller peak (B_2) in sample B is consistent with the response spectrum of sample A. It is associated with the uncoupled QDs. The major signal (B_1) was around 6.6 μm and the FWHM was only 0.4 μm ($\Delta\lambda/\lambda_p \sim 6\%$). The FWHM of the photocurrent spectrum of sample B is much narrower than that of sample A.

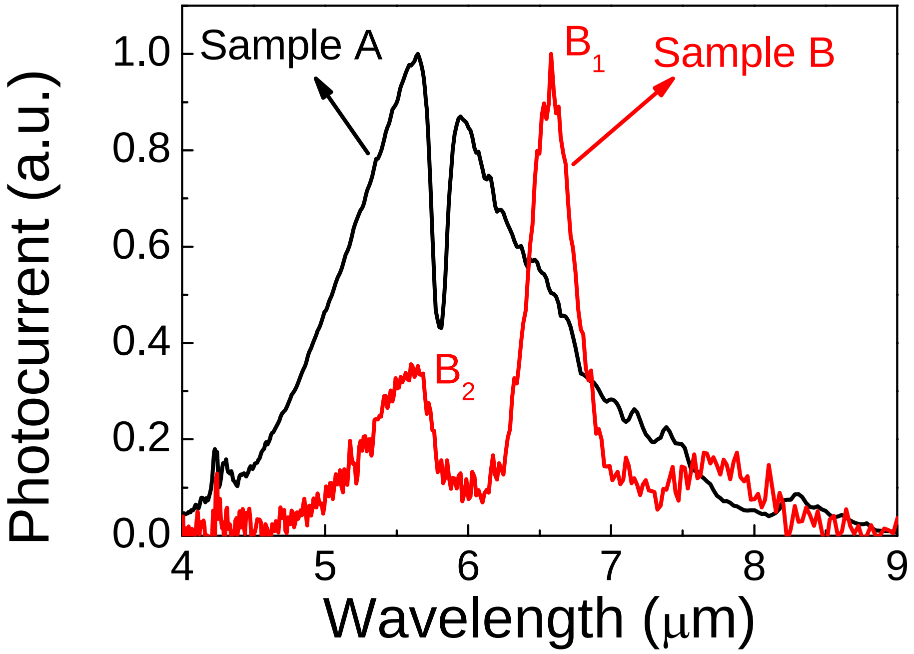

Figure 5.6: The 40K photocurrent response spectra of sample A and B.

The mini-bands shared by the QD layers in sample B provide common states for the intersubband absorption and reduced the FWHM which mainly comes from the size non-uniformity of the QDs in sample A. In QWIPs, the devices with mini-bands usually provide wider absorption band than the discrete quantum well devices due to the broadening of the mini-bands with more than 100 periods of superlattice. But instead the mini-bands formation in QDIPs reduced the broadened absorption linewidth caused by the size fluctuation of individual QDs, resulting in narrower absorption spectrum.

The device noise performance was measured to calculate the current gain and the quantum efficiency. Assuming the G-R noise dominates, the noise current gain of sample A and B at 77K was shown as a function of average electric field in fig. 5.7.

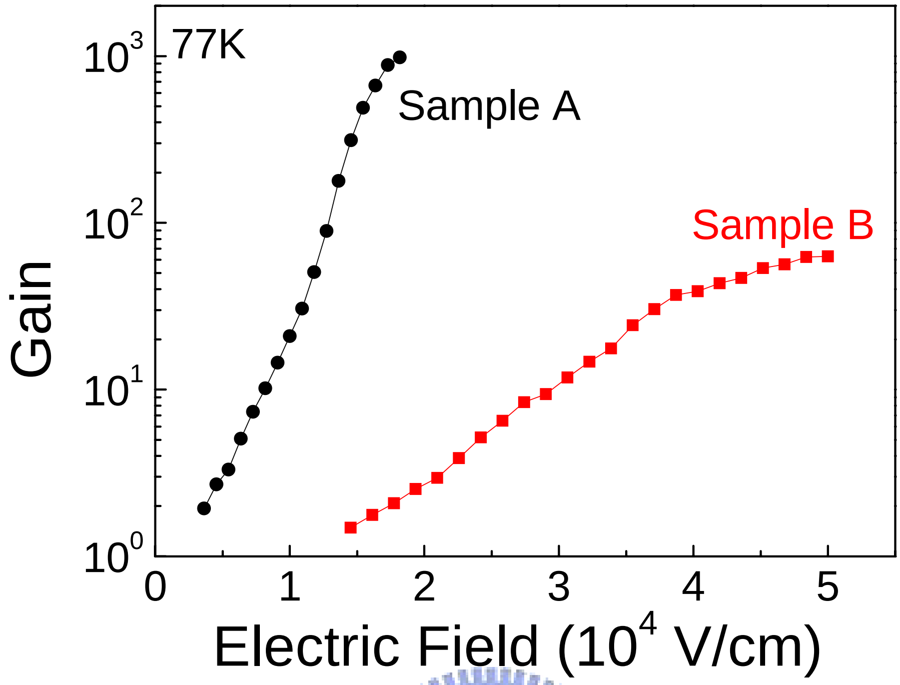

Figure 5.7: The 77K noise current gain of sample A and B as a function of the average electric field.

Dramatic decrease of the current gain of sample B was clearly observed compared with that of sample A. The current gain in sample B was few orders of magnitude lower that of sample A under the same average electric field. This indicates a major difference in the transport characteristics between the two samples. It is known the current gain of QDIPs could be expressed as equation 3.7. Since the two samples have similar filling factor, the capture probability was thus much higher in sample B even the layer number is higher in sample A. The formation of the mini-bands extends the electron wavefunction and effectively increases the cross section of the QDs and the capture probability of the carriers. Also, it was proposed the capture probability is strongly connected to the charge inside the QDs [41]. The repulsive charge in the QDs repels the carriers to be captured into the QDs and leads to low capture probability. In the vertically coupled QDs, the mini-bands facilitate the carrier redistribution between the layers. The chance to generate high repulsive coulomb potential was much lower than the case in the conventional QDIPs.

The higher capture probability was expected to improve the charging process of the QDs. The response photocurrent density was measured with standard lock-in technique at different chopper frequencies. The measurement was performed at 0.5 V and 40K. The dark current density of these two samples at this operation condition was quite close (1×10^{-9}A/cm^2) to ensure similar resistance level for the two samples. The similar resistance levels were used in the two samples for fare comparison. Fig. 5.8 shows the normalized frequency response photocurrent of the two samples. The roll-off frequency was only around 500Hz of sample A but increased to about 8000Hz of sample B. As expected, the higher capture probability in VC-QDIPs shortens the charging process and greatly increases the roll-off frequency.

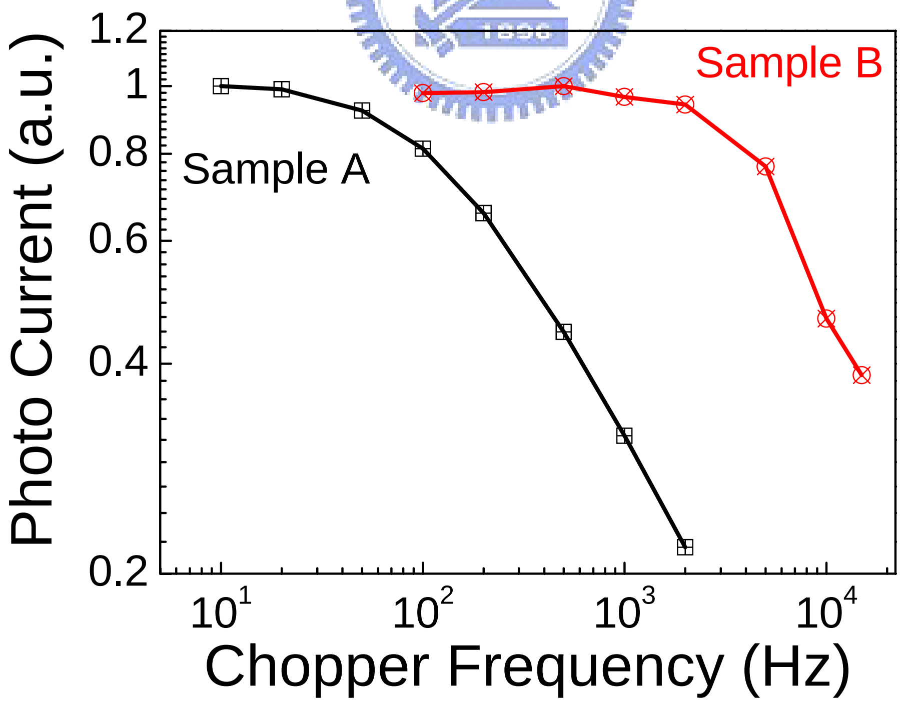

Figure 5.8: The normalized frequency response of photocurrent of sample A and B at 40K and 0.5V.

With the current gain and responsivity measured, the quantum efficiency of the two samples was also calculated. Fig. 5.9 shows the quantum efficiency of these two samples at 77K. The peak quantum efficiency at 77K is 0.23% and 0.78% for sample A and sample B, respectively. The narrower bandwidth of the VC-QDIP enhances the quantum efficiency even though only 7 layers of QDs were used in sample B. However, the low current gain in sample B counteracts the higher quantum efficiency and leads to lower responsivity in sample B. The responsivity in sample A was about 1A/W at 0.7V and 77K, but it was only 0.1 A/W under the same condition in sample B. At 0.6V and 60K, the detectivity for sample A was 1.9×10^{10} cmHz$^{0.5}$/W, which was slightly higher than that of sample B (1×10^{10} cmHz$^{0.5}$/W). As mentioned, in sample B, some QDs are not well aligned and the layer number is not as high as in sample A. More study on the vertical alignment of the QDs to increase the layer numbers and to avoid the uncoupled QDs will further enhance the quantum efficiency and the performance of the VC-QDIPs.

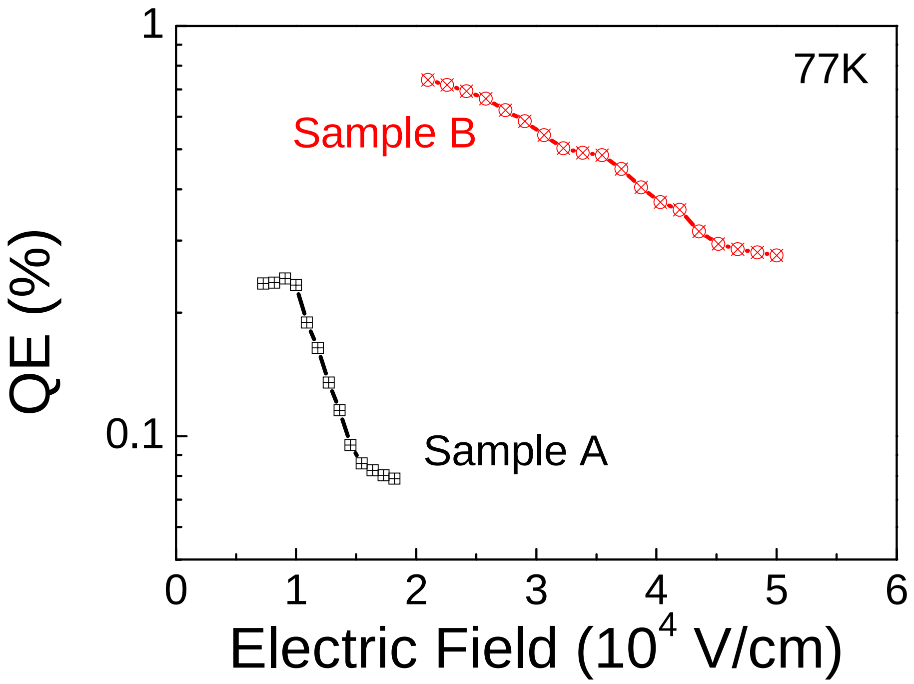

Figure 5.9: The quantum efficiency of sample A and B at 77K.

5.5 Summary

In summary, vertically coupled QDIPs have been investigated in this study. With the mini-bands in the coupled QDs, the responsivity spectrum and the roll-off frequency for QDIPs have been improved. The responsivity spectrum showed a fractional spectral width of only 6% $(\Delta\lambda/\lambda_p)$ which increased the quantum efficiency. The mini-bands also enhanced the capture probability and the roll-off frequency dramatically. The device provided a possible solution to enhance the quantum efficiency and roll-off frequency at the same time. More works to improve the vertical alignment of the QDs will further improve the performance of the VC-QDIPs.

Chapter 6

Photocurrent Spectrum Tuning of Quantum Dot Infrared Photodetectors

The quantum dot infrared photodetectors (QDIPs) with additional thin $Al_{0.2}Ga_{0.8}As$ layer near the quantum dot (QD) layers were studied. With the thin $Al_{0.2}Ga_{0.8}As$ layer, the carrier transitions of the QDIPs can be refined. The board absorption peak of the InAs/GaAs QDIPs splits into two response peaks with the additional $Al_{0.2}Ga_{0.8}As$ layer. These two signals have different behaviors as the spacing between the $Al_{0.2}Ga_{0.8}As$ layer and QDs is changing. One of the peaks remains fixed at the same wavelength, and the other peak shifts to higher energy and the intensity becomes weaker as the $Al_{0.2}Ga_{0.8}As$ layer is closer to the QD layers. A much narrow photocurrent spectrum was observed when the $Al_{0.2}Ga_{0.8}As$ layer is 5 nm to the QDs. The fractional spectra width is reduced from 25% to 10% and the quantum efficiency is enhanced. Combining with the reduced dark current due to the higher barrier, the detectivity increases for about 5 times.

6.1 Introduction

The response photocurrent spectrum of QDIPs is hard to adjust compared to that of QWIPs. It is not easy to adjust the self assembled QD’s energy levels by simply changing the dot sizes and keep the best density and uniformity. By changing the matrix material of the QDs, the QD’s energy levels can be adjusted and the device photocurrent spectrum can be tuned [53]. However, the device characteristics also change due to the different barrier structures and the QD quality also depends on the matrix material. Some compromise of the device performance is needed to obtain the required spectrum. Recently, with additional InGaAs wells, the dot-in-a-well structure has been demonstrated to provide the flexibility to alter the response wavelength [54]. However, the InGaAs layers increase the strain in the active region and make it more difficult to increase the QD layer numbers in QDIPs. In this study, instead of changing the matrix material, thin wide band gap layers are inserted under the QDs to adjust the QD's energy level and tune the photocurrent spectra of QDIPs. With the proper design, the spectra width can be reduced and the device performance is thus enhanced.

6.2 Sample Structure

Four samples were prepared by a Varian Gen-II MBE system on (001) semi-insulation GaAs substrates. Different active regions sandwiched between two 500nm silicon doped contact layers were used in the four samples. Ten layers of InAs QDs, each with 2.6 MLs InAs, were deposited at 520℃ with a 0.05 ML/s growth rate. Each QD layer was capped with a 3nm $Al_{0.2}Ga_{0.8}As$ layer, and the layers was separated by a 50nm GaAs barrier layer [23]. The $Al_{0.2}Ga_{0.8}As$ capping layer was used to reduce the device dark current and increase the device performance. A delta doped silicon layer was inserted 2nm beneath each QD layer to supply electrons in the QDs. Sample A was the control sample with the structure mentioned above. For samples B, C and D, an additional 1nm $Al_{0.2}Ga_{0.8}As$ layer was inserted below each QD layer at a distance of 11nm, 7nm and 5nm, respectively. A QD layer was grown on the sample surface with the same growth condition with the embedded QDs for atomic force microscope (AFM) study. The QDs density was about 1.6×10^{10} cm^{-2}, and the average size of the QD is about 10nm in height and 50nm in base radius. Fig. 6.1 shows the schematic drawing of the device structure and the energy band diagram. Fig. 6.2 shows the surface AFM image. Standard photolithography and wet chemical etching procedures were used to define the mesas and ohmic contacts. In all measurements, the bottom contact was referred to as ground. The photo response was measured under the normal incident configuration.

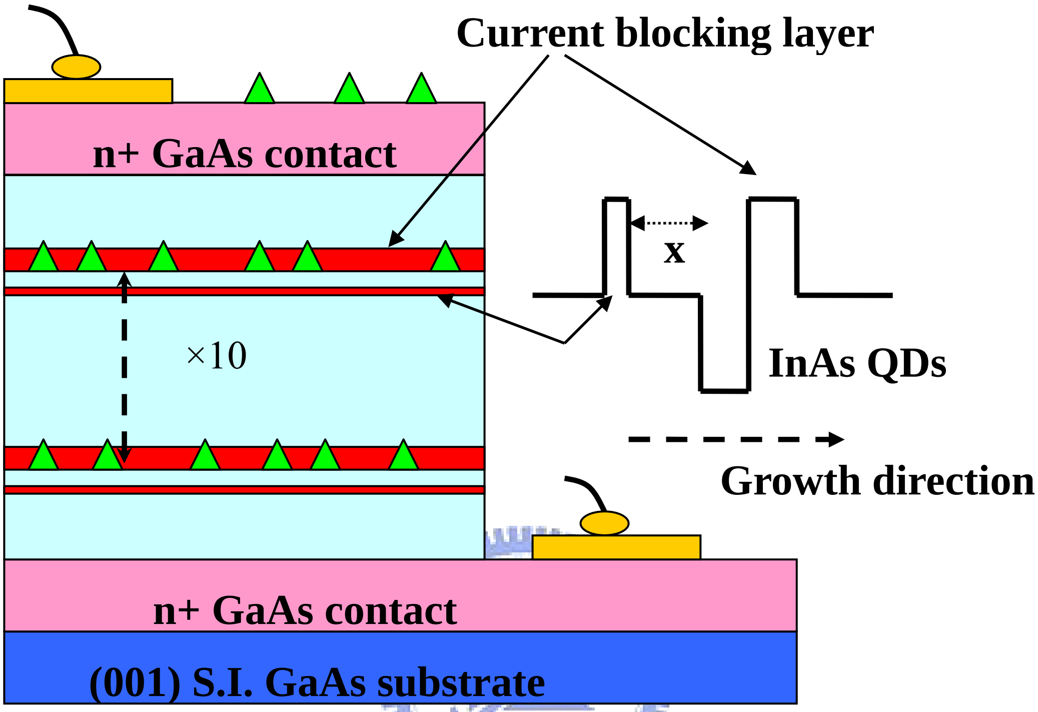

Figure 6.1: The schematic drawing of the device structure used in this study. Inset shows the band diagram of the QDs in the active region.

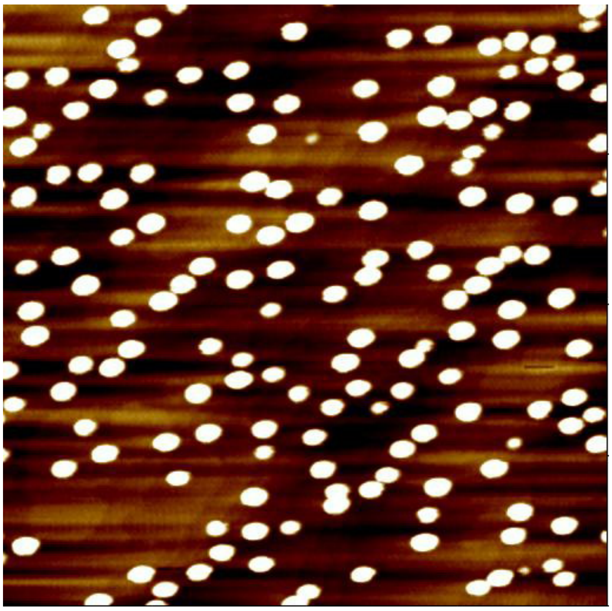

Figure 6.2: The surface AFM image of sample A (1μm×1μm).

6.3 Result and Discussion

The photocurrent spectra were measured by a Fourier Transform Infrared Spectroscopy (FTIR) system. Fig. 6.3 shows the normalized photocurrent spectra of the four samples at 40K and 1V.

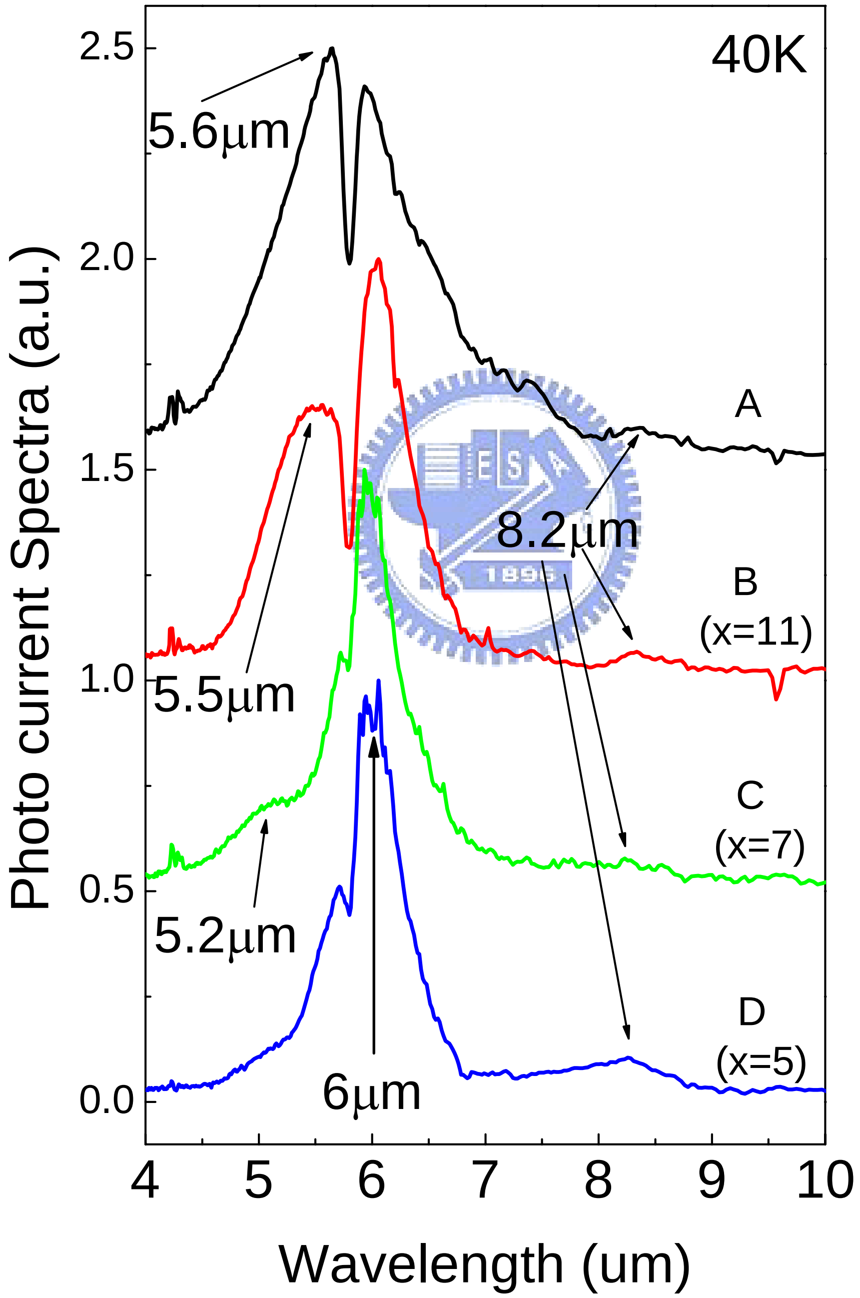

Figure 6.3: The normalized photocurrent spectra of these four samples at 40K and 1V.

For sample A, a broad detection spectrum was observed similar to those reported by others [54]. A sharp absorption dip at 5.8μm (214meV), which was observed in all our samples and those by others, was probably due to absorption by defects or impurities. With the insertion of the $Al_{0.2}Ga_{0.8}As$ layer, the broad response peak separates into two peaks. Apparently, the originally thought single peak is actually from two transitions with similar energies. These two transition peaks show different properties as the distance between the $Al_{0.2}Ga_{0.8}As$ layer and the QDs is changed. The peak at 6μm is almost fixed regardless the distance X. The other peak with slightly higher energy shifts toward shorter wavelength as the $Al_{0.2}Ga_{0.8}As$ layer is closer to the QDs. The intensity of the higher energy peak becomes weaker with the decrease of the distance X. When the distance decreases to 5nm in sample D, the high energy peak is too weak to be observed and only the response peak at 6μm could be observed. The full width at half maximum (FWHM) of the spectrum in sample A and D are 1.4μm and 0.6μm, respectively. The fractional spectrum width reduces from 25% to 10%.

In order to analyze the carrier transitions of these devices, the energy states of the QDs were measured by micro-photoluminescence (micro-PL) and photoluminescence excitation (PLE) system. Fig. 6.4 shows the 77K micro-PL and 1.4K PLE measurement result of sample A. The micro-PL excitation power density is about 10^5 W/cm^2 which generates information of the four lower transitions (E_0~E_3) of the QDs. To further probe the higher energy states, PLE measurement was executed with detection level at the ground state energy level of the 1.4K PL measurement, and the excitation power was kept as low as only the ground state signal appears in the spectrum. Three highest transitions of the QDs were observed, and the lowest energy peak of the PLE spectrum is the same as the E_3 transition shown in the micro-PL spectrum. Combining the micro-PL and PLE result, six transitions (E_0~E_5) were observed in the QDs. The transition energies are 1.11eV, 1.18eV, 1.25eV, 1.32eV, 1.42eV and 1.47eV. The associated six electron states (C_0~C_5) in the conduction band generate the photocurrent spectrum in our samples.

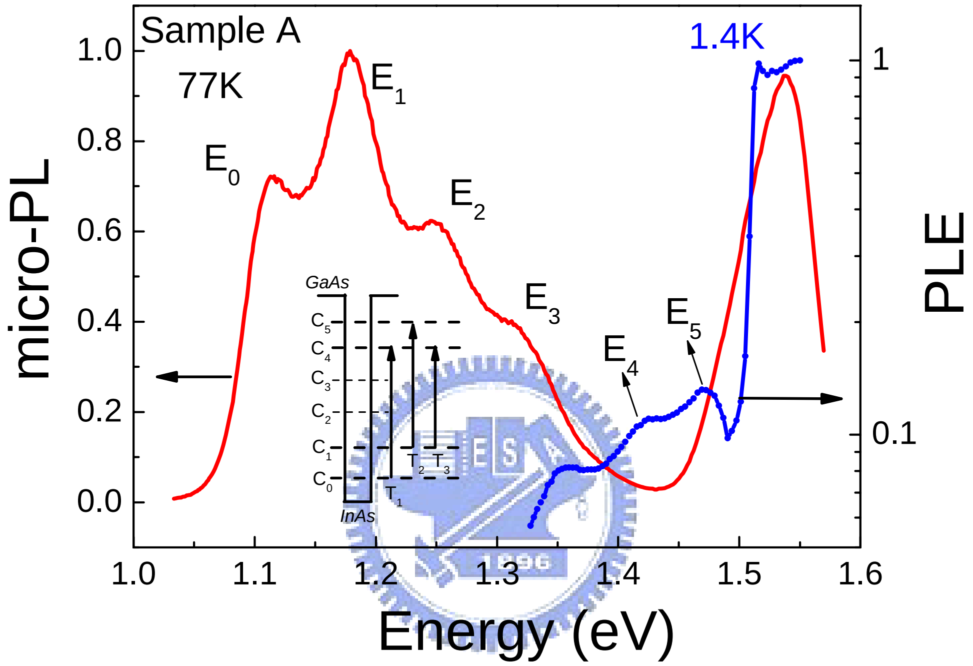

Figure 6.4: The 77K micro-PL and 1.4K PLE spectra of sample A. The inset shows the six electron states and possible intersubband transitions.

The transitions that generate two similar peaks in sample A are probably from C_0 to C_4 and from C_1 to C_5 assuming an energy discontinuity about 70% in the conduction band. The broad photocurrent spectrum of sample A could be fitted with two gauss curves with the peaks at 205meV (6µm) and 222meV (5.6µm). The longer wavelength peak at 6um doesn't dependent on the position of $Al_{0.2}Ga_{0.8}As$ layer, while the shorter wavelength one changes with the spacing between the $Al_{0.2}Ga_{0.8}As$ layer and QD layer. The 6µm transition peak could be deduced to be from C_0 to C_4, and the 5.6µm transition peak could be deduced to be from C_1 to C_5. Besides, the

8.2μm (151meV) response peak is from C_1 to C_4. The inset of fig. 6.4 shows the schematic drawing of the transitions. The T_1, T_2, and T_3 transitions correspond to the 6μm, 5.6μm, and 8.2μm photocurrent peaks. It is noticed that the transition from C_0 to C_5 was not observed in the photocurrent spectra. It might be due to the weaker oscillator strength [39, 55].

The observed spectra change in the series of samples can be explained with the PLE results. Fig. 6.5 shows the normalized PLE spectra of the four samples as a function of energy difference between excitation laser energy and detection energy.

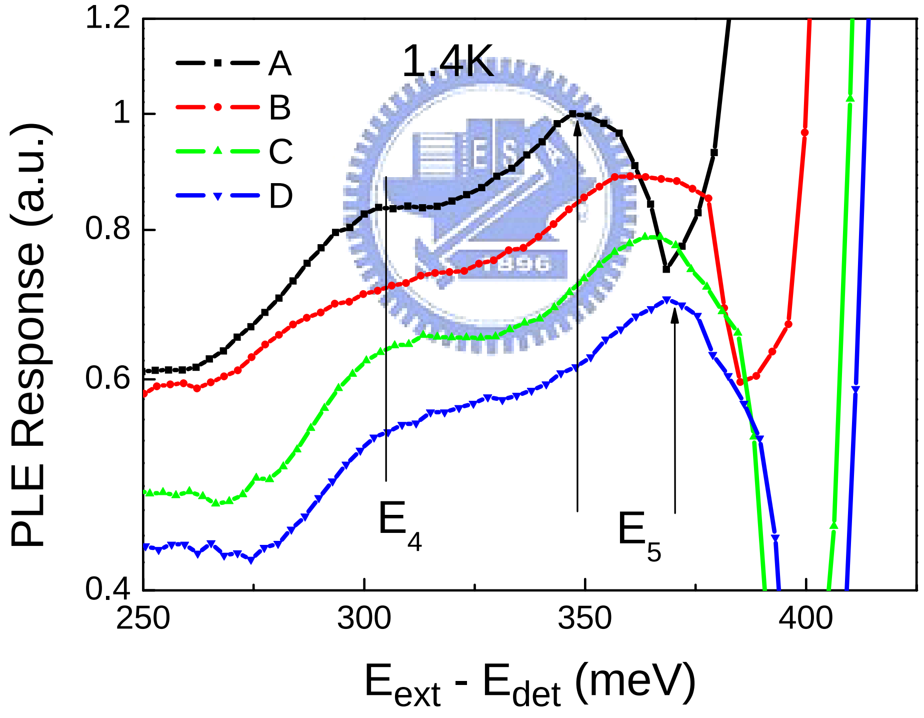

Figure 6.5: The PLE spectra of four samples at 1.4K as a function of energy difference between excitation laser energy and detection energy.

The location of E_4 and E_5 transitions are clearly identified. The E_4 transition energy is almost the same for all samples while the E_5 transition energy increases as the $Al_{0.2}Ga_{0.8}As$ layer is closer to the QD layer. The E_5 energy shifts about 23meV between sample A and C. This result is consistent with the energy shift of the photocurrent peak. Since C_5 is the highest energy electron state of the QD, the wavefunction extends more outside of the QD. With the insertion of $Al_{0.2}Ga_{0.8}As$ layer, C_5 state can be easily affected and pushed out of the QD. Therefore, the wavefunction overlap of the C_1 and C_5 reduces, and the carrier transition oscillator strength decreases. As a result, the response intensity would become weaker and weaker as the spacing decreases.

To further examine the proposed transitions, a simple single particle electron state calculation was executed using one band Hamiltonian with the material dependent effective mass approximation. The shape of QD is assumed as cone shape with 40nm in base diameter and 8nm in height. The cylindrical symmetry wavefunction can be expressed as:

$$\psi(r,z,\phi)=\chi(r,z)\cdot e^{il\varphi} \tag{6.1}$$

where φ is azimuthal angle, and l is the angular quantum number. The InAs QD is embedded in the GaAs matrix and capped by $Al_{0.2}Ga_{0.8}As$. The structure is the same with sample A. The electron effective mass is $0.044m_0$ and $0.067m_0$ for strained InAs and unstrained GaAs, respectively. The conduction band energy difference of GaAs and strained InAs is assumed as 419meV, and that of $Al_{0.2}Ga_{0.8}As$ and GaAs is assumed as 154meV [33]. Fig. 6.6(a) shows the schematic drawing of the simulation structure, and fig. 6.6(b) shows the calculated electron state energy levels with different l number (l=0, 1). Six electron states exist (C_0~C_5) in the QD. The states with higher l number have the similar energy with these six states [56]. The energy levels are consistent with the experiment micro-PL and PLE results. The angular quantum number difference (Δl) of T_1 and T_2 transition is equal to 0 which allows the TM polarized radiation absorption. The Δl of T_3 transition is equal to 1 which allows the TE polarized radiation absorption [39, 56]. However, the transition rule might be slightly relaxed in the strained InAs/GaAs QDs and also due to the mesa edge coupling. The normal incident absorption has been observed in the strained InGaAs/GaAs QWIPs without grating fabricated on the sample surface [57, 58].

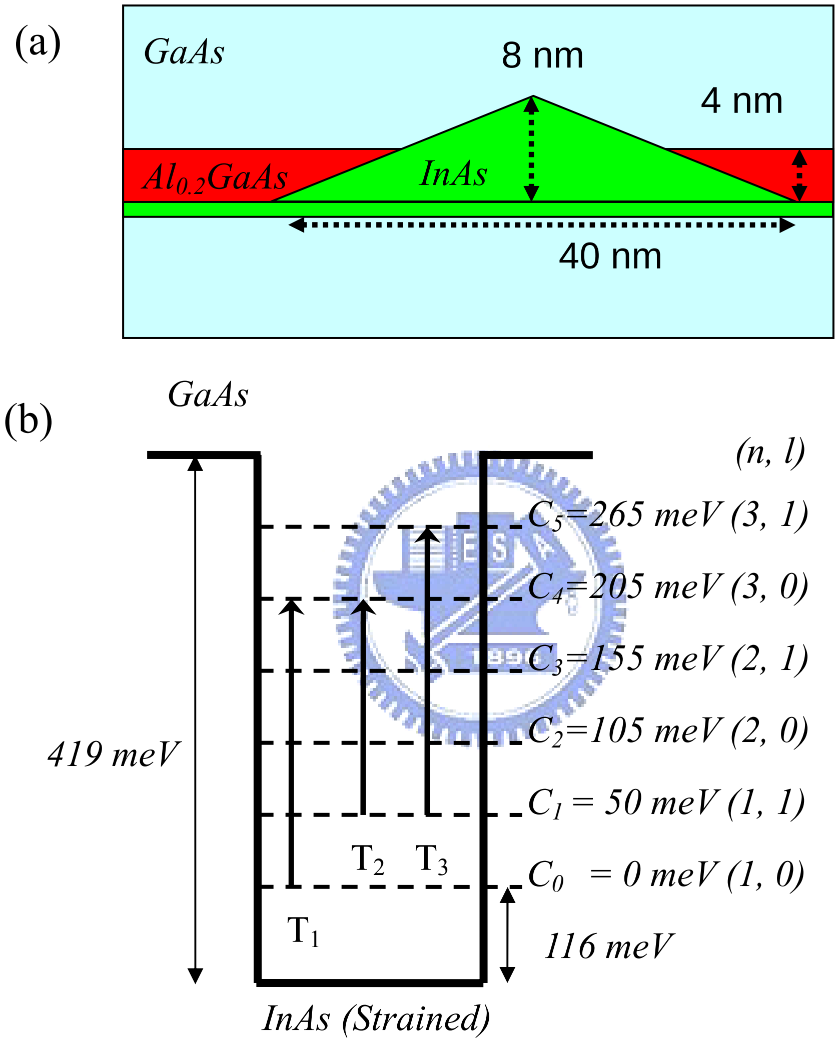

Figure 6.6: (a) The simulation structure of sample A.
(b) The simulated electron states of angular quantum number $l=0, 1$.

The wavefunction of the six electron states is shown in fig. 6.7. And, the electron transition oscillator strength of the six states is also calculated and shown in fig. 6.8. The oscillator strength of T_1 ($\Delta l=0$), T_2 ($\Delta l=0$) and T_3 ($\Delta l=1$) is 0.049, 0.01 and

2.5×10^{-3}, respectively. The oscillator strength of the T_3 is much smaller than T_1 and T_2 transitions. Therefore, the 8.2μm photocurrent peak intensity is much smaller than the other two peaks. Besides, the oscillator strength of the transition from C_0 to C_5 is 2×10^{-4}, and thus the transition is not observed in the photocurrent spectrum.

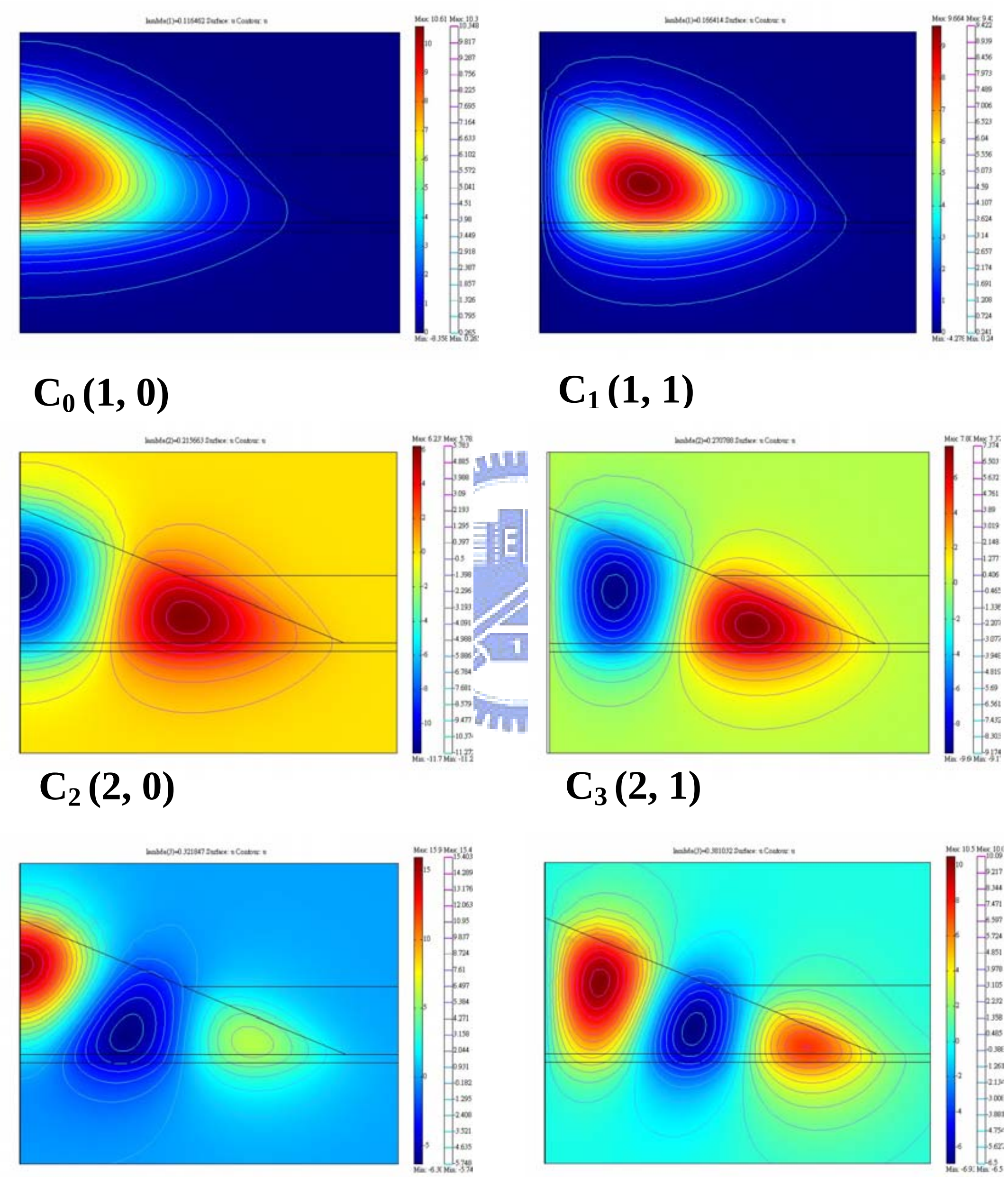

C_0 (1, 0) C_1 (1, 1)

C_2 (2, 0) C_3 (2, 1)

C_4 (3, 0) C_5 (3, 1)

Figure 6.7: The wavefunction of the six electron states.

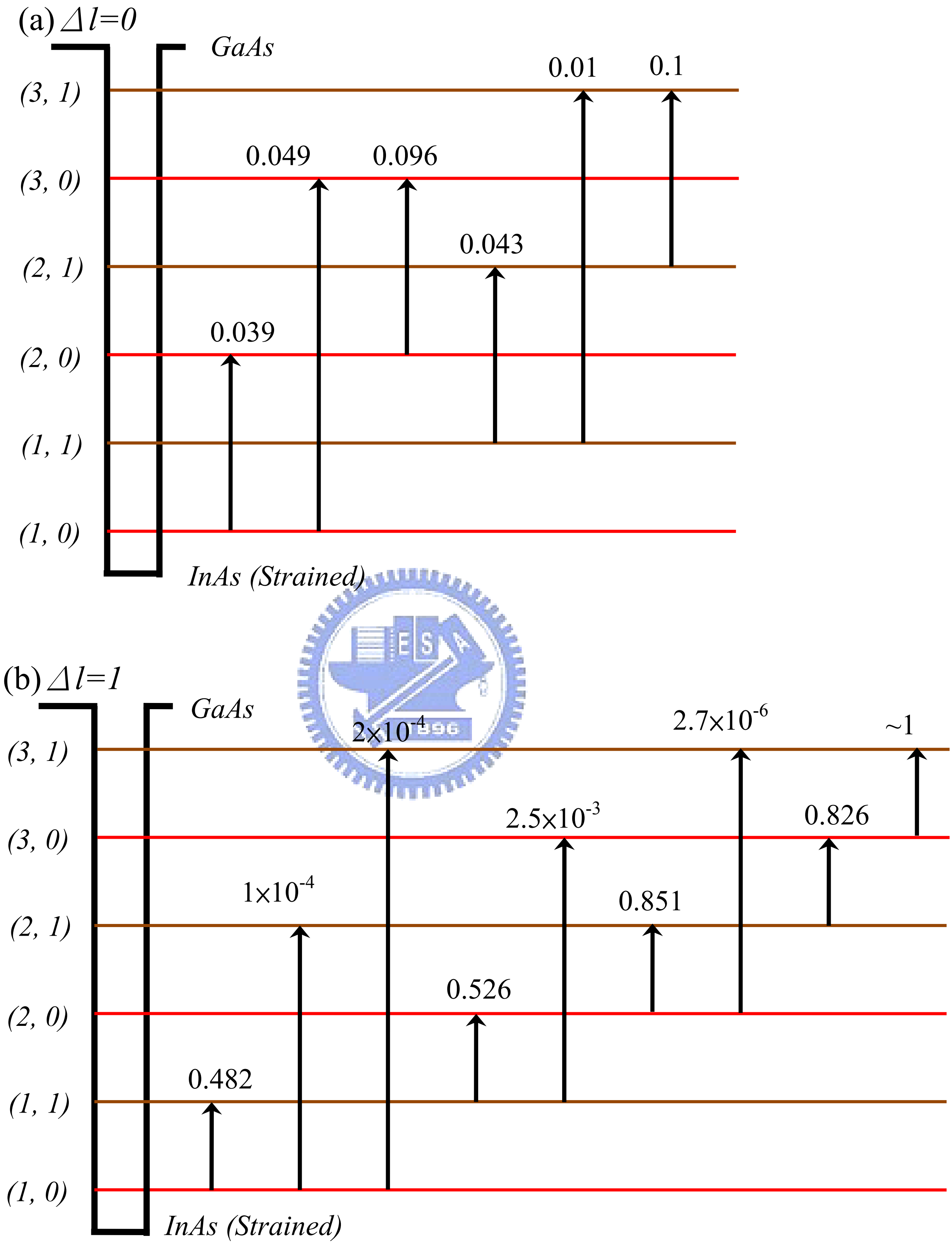

Figure 6.8: The intersubband carrier transition oscillator strength
(a) for $\Delta l=0$ (TM polarized), (b) for $\Delta l=1$ (TE polarized).

The simulation result was verified by the polarization dependence of the response spectrum. The 45° polished facet was generated to couple the polarized light. Fig. 6.9 shows the photocurrent spectra of sample B at 40K and 1V for different polarization angle of the incident radiation.

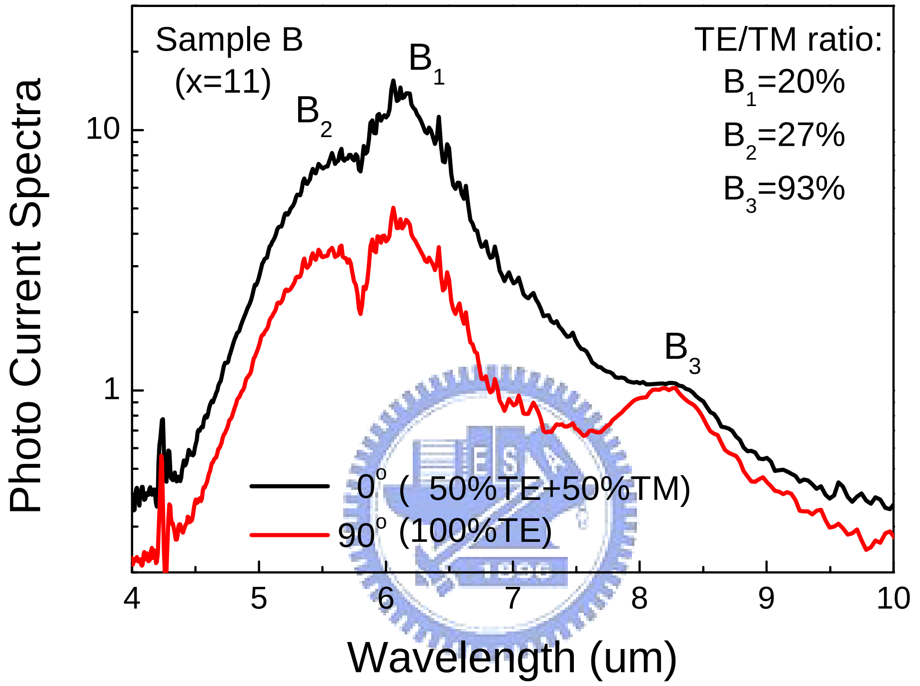

Figure 6.9: The photocurrent spectra of sample B at 40K and 1V for different polarization angle of the incident infrared light from the 45° polished facet on the detector.

The 0° polarized radiation includes 50% TE mode and 50% TM mode radiation, and the 90° polarized radiation includes 100% TE mode radiation. Three response peaks (B_1, B_2, and B_3) are corresponding to the T_1, T_2 and T_3 transitions, respectively. The three response peaks show different polarization dependence. The TE to TM response intensity ratio of the B_1, B_2, and B_3 is about 20%, 27%, and 93%, respectively. The T_1 and T_2 transitions prefer to absorb the TM polarized radiation, and T_3 transition prefers to absorb the TE polarized radiation. The results are consistent with the prediction from the simulation result. This further supported the proposed states and transitions responsible to the photocurrent spectrum.

The inserted $Al_{0.2}Ga_{0.8}As$ not only improved the response spectrum but also decrease the device dark current. Fig. 6.10 shows the dark current density and responsivity of sample A and D at 77K. The dark current density of the sample A and D is 28 and 3.2 mA/cm^2 at 0.5V and 77K. On the other hand, the normal incident responsivity of sample A and D is about 0.3 and 0.2 A/W, respectively under the same condition. The $Al_{0.2}Ga_{0.8}As$ layer largely reduces the dark current, but slightly reduces the responsivity. This is because of the better quantum efficiency in sample D. Fig. 6.11 shows the quantum efficiency and detectivity of sample A and D at 77K. The quantum efficiency of the sample D is higher than that of sample A. In sample A, two transitions (T_1 and T_2) contribute to the major photo response. In sample D, however, the T_2 transition is suppressed and only T_1 transition contributes to the major photo response. Therefore, the carriers which populate at C_1 state would relax to C_0 state and contribute to the T_1 transition and increases the quantum efficiency. Therefore, the device performance is improved. At 77K and 0.5V, the detectivity of sample A and D is 4.4×10^9 and 2.2×10^{10} cmHz$^{0.5}$/W respectively. The detectivity is largely enhanced with the additional $Al_{0.2}Ga_{0.8}As$ layers.

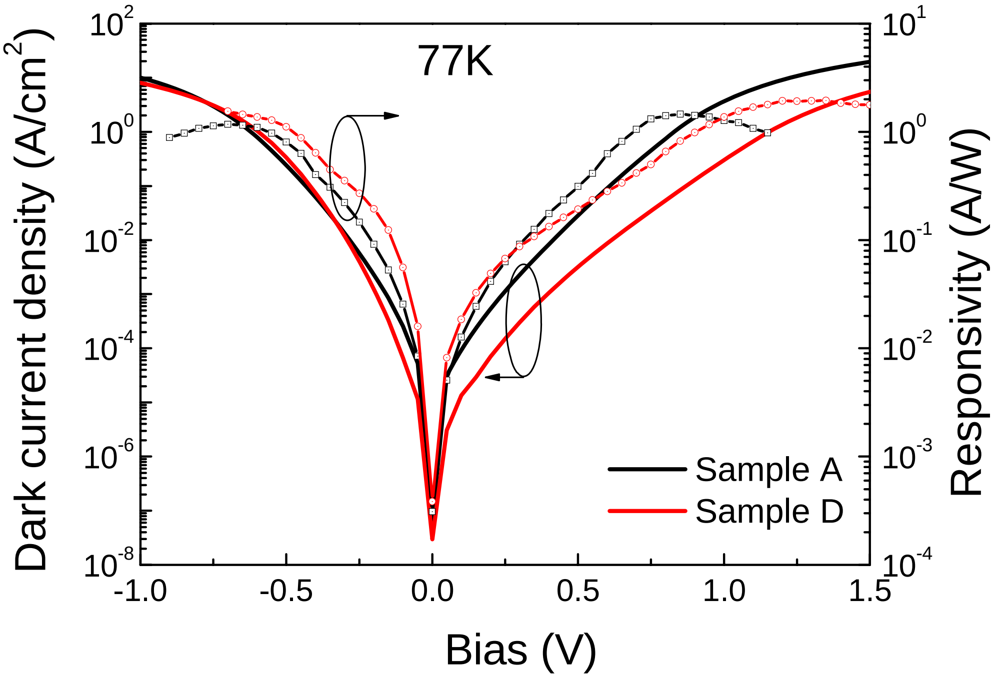

Figure 6.10: The dark current density and photo responsivity of sample A and D at 77K.

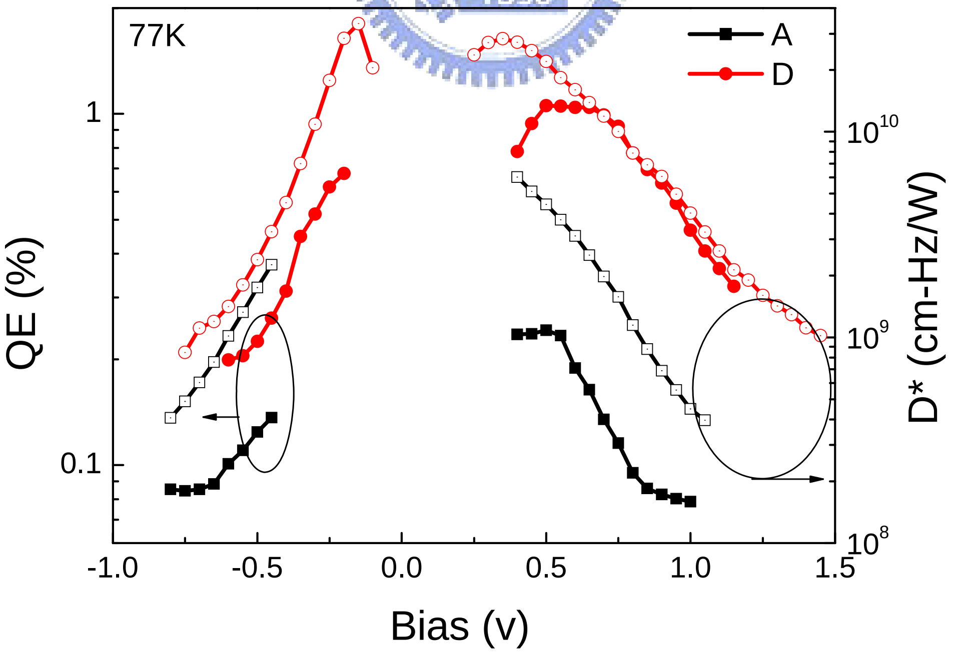

Figure 6.11: The quantum efficiency and detectivity of sample A and D at 77K.

6.4 Summary

The QDIPs with a thin wide band gap material $Al_{0.2}Ga_{0.8}As$ layer near QDs were studied. The board photocurrent spectra of the simple InAs/GaAs QDIPs are found to be composed of two transitions. With the insertion of the $Al_{0.2}Ga_{0.8}As$ layer, the response spectra could be separated into two peaks. One of the peaks is fixed at 6μm, and the other shifts to higher energy and the intensity becomes weaker as the decrease of the $Al_{0.2}Ga_{0.8}As$ layer distance. The much narrow photocurrent spectrum width is obtained, and the fractional spectrum width is reduced from 25% to 10% as the $Al_{0.2}Ga_{0.8}As$ layer is 5nm from the QD layer. The quantum efficiency increases, because one of the transitions is suppressed and the carrier would contribute to the other transition. Combining with the reduced dark current, the detectivity is enhanced for 5 times.

Chapter 7

GaSb/GaAs Quantum Structure Growth and Characterization

The growth conditions of GaSb/GaAs quantum dots were studied systematically, including the GaSb film thickness, substrate temperature, and the V/III beam equivalent flux ratio. The morphology of quantum dots is studied by the atomic force microscope. And, the excitation power density and temperature dependent photoluminescence is also studied. Due to the type-II band alignment, the result is different from the type-I band alignment system. Also, the distinct light emission peaks from GaSb wetting layer in GaAs were observed. Discrete atomic layers of GaSb for the wetting layer prior to quantum dot formation give rise to transition peaks corresponding to quantum wells with one, two and three monolayers. From the transition energies we were able to deduce the band offset parameter between GaSb and GaAs. By fitting the experimental data with the theoretical calculated result using an 8×8 $\mathbf{k}\cdot\mathbf{p}$ Burt's Hamiltonian along with the Bir-Picus deformation potentials, the valence band discontinuity for this type II heterojunstion was determined to be 0.45 eV.

7.1 Introduction

III-antimonide compounds have been regarded as potential materials for applications in ultra high-speed devices and long-wavelength photonic devices due to their high electron mobility and small bandgap energies [59, 60]. Moreover, heterostructures composed of antimonides and other III-V compounds, such as arsenites, have also been of great interests because of the unconventional type-II and type-III band alignment [5-7]. Lots of theoretical predictions for interesting optical, electronic, and magnetic phenomena in nanostructures have been made with antimonides [61]. Recently, with the advances in epitaxy technology, such nanostructures have been grown with high quality and from them many interesting experimental findings, either predicted or sometimes unexpected, have been observed. For instance, quantum wells (QWs) and self-assembled quantum dots (QDs) made by GaSb embedded in GaAs matrix, because of type-II heterostructures, can provide an opportunity for observation of optical transition between spatially separate electrons and holes around the hetero-interfaces. However, despite of a large amount of effort being put in this material system, one of the most important parameters, the band offset between GaSb and GaAs has yet to be accurately determined. The wide range of reported value in this parameter often leads to ambiguous interpretation of experimental results and theoretical predictions for nanostructures made from this system.

7.2 Growth Conditions

In this section, we investigated the characteristics of GaSb wetting layer and quantum dots in GaAs matrix in different growth conditions, including the GaSb film thickness, growth temperature and the V/III flux ratio. In our study, the GaSb films were sandwiched between a 150nm GaAs buffer layer and a 150nm GaAs capping layer. After the capping layer growth, a GaSb film with the same condition was grown on the surface for atomic force microscope (AFM) measurement. The GaSb/GaAs nanostructures were grown by a VECCO Gen-II solid source MBE system with valve cracker sources of antimony and arsenic on (001) GaAs substrates. We used As_4 as arsenic source instead of As_2 to avoid intermixing of Sb and As atoms during the growth process [62]. The cracking zone of the Sb and As cell was at 1050℃ and 500

℃. The sample structure is showed in fig. 7.1. The fig. 7.2 shows the shutter operation sequence and the substrate temperature change procedure during the GaSb film growth. The GaSb growth rate was kept at 0.2 um/hr. After the GaSb QD growth, 60sec Sb interruption was performed to increase the uniformity of the QDs. During the growth process, the As beam equivalent pressure was kept at about 2×10^{-5} torr, and the GaAs matrix was grown at 580℃.

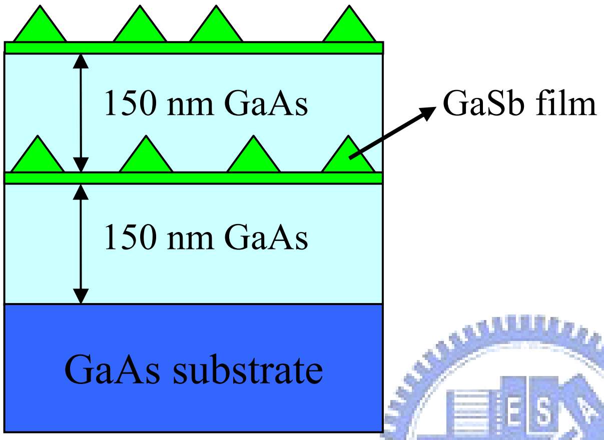

Figure 7.1: The sample structure of GaSb/GaAs QDs in our study.

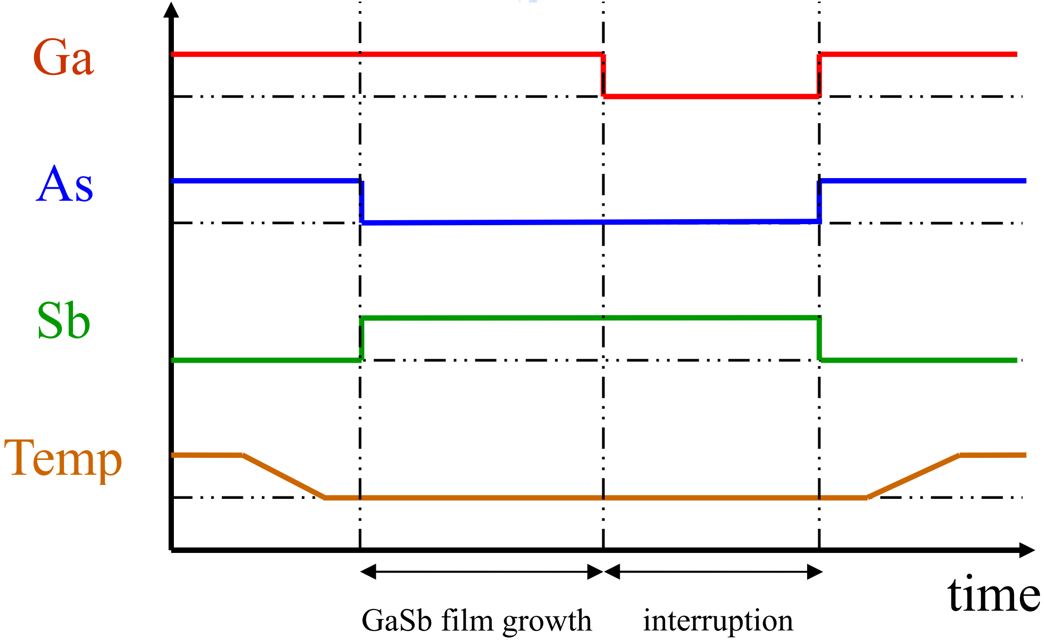

Figure 7.2: The Ga, As and Sb source shutter operation sequence during GaSb film growth. And, the substrate temperature change procedure.

7.3 Surface Morphology Study

First, we study the QD morphology in different growth conditions, including GaSb film thickness, substrate temperature, and V/III flux ratio. Tem samples (A~J) were prepared with different growth conditions by Veeco Gen-II MBE system. The surface QD morphology is studied by the atomic force microscope (AFM, Veeco D3100) system. All of the growth conditions and the surface QD density of the ten samples are listed in the table 7.1.

Sample #	Substrate Temp. (°C)	Sb BEP (torr)	V/III Flux ratio	GaSb (ML)	Dot density (10^{10} cm^{-2})
A (Rn0281)	500	4	5	1	×
B (Rn0282)	500	4	5	2	1.04
C (Rn0283)	500	4	5	3	0.9
D (Rn0256)	500	4	5	4	1.43
E (Rn0273)	540	4	5	4	~0.0072
F (Rn0274)	520	4	5	4	0.41
G (Rn0275)	480	4	5	4	2.15
H (Rn0277)	500	2.4	3	4	1.36
I (Rn0278)	500	8	10	4	0.68
J (Rn0279)	500	16	20	4	0.73

Table 7.1: The list of the GaSb quantum structure growth conditions, and surface QD density.

Fig. 7.3 shows the surface AFM image of sample A, B, C and D. These four samples were deposited with 1, 2, 3 and 4 monolayers GaSb film. The growth temperature was at 500℃, and V/III flux ratio was 5.

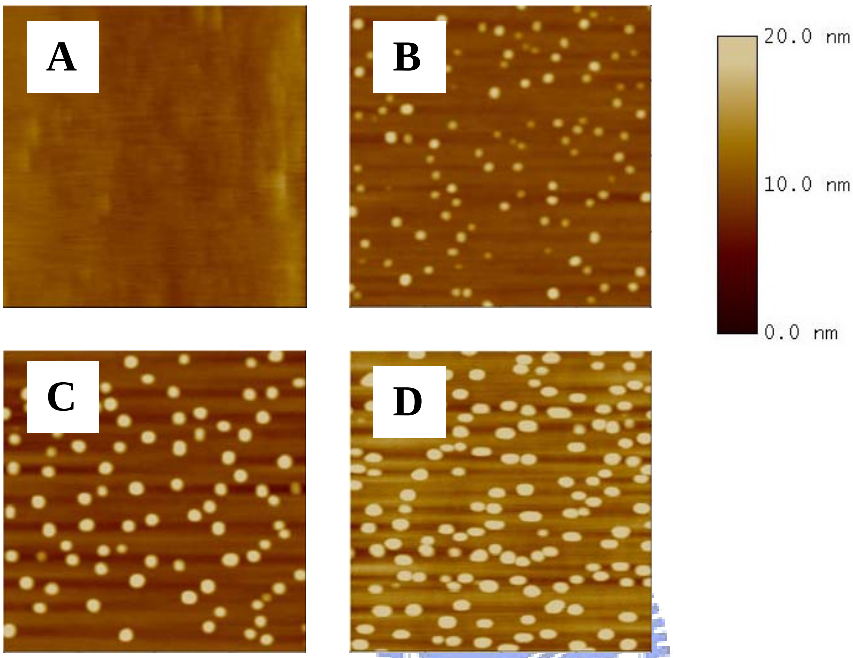

Figure 7.3: The surface AFM image of sample A, B, C, and D. The image size of sample A is 5μm×5μm, and the others are 1μm×1μm. Sample A, B, C and D was deposited with 1, 2, 3 and 4 monolayer GaSb film.

The smooth surface of sample A clearly shows that one monolayer of GaSb is not enough for quantum dot formation. However, on the surface of sample B, which had a 2-ML GaSb film, we can see clear images of quantum dots. The formation of dots implies that the strain of the GaSb film cannot be sustained pseudomorphically in GaAs surface when more than 1 ML of GaSb is deposited. This is obviously due to the large lattice mismatch (8%) between GaSb (6.06Å) and GaAs (5.65Å). When the deposit GaSb film thickness was 3-ML, the quantum dot size became larger than sample B. However, the dot density was lower than sample B, because the material of smaller QDs diffused to form larger QDs. The size uniformity of QDs in sample C is better than that of sample B. When more material deposited, the QDs density becomes higher. The dot density of sample C and D is about 0.9 and $1.43\times10^{10}\text{cm}^{-2}$, respectively.

Fig. 7.4 shows the surface AFM image of sample E, F, D and G. The substrate temperature was 540℃, 520℃, 500℃ and 480℃. The deposit film thickness was 4 ML and V/III flux ratio was 5. The higher epitaxial temperature results in lower dot density. The dot density is about 0.0072, 0.41, 1.43, and 2.15 $\times10^{10}\text{ cm}^{-2}$, respectively. The dot density decreases significantly when the epitaxial temperature raised from 520℃ to 540℃.

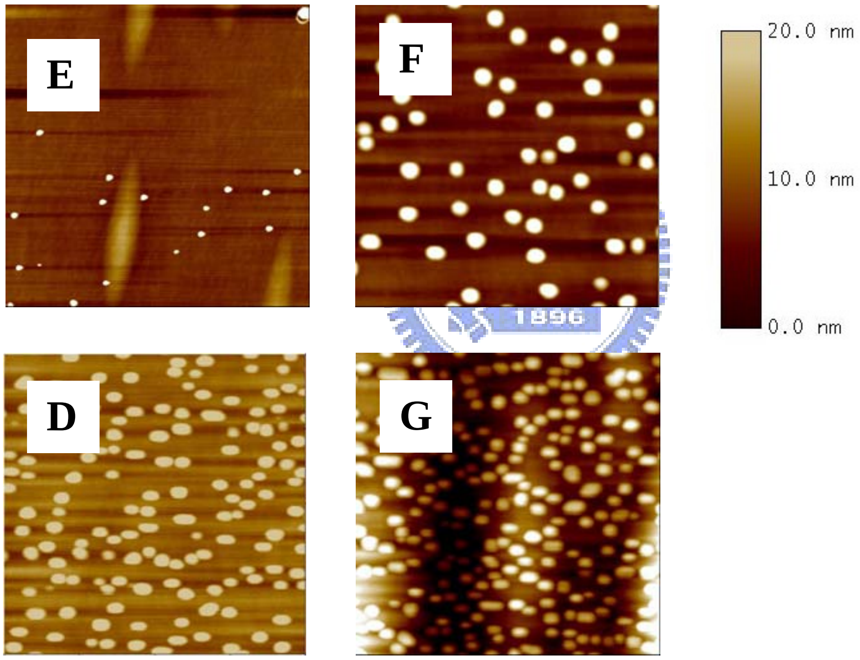

Figure 7.4: The surface AFM image of sample E, F, D, and G. The image size of sample E is 5μm×5μm, and the others are 1μm×1μm. Sample E, F, D and G was grown at 540℃, 520℃, 500℃ and 480℃.

Fig. 7.5 shows the surface AFM image of sample H, D, I, and J. The III/V flux ratio is 3, 5, 10, and 20. We keep the Ga growth rate and vary the Sb flux during the QD growth. The growth temperature was kept at 500℃, and the film thickness is 4 ML. When the III/V flux ratio became higher, the shape of the QDs became more unsymmetrical. The QDs show a slight elongation along [1-10] direction compared to [110] direction.

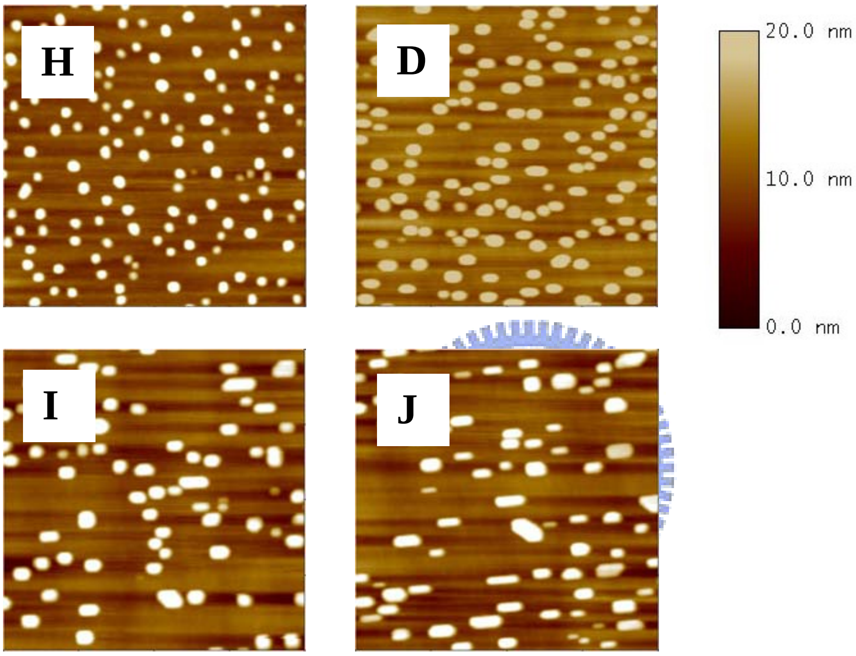

Figure 7.5: The surface AFM image of sample H, D, I, and J with the image size 1µm×1µm. The V/III flux ratio is equal to 3, 5, 10 and 20.

The lower and higher V/III flux ratio will result in Stranski-Krastanov (SK) growth mode and interfacial misfit (IMF) mode, respectively [63]. Fig. 7.6 (a) and (b) show the cross-section TEM image of the surface QDs in SK and IMF growth mode. The interface of GaSb QDs and the GaAs substrate shows the dislocation-free interface. In the IMF mode QDs, the dislocation generates at the interface. The SK growth mode QDs remain highly stressed, and the IMF growth mode produces strain-relaxed QDs. The sample H, the V/III flux ratio is 3, is grown with SK mode and the QDs maintain the circular shape. The sample J, the V/III flux ratio is 20, is grown with IMF mode and the QDs become the rectangular shape along [1-10] direction.

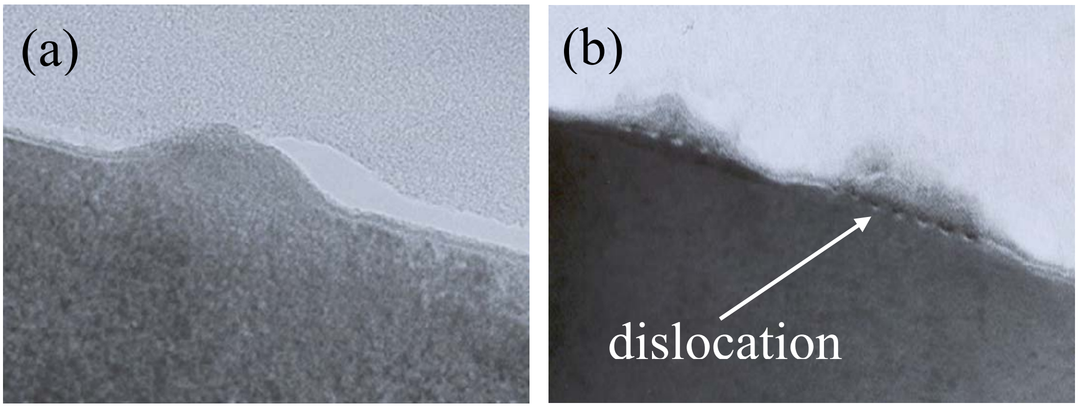

Figure 7.6: (a) SK mode GaSb/GaAs QDs. (b) IMF mode GaSb/GaAs QDs. There misfit array at the GaSb QDs and GaAS substrate interface.

The critical thickness of the QDs formation is between 1~2 monolayer due to the high lattice mismatch (8%). The more deposit material results in the higher QDs density. The higher epitaxial temperature results in lower QD density. The characteristics of the GaSb/GaAs QDs growth are similar to that of the InAs/GaAs QDs. However, the V/III flux ratio will influence the GaSb/GaAs QD growth mode. The higher V/III flux ratio results in IMF growth mode, which generates dislocations at the interface.

7.4 Photoluminescence Study

7.4.1 Photoluminescence study at different excitation power.

The GaSb/GaAs heterostructure is the type-II band alignment, where the hole and electron are spatially separated as shown in fig. 7.7. For the GaSb/GaAs QDs, the hole is confined in the dot, and the electron, which surrounds the dot, is confined in the triangular potential well in GaAs side.

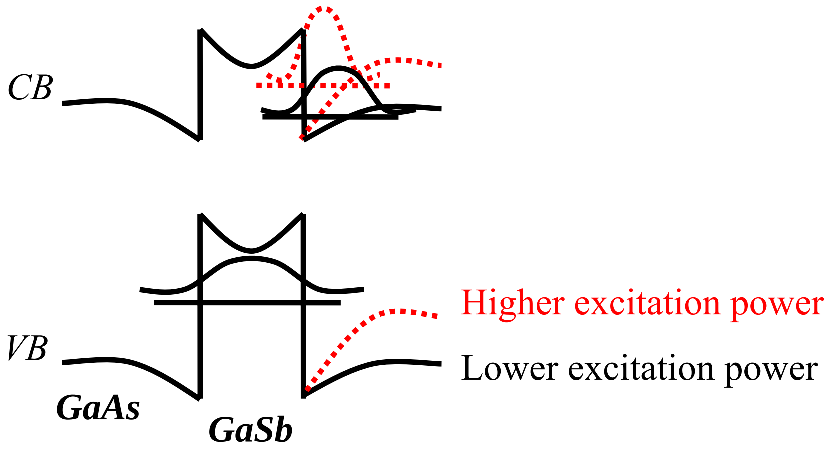

Figure 7.7: The schematic band structure of the GaSb/GaAs heterostructure in different excitation level.

Because of the type-II heterostructure, the carrier recombination lifetime is longer than the type-I heterostructure. The carrier density increases significantly with the excitation power. The electric filed, which is induced by the spatial separated electron-hole space charge, increases as excitation power increases. As the dash curve at fig. 7.7, the increased electric field causes an upward shift of the energy level in the triangular potential well on the GaAs side. Fig. 7.8 shows the low temperature (20K) PL response of sample D at the excitation power varying from 1mW to 30mW.

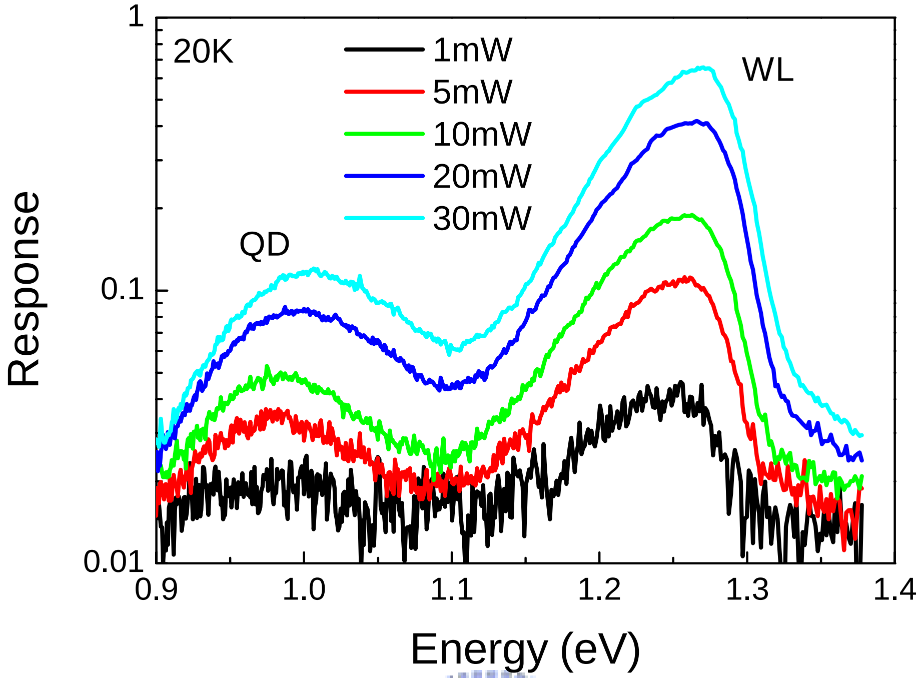

Figure 7.8: The 20K PL response spectrum of the sample D at different excitation power.

The higher energy emission peak comes from the wetting layer (WL) emission, and the lower energy emission peak comes from the QDs. The emission intensity of the WL is higher than that of QDs, because the wavefunction overlap of electron-hole pair of WL is larger than QDs. The peak position shows clearly blue shift as the excitation power increases. The observed blue shift for the emission peaks from GaSb/GaAs heterostructures is usually proportional to the 1/3 power of the excitation level, which is consistent with the triangular well approximation for electrons in GaAs [5]. Fig. 7.9 shows the emission energy positions of sample A as a function of the cubic root of the excitation power. Sample A has the simplest GaSb structure, and thus it is suit for the proof of the triangular well approximation. As seen in the figure, the energy shift follows the 1/3 power dependence quite well. But it should be noted that the excitation power was kept below 10mW in this plot. At higher pumping powers, because of local heating, the 1/3 power law dependence will no longer be valid.

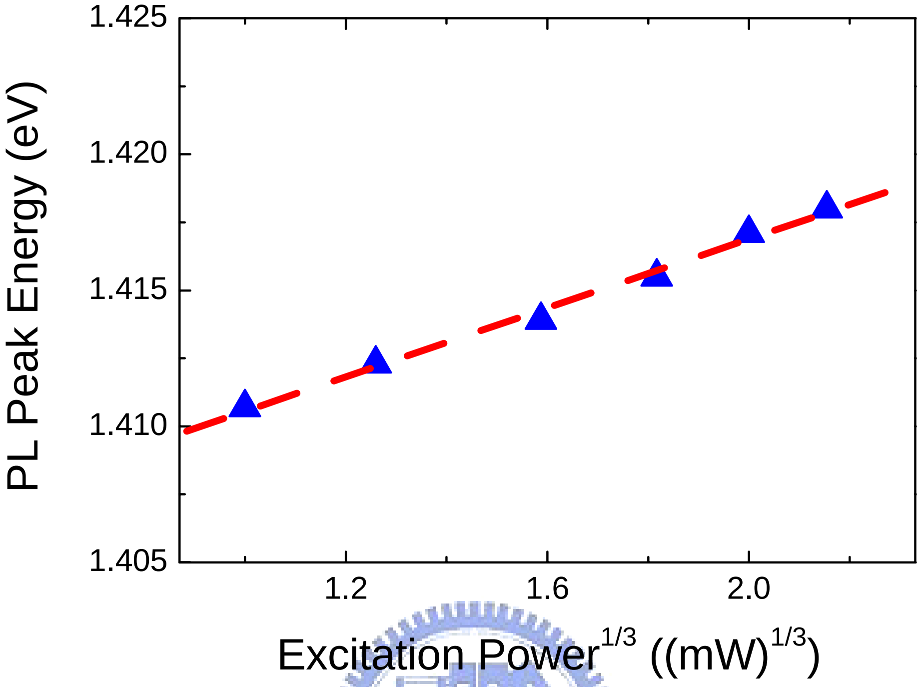

Figure 7.9: Measured transition energy of sample A as a function of the cubic root of the excitation power.

7.4.2 Photoluminescence study at different temperature

Fig. 7.10 shows the emission spectrum of sample D in different temperature at 10mW excitation power. Fig. 7.11 shows the emission peak energy level of the WL and QDs as functions of temperature. The peak position of WL shows a red shift with temperature. However, the peak position of QDs shows a slightly blue shift during 10K to 160K. This result is observed only in type-II QDs heterostructure due to the longer carrier lifetime and easier carrier migration [64]. The electron can easily migrate from one dot to another dot through the nonlocalized state of the WL, because of the poor confinement of the triangular potential well. In this case, the PL spectrum of the QDs emission is a product of the density of state (DOS) and the quasiequilibrium thermal distribution function of the trapped electrons. Fig. 7.12

illustrates the situation. The G(E) is the Gaussian DOS distribution, and the F(E, T) is the Fermi-Dirac distribution function. At lower temperature (T_0), only QDs with energies lower than the electron quasi-Fermi level are populated. Higher temperature (T_1) causes a redistribution of the localized electrons. As a result, the emission peaks of QDs shows blue shift with temperature.

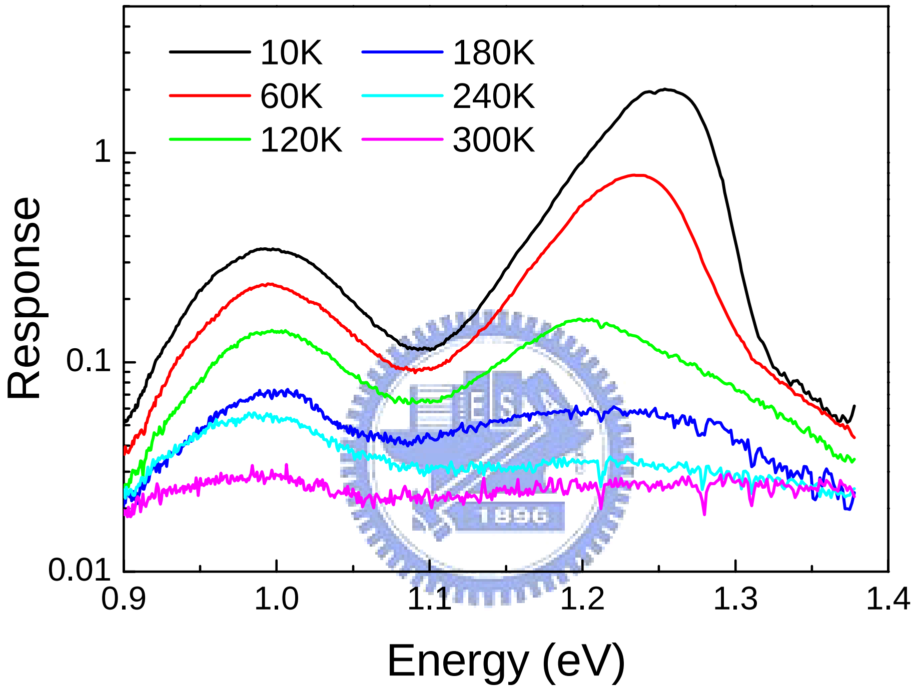

Figure 7.10: PL emission spectrum of sample D at different temperature at 10mW excitation power.

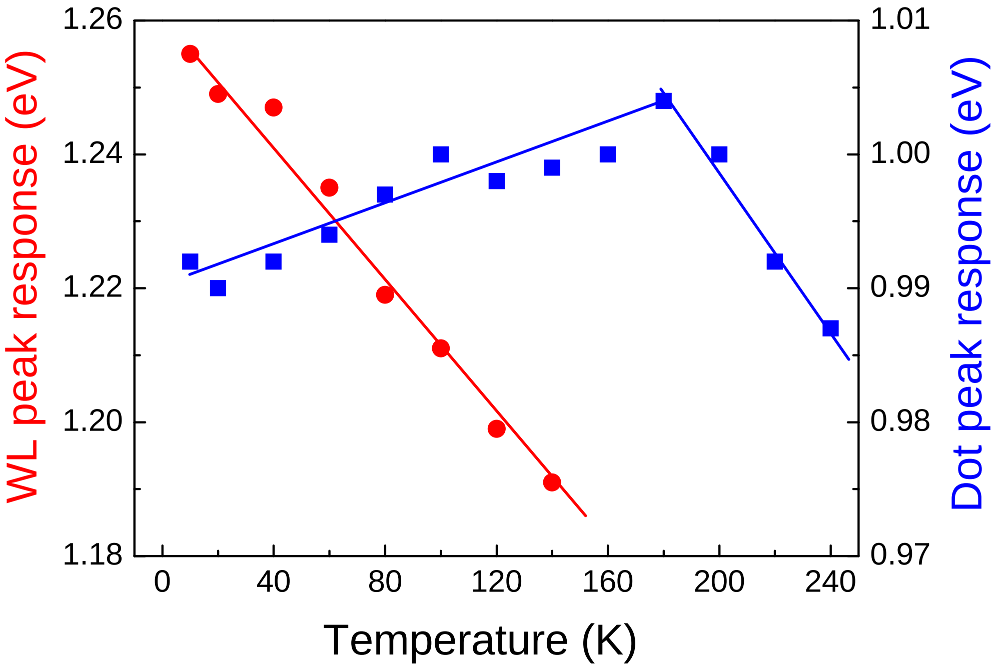

Figure 7.11: The emission peaks energy level of WL and QDs at different temperature.

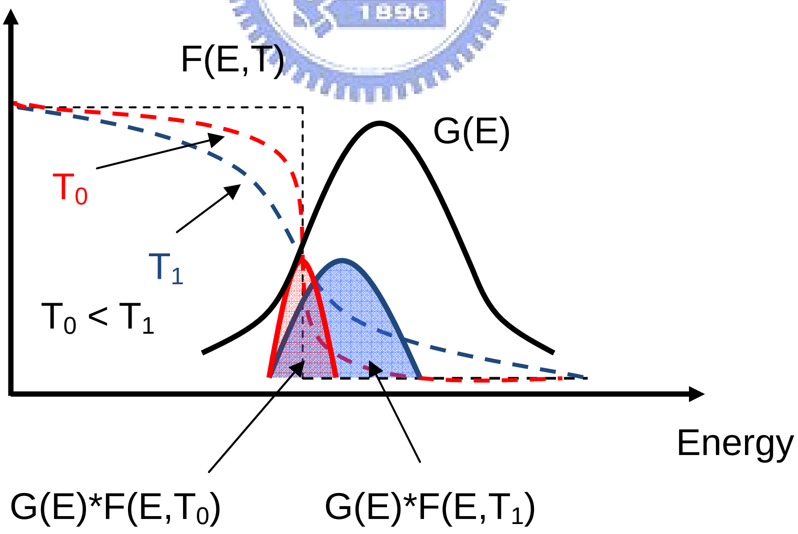

Figure 7.12: Product of Fermi-Dirac and Gaussian distribution at different temperatures.

The emission peak position of QDs is determined by two phenomena. One is the blue shift due to the electron quasi-equilibrium, and the other is the red shift due to the temperature rising. Not in all of the type-II QDs samples, the blue shift phenomenon can be observed. The blue shift with temperature can be observed in denser QDs samples, because the denser QDs allow the electrons redistribution and reach quasi-equilibrium easier.

7.5 Discrete Monolayer Light Emission from GaSb Wetting Layer

The PL measurement of the sample A and B was performed at 20 K with a CW Ar^+ laser as the excitation source. The excitation power was varied from 1 mW to 100 mW. The measured spectra of samples A and B are shown in Fig. 7.13 (a) and (b), respectively. For sample A (see Fig. 7.13 (a)), the dominant peak is A_1 at ~1.4 eV. At low excitation levels, this is the only peak observed. But when the excitation exceeds 100 mW, two additional peaks A_2 and A_3 at about 1.3 and 1.22 eV are observed along with the main peak A_1. For sample B, the situation is more complicated. From Fig. 7.13 (b), one can see that the emission is dominated by the peak B_2 at ~1.3 eV at all excitation levels. With the excitation level increasing, the side peaks B_1 and B_3, at 1.22eV and 1.4eV respectively, become more obvious. It is noticed that the three peaks B_i for sample B appear exactly at the same positions of the peaks A_i for sample A (i=1, 2, 3). At the excitation of 100 mW, we also found a broad peak B_{QD} around 1.05 eV in the spectrum for sample B. This peak is absent from the spectra for sample A and should be attributed to optical transition in QDs.

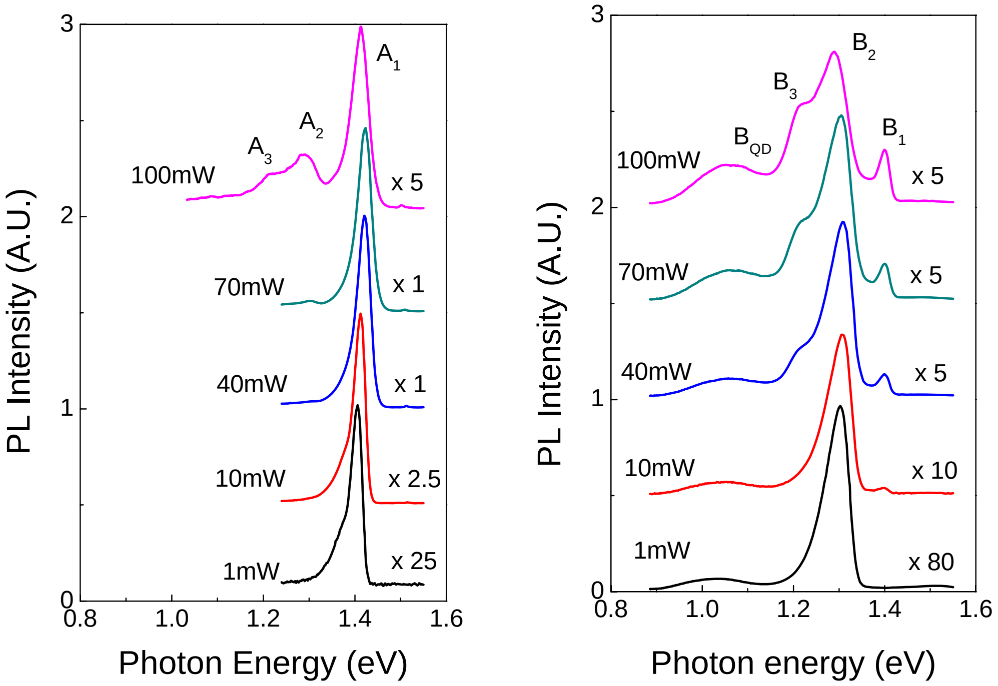

Figure 7.13: Photoluminescence spectra of (a) sample A and (b) sample B at 20K.

The fact that the positions of the emission peaks from two different samples are identical indicates that they originate from optical transitions in QWs with the same thickness. The QW in sample A has a nominal thickness of 1 ML allows us to assign the main peak A_1 to the optical transition in 1-ML QWs. Consequently, the lower peaks A_2 and A_3 at lower energies can be assigned to optical transitions in 2- and 3-ML QWs, respectively. As will be seen later, this assignment is in reasonable agreement with our calculation result. Based on a similar argument, the main peak B_2 of sample B, which was deposited with 2 MLs of GaSb, is due to the optical transition in 2-ML QWs. The two side peaks B_1 and B_3, therefore, naturally come from optical transitions in 1- and 3-ML QWs, respectively.

Fig. 7.14 shows the energy positions of the emission peaks A_1 and B_2 as functions of the cubic root of the excitation power density. The upper and lower lines in the figure, corresponding to A_1 and B_2 respectively, show how the transition energies in the 1-ML and 2-ML QWs change with excitation power. The plot in Fig. 7.14 is used to obtain the transition energies of 1-ML and 2-ML GaSb/GaAs QWs in the absence of the excitation by linear extrapolation of the lines to the *y*-axis.

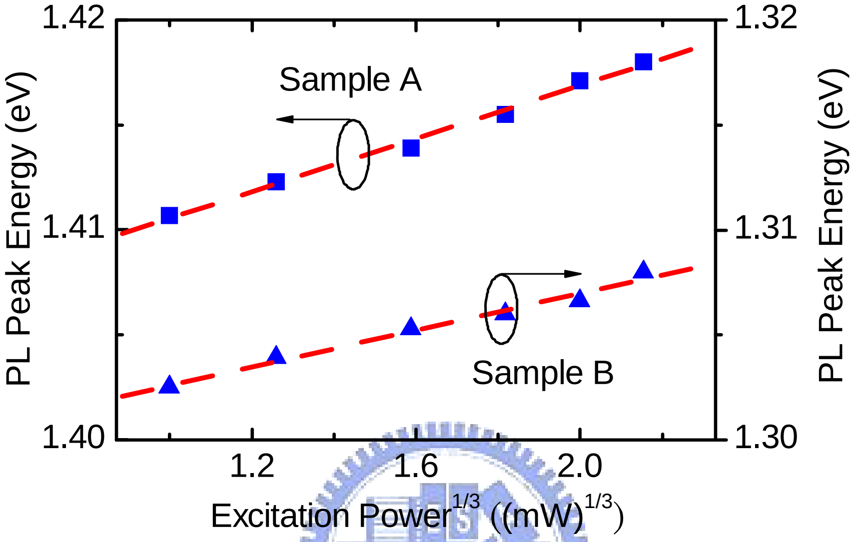

Figure 7.14: Measured transition energy v.s. the cubic root of the excitation power. The interceptions of the extrapolated lines with the y axis give the transition energies at thermal equilibrium.

The obtained transition energy can be considered as the bandgap energy of GaSb/GaAs QWs at thermal equilibrium. The resulting band gap energy is 1.404 eV for 1-ML QW and 1.298 eV for 2-ML QW. For the 3-ML QW, we cannot adopt the extrapolation method described above since we lack a series of appreciable emission signals at low excitation levels. Instead, we estimate the band gap energy at thermal equilibrium for the 3-ML QW to be about the position in energy of the peak B_3 obtained from sample B at excitation of 70 mW. This may overestimate the band gap energy according to the triangular potential well upward shift, but because the heating effect can compensate part of the energy shift, we expect the error is reasonably small compared to the difference from the band gap energy of 1-ML or 2-ML QW.

Now that the band gap energies of 1-, 2-, and 3-ML QWs have been obtained by experiment, we can determine the band offset between GaSb and GaAs by fitting the theoretically calculated band gap to the experimentally obtained data with the band offset as an adjusting parameter. To this end, we use the eight-band **k•p** model to calculate the valence band structures of GaSb/GaAs QW in the flat-band approximation for various values of band offset [65]. The strain effect is considered, assuming the GaSb is pseudomorphically grown on strain-free GaAs, using the Bir-Picus deformation potential theory. The parameters taken for calculation can be found in Ref. 32. The calculated transition energy is then the difference between the GaAs conduction band edge and the first heavy-hole subband edge in the GaSb QW. Fig. 7.15 shows the calculated transition energy of 1-, 2-, and 3- ML GaSb QWs for a series of valence band offset (VBO) values, along with the data obtained from measurement, where VBO is the difference in valence band edge between strain-free GaSb and strain-free GaAs. As can be seen, the variation of the transition energy with the QW thickness is quite consistent between the calculation and the measurement, proving the correctness of our previous assignment of the emission peaks to optical transition in QWs with definite monolayer-scale thickness. Comparison between the calculated and the measured data suggests that the strain-free VBO should lie in the range of 0.4~0.6 eV. With the strain in GaSb included, the VBO should lie in the range of 0.61~0.81 eV. For the best fitting, the VBO is 0.45 eV. The slight deviation in the calculated data is attributed to the omission of band bending in our calculation, which is particularly important to the structure with the 3-ML QW. There is a wide range of VBO values (from 0.12 to 0.9 eV) reported in the past [32, 66-69]. Our study has narrowed significantly the VBO range.

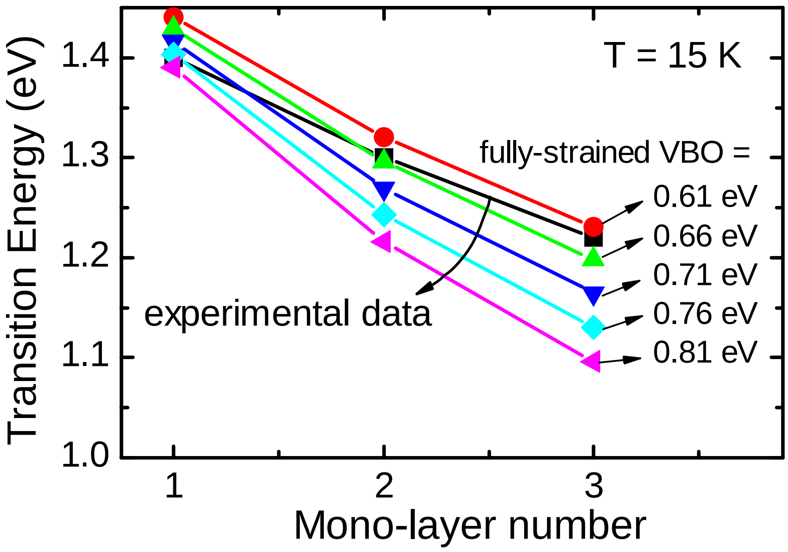

Figure 7.15: Transition energies of quantum wells with 1, 2 and 3 ML of GaSb. The measured result is compared with the theoretical result.

7.6 Summary

The growth conditions of the GaSb quantum dots in GaAs (001) matrix are systematically investigated, including the film thickness, substrate temperature and V/III flux ratio. And, the photoluminescence results in different excitation power and temperature have also been studied. Due to the type-II band alignment, the carrier lifetime of GaSb/GaAs QDs is much longer than InAs/GaAs QDs. The peak energy blue shift with excitation power density and temperature is caused by the much longer carrier lifetime. Besides, we have observed distinct PL peaks from monolayer GaSb layers in GaAs. Such peaks have been identified to be originated from optical transitions in 1-, 2- and 3-ML GaSb/GaAs type-II QWs. The observed phenomenon is peculiar to the monolayer-scale GaSb/GaAs layers. A range of valence band offset for the GaSb/GaAs heterojunction from 0.4 to 0.6 eV is suggested according to the fitting of the measured data to our eight-band **k•p** calculation.

Chapter 8

GaSb Growth on Silicon (001) Substrate

8.1 Introduction

III-antimonide compounds have been regarded as potential materials for application in ultra high speed devices and long wavelength photonic devices due to their high electron mobility and small band gap energies. The compound semiconductor AlSb (6.13Å), GaSb (6.10Å), and InAs (6.06Å) with the similar lattice constant are candidates for these applications [4, 59, 60]. Due to the expensive price and crisp characteristic of GaSb substrate, the GaSb material has usually been grown on GaAs substrate with thick AlSb buffer layer [4]. Moreover, the Silicon wafer has several advantages, including low cost, hardness, large size and mature integration circuit technology. Therefore, the growth of III-V compound on Silicon wafer is of great potential in the optical and logic circuit integration application. However, only few reports on the growth of GaSb on Silicon substrate are published [36, 37, 70-73]. In this work, we report the study of GaSb growth on Silicon (001) substrate with different buffer layer.

8.2 Samples growth condition

All the samples in this study were grown by VEECO Gen-II solid source MBE system with antimony valve cracker source. In our MBE system, it is difficult to generate a clean and well ordered Silicon substrate surface. Therefore, we use an ex-situ chemical etching clean process to remove the surface native oxide. The silicon substrate was cleaned by diluted HF solution for 10 minutes followed by de-ionized water. After the chemical cleaning procedure, the substrate was loaded into vacuum environment to avoid the silicon dioxide formed. After substrate cleaning, the silicon surface was passivated with hydrogen atoms. Before sample growth, the hydrogen atoms were removed by heating the Silicon substrate more than 600℃. After 10 minutes desorption, the silicon surface showed the 2×2 reflection high energy electron diffraction (RHEED) reconstruction pattern suggested the hydrogen atom free surface. During sample growth, the antimony beam equivalent pressure (BEP) was kept at 1×10^{-6} torr, and the cracking zone temperature of antimony cell was kept at 1050℃.

In this work, three samples were prepared with different buffer layer structure. After the buffer layer growth, 1μm GaSb bulk layer was grown with 1μm/hr growth rate. The V/III flux ratio was about 3 and the growth temperature was at 500℃. An 8nm $In_{0.2}Ga_{0.8}Sb$ QW was inserted in GaSb bulk layer at 150nm below sample surface for the optical property study. The QW growth temperature was at 490℃. Fig. 8.1 shows the sample structure.

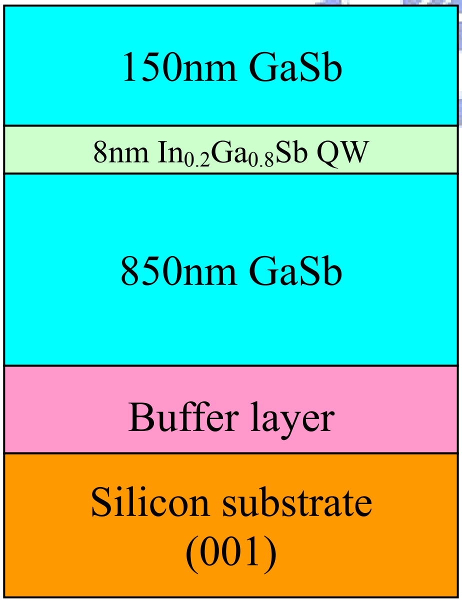

Figure 8.1: The sample structure of GaSb on Silicon substrate in our study.

The buffer layer structure in sample A, B and C is:

A. Without any AlSb buffer layer, the GaSb was grown directly on the silicon surface.

B. With 100nm AlSb buffer layer at 480℃, and the growth rate was 0.5μm/hr.

C. With GaSb(10nm)/AlSb(10nm) 10 periods superlattice buffer layer at 480℃, the GaSb and AlSb growth rate was 1μm/hr and 0.5μm/hr.

8.3 Experiment result

After the growth, the sample A shows a non-mirror surface, but the sample B and C shows a better mirror surface. Therefore, the surface morphology of sample B and C is much smoother than that of sample A. Fig. 8.2 shows the surface AFM image of these three samples. All of the AFM image size is 10μm×10μm with 30nm scale bar. The surface roughness of sample A is the worst, and the other two samples are much similar. The surface roughness is quantified by the atomic force microscope (AFM). The root mean square surface roughness of sample B and C are 4.27nm and 3.88nm with the same scanning parameter. The sample C showes the best surface flatness quality. The flatter surface is better for the structure growth.

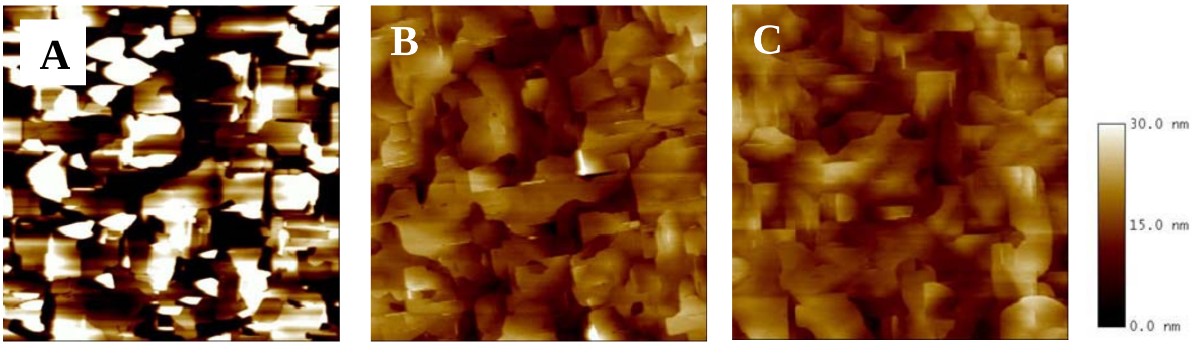

Figure 8.2: The surface AFM image of these three samples. The image size is 10μm×10μm with the 30nm scale bar.

Fig. 8.3 shows the $In_{0.2}Ga_{0.8}Sb$/GaSb QW low temperature (20K) photoluminescence (PL) response of these three samples. The sample C shows the largest response intensity and the smallest full width at half maximum (FWHM). The FWHM of sample C is 11.2meV. The peak emission energy of the $In_{0.2}Ga_{0.8}Sb$ QW varies from 0.71eV to 0.73eV. The peak energy variation might be due to the source beam flux variation. With simple estimation, 2% material composition difference on $In_{0.2}Ga_{0.8}Sb$ QW results in 11meV energy level change.

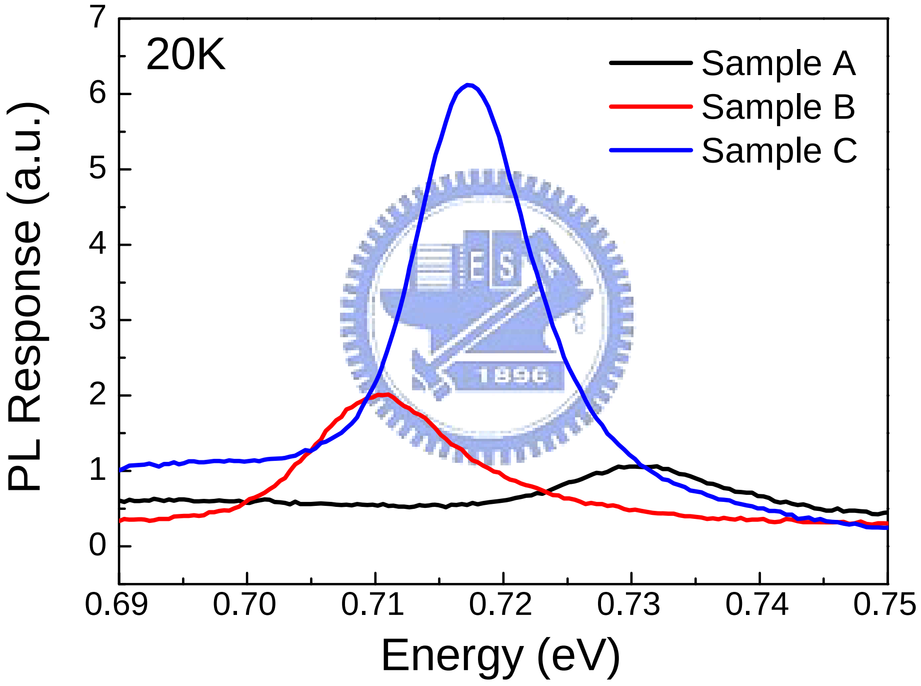

Figure 8.3: The 20K PL response from the 8nm $In_{0.2}Ga_{0.8}Sb$/GaSb QW. The FWHM of sample C is 11.2meV.

Fig. 8.4 shows the high resolution X-ray diffraction (XRD) rocking curve from GaSb (004) orientation of the three samples. The scatter point is the measurement data and continuous curve is the gaussian fitting curve. These three samples were measured at the same condition and the same X-ray source intensity. The sample C shows the higher intensity and smaller FWHM. The FWHM of sample C is 490 arcsec,

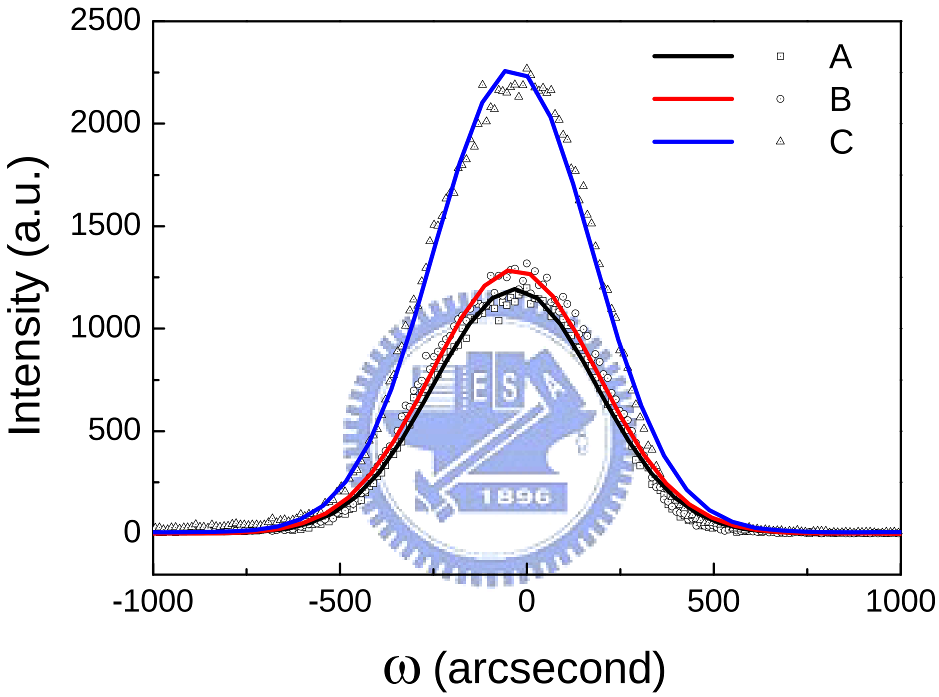

Figure 8.4: High resolution XRD (004) rocking curve of GaSb on Silicon. The FWHM of the sample C is 490 arcsec.

In our study, three analysis techniques (AFM, PL and XRD) show the GaSb bulk and $In_{0.2}Ga_{0.8}Sb$/GaSb QW quality of sample C is the best and sample A is worst. The AlSb buffer layer is necessary in the crystal growth of GaSb on Silicon substrate. Moreover, the GaSb/AlSb superlattice buffer layer is the best choice for the growth.

8.4 Discussion

The lattice constant of GaSb and silicon is 6.10 Å and 5.43 Å, and the lattice mismatch is about 12%. When GaSb deposited directly on silicon substrate, it would generate many dislocations at the interface. The non-mirror surface of sample A suggests that the GaSb does not block dislocations propagation efficiently. When 100nm AlSb buffer layer was inserted at GaSb and silicon interface in sample B, the GaSb crystal shows a mirror surface. The surface AFM image of sample B is smoother than that of sample A and the PL and XRD study also shows the better result. The $In_{0.2}Ga_{0.8}Sb$/GaSb QW PL intensity of sample B is two times larger than that of sample A. Therefore, the AlSb buffer layer plays an important role in the GaSb and silicon heterojunction growth. The lattice constant of AlSb is 6.13 Å, and the lattice mismatch to silicon is about 13%. When AlSb deposited on silicon, many dislocations generate. Observing the RHEED pattern variation during sample growth, the reconstruction pattern is spotty during the first few monolayers. The few monolayers AlSb form the QDs, which is the nucleation process, on the Silicon surface [37, 71-73]. When more AlSb deposited on the substrate, the reconstruction pattern changes from spotty to streaks. The streaky reconstruction pattern indicates that the AlSb QDs coalesce to a bulk material. This nucleation and coalescence process generates an undulation surface, which accommodates the AlSb and silicon heterointerface strain energy. These processes are the strain relief mechanism.

In sample C, the QW PL intensity shows three times larger than sample B, and the FWHM is also better than sample B. Also, the intensity and FWHM of the XRD measurement data shows the best result in the three samples. Thus, the ten periods superlattice GaSb (10nm)/AlSb (10nm) buffer layer is the best buffer layer structure to prevent the dislocation propagation in our study. The lattice constant mismatch between AlSb and GaSb is only 0.5% and thus the heterointerface is nearly strain free.

The superlattice structure is able to merge dislocations and stop dislocation propagation. The first 10nm AlSb layer also plays as the nucleation and coalescence process. The 10nm AlSb layer is about 30 monolayers that are thick enough to coalesce the AlSb QDs and form the undulation surface. During the 10nm AlSb growth, the reconstruction pattern changes from spotty to streaky pattern. Fig. 8.5 shows the GaSb/AlSb superlattice high resolution transmission electron microscope (HR-TEM) image of sample C. In the area 1 and 2, the dislocations merge at the GaSb/AlSb interface. And, in the area 3, the dislocation stops at the interface.

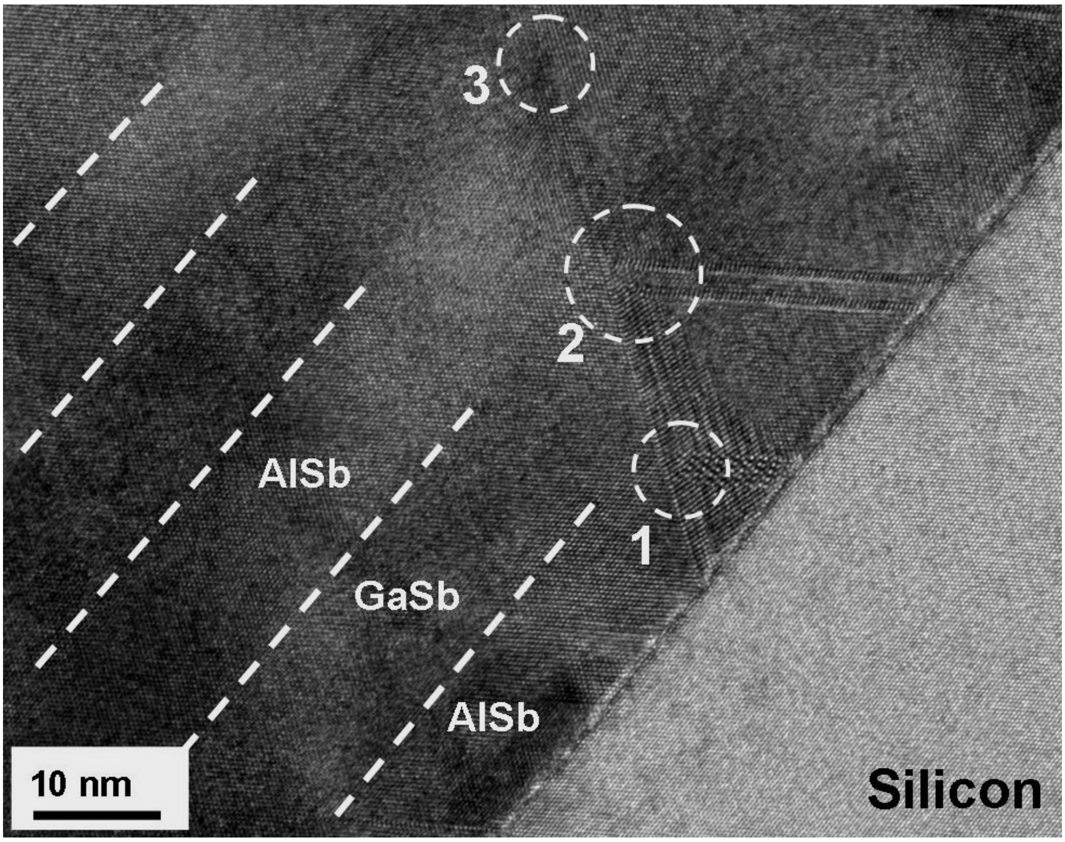

Figure 8.5: Cross-section HR-TEM image of the GaSb/AlSb superlattice on silicon substrate in sample C. In area 1, 2 and 3 the dislocations merge or stop at the superlattice interface.

8.4 Summary

The heterojunction growth of GaSb on silicon (001) substrate with different buffer layer has been studied. When the GaSb deposited directly on the silicon surface, the GaSb crystal surface shows a non-mirror surface. It is necessary to use the AlSb as the buffer layer material to enhance the crystal quality. This AlSb nucleation and coalescence processes accommodate the heterojunction strain energy and result in better crystal quality. Furthermore, the GaSb/AlSb superlattice interface would merge the dislocations and block the dislocation propagation. This buffer layer structure results in better GaSb crystal quality.

Chapter 9

Conclusion

In this dissertation, the study of the quantum dot infrared photodetectors (QDIPs) and GaSb material are presented at the former chapters. The primary conclusion is summarized as follows:

The first part: quantum dot infrared photodetectors (QDIPs):

The responsivity temperature dependence behavior of InAs/GaAs QDIPs has been investigated. From the measurement, we found the dramatic change of the current gain with temperature dominates the behavior of the responsivity. The increasing dark current with the temperature injects more carriers into the QDs. The repulsive potential of the extra carriers suppresses the capture process and enhances the current gain. The average extra carrier numbers calculated from the capture probability qualitatively explained the behavior of the quantum efficiency. From this concept, QDIPs with smaller QD and higher density is predicted to have better temperature stability and also maintain a higher current gain.

The vertically coupled QDIPs have been investigated. With the mini-bands in the coupled QDs, the photoresponse spectrum, quantum efficiency, and the roll-off frequency for QDIPs have been improved. The photoresponse spectrum shows a smaller fractional spectral width of 6% ($\Delta\lambda/\lambda_p$), which increased the quantum efficiency. The mini-bands also enhanced the capture probability and the roll-off frequency dramatically. The device provided a possible solution to enhance the quantum efficiency and roll-off frequency at the same time. More works to improve the vertical alignment of the QDs will further improve the performance of the vertically coupled QDIPs.

The QDIPs with a thin wide band gap material $Al_{0.2}Ga_{0.8}As$ layer near QDs have been studied. The board photocurrent spectra of the simple InAs/GaAs QDIPs are found to be composed of two transitions. With the insertion of the $Al_{0.2}Ga_{0.8}As$ layer, the response spectra could be separated into two peaks. One of the peaks is fixed at 6μm, and the other shifts to higher energy and the intensity becomes weaker as the decrease of the $Al_{0.2}Ga_{0.8}As$ layer distance. The much narrow photocurrent spectrum width is obtained, and the fractional spectrum width is reduced from 25% to 10% as the $Al_{0.2}Ga_{0.8}As$ layer is 5nm from the QD layer. Because one of the transitions is suppressed and the carrier contributes to the other transition, the quantum efficiency increases. Also, the thin $Al_{0.2}Ga_{0.8}As$ layer reduces the device dark current, and then the detectivity is enhanced for 5 times.

The second parts: GaSb/GaAs QDs and GaSb growth on silicon substrate:

The growth conditions of the GaSb quantum structure in GaAs (001) matrix have been systematically investigated, including the film thickness, substrate temperature and V/III flux ratio. And, the photoluminescence results in different excitation power and temperature have also been studied. Due to the spatially separated electron and hole, the carrier life time of the type-II GaSb/GaAs QDs is much longer than the type-I InAs/GaAs QDs. This phenomenon would cause the PL signal blue shift with excitation power density and the QD PL signal blue shift with temperature. Furthermore, we observed distinct PL peaks from monolayer GaSb layers in GaAs. Such peaks have been identified to be originated from optical transitions in 1-, 2- and 3-ML GaSb/GaAs type-II QWs. A range of valence band offset for the GaSb/GaAs heterojunction from 0.4 to 0.6 eV is suggested according to the fitting of the measured data to our eight-band **k•p** calculation.

The heterojunction growth of GaSb on silicon (001) substrate with different buffer layer has been studied. When the GaSb deposited directly on the silicon surface, the GaSb crystal surface shows a non-mirror surface. It is necessary to use the AlSb as the buffer layer material to enhance the crystal quality. This AlSb nucleation and coalescence processes accommodate the heterojunction strain energy and result in better crystal quality. Furthermore, the GaSb/AlSb superlattice interface would merge the dislocations and block the dislocation propagation. This buffer layer structure results in better GaSb crystal quality.

Reference:

[1] S. L. Chuang, "Physics of photonic devices", Wiley, New York, (2009)

[2] L. D. Nguyen, L. E. Larson, and U. K. Mishra, Proc. IEEE, **80,** 494 (1992)

[3] D. J. Mowbray, and M. S. Skolnick, J. Phys. D: Appl. Phys. **38,** 2059 (2005)

[4] B. R. Bennett, R. Magno, J. B. Boos, W. Kruppa, and M. G. Ancona, Solid State Ecectron. **49,** 1875 (2005)

[5] N. N. Ledentsov, J. Bohrer, M. Beer, F. Heinrichsdorff, M. Grundmann, D. Bimberg, S. V. Ivanov, B. Ya. Meltser, S. V. Shaposhnikov, I. N. Yassievich, N. N. Faleev, P. S. Kop'ev, and Zh. I. Alferov, Phys. Rev. B **52,** 14058 (1995)

[6] F. Hatami, N. N. Ledentsov, M. Grundmann, J. Bohrer, F. Heinrichsdorff, M. Beer, D. Bimberg, S. S. Ruvimov, P. Werner, U. Gosele, J. Hexdenreich,U. Richter, S. V. Ivanov, B. Ya. Meltser, P. S. Kop'ev, and Zh. I. Alferov, Appl. Phys. Lett. **67,** 656 (1995)

[7] C. K. Sun, G. Wang, J. E. Bowers, B. Brar, H. R. Blank, H. Kroemer, and M. H. Pilkuhn, Appl. Phys. Lett. **68,** 1543 (1996)

[8] A. Rogalski, Infrared Phys. & Technol. **38,** 295 (1997)

[9] L. C. West, and S. J. Eglash, Appl. Phys. Lett. **46,** 1156 (1985)

[10] B. F. Levine, K. K. Choi, C. G. Bethea, J. Walker, and R. J. Malik, Appl. Phys. Lett. **50,** 1092 (1987)

[11] L. J. Kozlowski, G. M. Williams, G. J. Sullivan, C. W. Farley, R. J. Anderson, J. Chen, D. T. Cheung, W. E. Tennant, and R. E. DeWames, IEEE Trans. on Electron. Devices **38,** 1124 (1991)

[12] S. V. Bandara, S. D. Gunapala, J. K. Liu, S. B. Rafol, D. Z. Ting, J. M. Mumolo, R. W. Chuang, T. Q. Trinh, J. H. Liu, K. K. Choi, M. Jhabvala, J. M. Fastenau,

and W. K. Liu, Infrared Phys. & Technol. **44,** 369 (2003)

[13] V. Ryzhii, Semicond. Sci. Technol. **11,** 759 (1996)

[14] H. Drexler, D. Leonard, W. Hansen, J. P. Kotthaus, and P. M. Petroff, Phys. Rev. Lett. **73,** 2252 (1994)

[15] J. Phillips, K. Kamath, X. Zhou, N. Chervela, and P. Bhattacharya, Appl. Phys. Lett. **71,** 2079 (1997)

[16] K. W. Berryman, S. A. Lyon, and M. Segev, Appl. Phys. Lett. **70,** 1861 (1997)

[17] S. J. Chua, S. J. Xu, X. H. Zhang, X. C. Wang, T. Mei, W. J. Fan, C. H. Wand, J. Jiang, and X. G. Xie, Appl. Phys. Lett. **73,** 1997 (1998)

[18] J. Phillips, K. Kamath, and P. Bhattacharya, Appl. Phys. Lett. **72,** 2020 (1998)

[19] S. Maimon, E. Finkman, G. Bahir, S. E. Schacham, J. M. Garcia, and P. M. Petroff, Appl. Phys. Lett. **73,** 2003 (1998)

[20] D. Pan, E. Towe, and S. Kennerly, Appl. Phys. Lett. **73,** 1937 (1998)

[21] S. J. Xu, S. J. Chua, T. Mei, X. C. Wang, X. H. Zhang, G. Karunasiri, W. J. Fan, C. H. Wang, J. Jiang,S. Wang, and X. G. Xie, Appl. Phys. Lett. **73,** 3153 (1998)

[22] S. K. Lee, K. Hirakawa, Y. Shimada, Physica E **7,** 499 (2000)

[23] S. Y. Wang, S. D. Lin, H. W. Wu, and C. P. Lee, Appl. Phys. Lett. **78,** 1023 (2001)

[24] Z. Chen, O. Baklenov, E. T. Kim, I. Mukhametzhanov, J. Tie, A. Madhukar, Z. Ye, and J. C. Campbell, J. Appl. Phys. **89,** 4558 (2001)

[25] A. D. Stiff, S. Krishna, P. Bhattacharya, and S. W. Kennerly, IEEE J. Quantum Electron. **37,** 1412 (2001)

[26] L. Jiang, S. S. Li, N. T. Yeh, J. I. Chyi, C. E. Ross, and K. S. Jones, Appl. Phys. Lett. **82**, 1986 (2003)

[27] S. Chakrabarti, A. D. Stiff-Roberts, P. Bhattacharya, S. Gunapala, S. Bandara, S. B. Rafol, and S. W. kennerly, IEEE Photon. Technol. Lett. **16**, 1361 (2004)

[28] H. S. Ling, S. Y. Wang, C. P. Lee, and M. C. Lo, IEEE Photon. Technol. Lett. **21**, 118 (2009)

[29] P. Bhattacharya, X.H. Su, S. Chakrabarti, G. Ariyawansa, A.G.U. Perera, Appl. Phys. Lett. **86**, 191106 (2005)

[30] H. Lim, S. Tsao, W. Zhang, and M. Razeghi, Appl. Phys. Lett. **90**, 131112 (2007)

[31] S. D. Gunapala,, S. V. Bandara, C. J. Hill, D. Z. Ting, J. K. Liu, S. B. Rafol, E. R. Blazejewski, J. M. Mumolo, S. A. Keo, S. Krishna, Y. C. Chang, and C. A. Shott, Infrared Physics & Technology **50,** 149 (2007)

[32] I. Vurgaftman, J. R. Meyer, and L. R. Ram-Mohan, J. Appl. Phys. **89,** 5815 (2001)

[33] C. E. Pryor, and M. E. Pistol, Phys. Rev. B **72,** 205311 (2005)

[34] P. S. Dutta, H. L. Bhat, and V. Kumar, J. Appl. Phys. **81,** 5821 (1997)

[35] A. Joullie, and P. Chrostol, C. R. Physique **4,** 621 (2003)

[36] K. Akahane, N. Yamamoto, S. Gozu, and N Ohtani, J. Crystal Growth **264,** 21 (2004)

[37] G. Balakrishnan. S. Huand, L. R. Dawson, Y. C. Xin, P. Conlin, and D. L. Huffaker, Appl. Phys. Lett. **86,** 034105 (2005)

[38] Z. Ye, J. C. Campbell, Z. Chen, E. T. Kim, and A. Madhukar, **83**, 1234 (2003)

[39] H. Lim, W. Zhang, S. Tsao, T. Sills, J. Szafraniec, K. Mi. B. Moraghar, and M. Razeghi, Phys. Rev. B **72,** 085332-1 (2005)

[40] J. Y. Duboz, H.C. Liu, Z.R. Wasilewski, M. Byloss, and R. Dudek, J. Appl. Phys. **93,** 1320 (2003)

[41] V. Ryzhii, I. Khmyrova, M. Ryzhii, and V. Mitin, Semicond. Sci. Technol. **19,** 8 (2004)

[42] K.W. Sun, A. Kechiantz, B.C. Lee, and C.P. Lee, Appl. Phys. Lett. **88,** 163117 (2006)

[43] J. Urayama, T.B. Norris, J. Singh, and P. Battacharya, Phys. Rev. Lett. **86,** 4930 (2001)

[44] O. Stier, M. Grundmann, and D. Bimberg, Phys. Rev. B **59,** 568 (1999)

[45] D. T. Le, C. P. Morath, H. E. Norton, D. A. Cardimona, S. Raghavan, P. Rotella, S. A. Stintz, B. Fuchs, and S. Krishna, Infrared Physics & Technology **44,** 517 (2003)

[46] R. Rehm, H. Schneider, M. Walther, and P. Koidl, Appl. Phys. Lett. **80,** 862 (2002)

[47] Y. Paltiel, N. Snapi, A. Zussman, and G. Jung, Appl. Phys. Lett. **87,** 231103-1 (2005)

[48] G. S. Solomon, J. A. Trezza, A. F. Marshall, and J. S. Harris, Phys. Rev. Lett. **76,** 952 (1996)

[49] G. S. Solomon, J. A. Trezza, A. F. Marshall, and J. S. Harris, J. Vac. Sci. Technol. B **14(3),** 2208 (1996)

[50] Q. D. Zhuang, J. M. Li, H. X. Li, Y. P. Zeng, L. Pan, Y. H. Chen, M. Y. Kong, and L. Y. Lin, Appl. Phys. Lett. **73,** 3706 (1998)

[51] L. Brusaferri, S. Sanguinetti, E. Grilli, M. Guzzi, A. Bignazzi, F. Bognai, L. Carraresi, M. Colocci, A. Bosacchi, P. Frigeri, and S. Franchi, Appl. Phys. Lett. **69,** 3354 (1996)

[52] S. Snguinetti, M. Henini, M. G. Alessi, M. Capizzi, P. Frigeri, and S. Franchi, Phys. Rev. B **60,** 8276 (1999)

[53] Z. Chen, O. Baklenov, E. T, Kim, I. Mukhametzhanov, J. Tie A. Madhukar, Z. Ye, and J. C. Campbell, J. Appl. Phys. **89,** 4558 (2001)

[54] E. T. Kim, Z. Chen, and A. Madhukar, Appl. Phys. Lett. **79**, 3341 (2001)

[55] B. Aslan, H. C. Liu, M. Korkusinski, S. J. Cheng, and P. Hawrylak, Appl. Phys. Lett. **82**, 630 (2003)

[56] G. A. Narvaez, and A. Zunger, Phys. Rev. B **75**, 085306 (2007)

[57] S. Y. Wang, and C. P. Lee, Appl. Phys. Lett. **71**, 113 (1997)

[58] G. Karunasiri, J. S. Park, J. Chen, R. Shih, J. F. Scheihing, and M. A. Dodd, Appl. Phys. Lett. **67,** 2600 (1995)

[59] Y. Oda, H. Yokoyama, K. Kurishima, T. Kobayashi, N, Watanabe, and M. Uchida, Appl. Phys. Lett. **87,** 023503 (2005)

[60] Q. Yang, C. Manz, W. Bronner, Ch. Mann, L. Kirste, K. Kohler, and J. Wanger, Appl. Phys. Lett. **86,** 131107 (2005)

[61] M.Hayne, J. Maes, S. Bersier, M. Henini, L. Muller-Kirsch, Rober Heitz, D. Bimberg, and V. V. Moshchalkov, Phisica B **346,** 421 (2004)

[62] M. Kudo, T. Mishima, S. Iwamoto, T. Nakaoka, and Y. Arakawa, Physica E **21,** 275 (2004)

[63] G. Balakrishnan, J. Tatebayashi, A. Khoshakhlagh, S.H. Huang, A. Jallipalli, L.R. Dawson, and D. L. Huffaker, Appl. Phys. Lett. **89,** 161104-1 (2006)

[64] O. G. Lyublinskays, V. A. Solov'ev, A. N. Semenov, B. Ya. Meltser, Ya. V. Terent'ev, L. A. Prokopva, A. A. Toropov, A. A. Sitnikova, O. V. Rykhova, S. V. Lvanov, K. Thonke, and R. Sauer, J. Appl. Phys. **99,** 093517 (2006)

[65] A. Zakharova, S. T. Yen, and K. A. Chao, Phys. Rev. B **66,** 085312 (2002)

[66] A. D. Katnani, and G. Margaritondo, J. Appl. Phys. **54,** 2522 (1983)

[67] J. Tersoff, Phys. Rev. B **30,** 4874 (1984)

[68] Y. Tsou, A. Ichii, and Elsa M. Garmire, IEEE J. Quantum Electron. **28,** 1261 (1992)

[69] F. L. Schuermeyer, P. Cook, E. Martinez, and J. Tantillo, Appl. Phys. Lett. **55,** 1877 (1989)

[70] R. J. Malik, J.P. van der Ziel, B. F. Levine, C. G. Bethea, and J. Walker, J. Appl. Phys. **59,** 3909 (1986)

[71] K. Akahane, N. Yamomoto, S. Gozu, A. Ueta, and N Ohtane, J. Crystal Growth **283,** 297 (2005)

[72] G. Balakrishnan, S. Huang, L. R. Dawson, Y. -C. Xin, P. Conlin, and D. L. Huffaker, J. Vac. Sci. Technol. B, **23(3)** 1010 (2005)

[73] T. Toda, F. Nishino, A. Kato, T. Kambayashi, Y. Jinbo, N. Uchitomi, Physica B. **376,** 602 (2006)

Vita

Name: Ming-Cheng, Lo（羅明城）

Sex: Male

Date of Birth: October 8, 1980

Place of birth: Taipei, Taiwan, R.O.C.

Education:

National Chiao Tung University Ph. D September, 2003-

Institute of Electronics Engineering

National Chiao Tung University M. S. September, 2002~June, 2003

Institute of Electronics Engineering

National Chiao Tung University B. S. September, 1998~June, 2002

Institute of Electronics Engineering

Title of the Ph. D Dissertation:

Studies of Quantum Dot Infrared Photodetectors and GaSb Material

Publication List

[1] M. C. Lo, S. D. Lin, S. Y. Wang, and C. P. Lee, "Photoluminescence study of high density InAs/GaAs quantum dots", 7th Trends in Nano Technology International Conference, Sep, 2006

[2] S. Y. Wang, M. C. Lo, H. Y. Hsiao, H. S. Ling, and C. P. Lee, "Temperature dependent responsivity of quantum dot infrared photodetectors", Infrared Physics & Technology **50,** 166 (2007)

[3] M. C. Lo, S. J. Huang, C. P. Lee, S. D. Lin, and S. T. Yen, "Discrete monolayer light emission form GaSb wetting layer in GaAs", Appl. Phys. Lett. **90,** 243102 (2007)

[4] M. C. Lo, S. Y. Wang, S. D. Lin, H. S. Ling, and C. P. Lee, "Photocurrent spectrum tuning of quantum dot infrared photodetectors" submitted to J. Appl. Phys.

[5] H. S. Ling, C. P. Lee, and M. C. Lo, "Energy dependent carrier relaxation in self-assembled InAs quantum dots", J. Appl. Phys. **103,** 124311 (2008)

[6] H. S. Ling, S. Y. Wang, C. P. Lee, and M. C. Lo, "High quantum efficiency dots-in-a-well quantum dot infrared photodetectors with AlGaAs confinement enhancing layer", Appl. Phys. Lett. **92,** 193506 (2008)

[7] M. F. Tsai, H. Lin, C. H. Lin, S. D. Lin, S. Y. Wang, M. C. Lo, S. J. Cheng, M. C. Lee, and W. H. Chang, "Diamagnetic Response of Exciton Complexes in Semiconductor Quantum Dots", Phys. Rev. Lett. **101,** 267402 (2008)